

AFIT/GE/ENG/99M-10

COMPUTATION OF SCATTERING FROM
BODIES OF REVOLUTION USING AN
ENTIRE-DOMAIN BASIS IMPLEMENTATION
OF THE MOMENT METHOD

THESIS

Arthur Peyton Ford, IV
Captain, USAF

AFIT/GE/ENG/99M-10

Approved for public release; distribution unlimited

19990413 097

REPORT DOCUMENTATION PAGE			Form Approved OMB No. 0704-0188	
Public reporting burden for this collection of information is estimated to average 1 hour per response, including the time for reviewing instructions, searching existing data sources, gathering and maintaining the data needed, and completing and reviewing the collection of information. Send comments regarding this burden estimate or any other aspect of this collection of information, including suggestions for reducing this burden, to Washington Headquarters Services, Directorate for Information Operations and Reports, 1215 Jefferson Davis Highway, Suite 1204, Arlington, VA 22202-4302, and to the Office of Management and Budget, Paperwork Reduction Project (0704-0188), Washington, DC 20503.				
1. AGENCY USE ONLY (Leave blank)		2. REPORT DATE March 1999		3. REPORT TYPE AND DATES COVERED Master's Thesis
4. TITLE AND SUBTITLE Computation of Scattering from Bodies of Revolution Using an Entire-domain Basis Implementation of the Moment Method			5. FUNDING NUMBERS	
6. AUTHOR(S) ARTHUR P. FORD, IV, Captain, USAF				
7. PERFORMING ORGANIZATION NAME(S) AND ADDRESS(ES) Air Force Institute of Technology (AFIT) 2950 P Street Wright-Patterson AFB, OH 45433-7765			8. PERFORMING ORGANIZATION REPORT NUMBER AFIT/GE/ENG/99M-10	
9. SPONSORING/MONITORING AGENCY NAME(S) AND ADDRESS(ES) AFRL/XPN 2591 K ST WRIGHT-PATTERSON AFB OH 45433-7602 Major William D. Wood, Program Manager, Low Observables Technology (937) 255-0270			10. SPONSORING/MONITORING AGENCY REPORT NUMBER	
11. SUPPLEMENTARY NOTES Advisor: Major Peter J. Collins (937) 255-6565 ext. 4304 email: Peter.Collins@afit.af.mil				
12a. DISTRIBUTION AVAILABILITY STATEMENT Approved for public release; distribution unlimited			12b. DISTRIBUTION CODE	
13. ABSTRACT (Maximum 200 words) Research into improved calibration targets for measurement of radar cross-section has created a need for the ability to accurately compute the scattering from perfectly conducting bodies of revolution. Common computational techniques use Moment Method codes that employ subdomain basis functions to expand the unknown current density. This approach has its shortcomings. Large numbers of basis functions are required, and increasing the number of basis functions to improve accuracy after an initial computation requires re-computation of previous results and lost processing time. This research involves using basis functions that have as their domain the entire length of the surface. Entire-domain basis functions are better able to model the current density on a smooth surface. Fewer modes are required resulting in smaller matrix sizes. In addition, accuracy can be increased incrementally by adding entire-domain modes while retaining previously computed results saving significant computation time. Electric-field integral equations are developed and solved by an entire-domain implementation of the Moment Method for a perfectly conducting sphere. Comparison is made to the exact Mie series. Convergence in fewer modes is demonstrated over an equivalent application of subdomain pulses. Matrix fill time saves as much as hours over subdomain discretization.				
14. SUBJECT TERMS Method of Moments, Bodies of Revolution, Chebyshev Polynomials, Scattering			15. NUMBER OF PAGES 105	
			16. PRICE CODE	
17. SECURITY CLASSIFICATION OF REPORT Unclassified	18. SECURITY CLASSIFICATION OF THIS PAGE Unclassified	19. SECURITY CLASSIFICATION OF ABSTRACT Unclassified	20. LIMITATION OF ABSTRACT UL	

The views expressed in this thesis are those of the author and do not reflect the official policy or position of the Department of Defense or the United States Government.

AFIT/GE/ENG/99M-10

COMPUTATION OF SCATTERING FROM BODIES OF REVOLUTION
USING AN ENTIRE-DOMAIN BASIS IMPLEMENTATION
OF THE MOMENT METHOD

THESIS

Presented to the Faculty of the School of Engineering
of the Air Force Institute of Technology
Air University
In Partial Fulfillment of the
Requirements for the Degree of
Master of Science in Electrical Engineering

Arthur Peyton Ford, IV, B.A., B.S.E.E.
Captain, USAF

March, 1999

Approved for public release; distribution unlimited

COMPUTATION OF SCATTERING FROM BODIES OF REVOLUTION
USING AN ENTIRE-DOMAIN BASIS IMPLEMENTATION
OF THE MOMENT METHOD

Arthur Peyton Ford, IV, B.A., B.S.E.E.

Captain, USAF

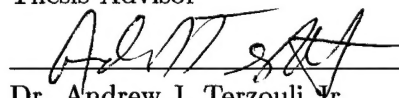
Approved:



Major Peter J. Collins Ph.D.
Thesis Advisor

12 MAR 99

Date



Dr. Andrew J. Terzouli Jr.
Committee Member

12 Mar 99

Date



Dr. William P. Baker
Committee Member

12 Mar 99

Date

Acknowledgements

I would like to express my sincere gratitude to many who have assisted me in this research effort. The effort began at the very beginning of my graduate studies. The guidance I recieved in course selection from my advisor, Maj Pete Collins, was invaluable. I would also like to give thanks to Dr. William Baker and Dr. Andy Terzouli who gave frequent advice and encouragement throughout the research effort. It was the courses the three of them taught that were enlightening to the degree that I had the courage to embark on this path. Additionally, I owe thanks to Maj Bill Wood from the Air Force Research Laboratory for sponsoring this research and for the wisdom he provided.

Most importantly however, I express gratitude to my wife for her patience and my children for their understanding throughout this long effort. Their enduring cheerfulness, made it so much easier.

Arthur Peyton Ford, IV

Table of Contents

	Page
Acknowledgements	iii
List of Figures	vi
List of Tables	viii
Abstract	ix
 I. Introduction	 1-1
 II. Background	 2-1
2.1 Numerical Solution by the Method of Moments	2-1
2.2 Choosing a Basis Function	2-4
2.2.1 Subdomain Basis Functions	2-4
2.2.2 Entire Domain Basis Functions	2-5
2.2.3 Physical Basis Functions	2-8
2.2.4 Hybrid Basis Functions	2-9
2.2.5 Vector Basis Functions	2-9
2.3 Testing Functions	2-11
2.4 Summary and Implications to Bodies of Revolution	2-12
 III. Theory	 3-1
3.1 Definition and Geometry	3-1
3.2 Integral Equations	3-4
3.3 Chebyshev Polynomial Basis Functions	3-6

	Page
IV. Application to the Integral Equation	4-1
4.1 The Impedance Matrix	4-4
4.2 The Voltage Matrix	4-6
4.3 Scattered Field Equation	4-6
4.4 Three-dimensional Scattering Cross-section	4-8
4.5 Summary	4-9
V. Results	5-1
5.1 The Computer Code	5-2
5.2 The Currents	5-7
5.3 The Scattering Cross-Section	5-16
5.3.1 Assessment of Accuracy	5-16
5.3.2 Subdomain Data	5-17
5.3.3 Entire-Domain Data	5-19
5.4 Computation and Matrix Fill Time	5-23
VI. Conclusions and Recommendations	6-1
6.1 Conclusions	6-1
6.2 Recommendations for Future Research	6-2
Appendix A. The Computer Code	A-1
Appendix B. Current Densities by Mode	B-1
Bibliography	BIB-1
Vita	VITA-1

List of Figures

Figure		Page
2.1.	Pulse (piecewise constant) subdomain basis functions.	2-6
2.2.	Triangular (piecewise linear) subdomain basis functions.	2-7
2.3.	A notional example of a directional (vector) basis function on a surface cell.	2-10
3.1.	Geometry of the body of revolution	3-2
3.2.	A plane wave incident on the body of revolution	3-3
3.3.	The first nine modes of the Chebyshev polynomial of the first kind (T_0 - T_8).	3-7
5.1.	Flowchart of MAINSPHERE	5-3
5.2.	Flowchart of MAKEZV	5-4
5.3.	Flowchart of COMPRCS	5-5
5.4.	$\hat{\phi}$ directed current density for the $n = 2$ entire-domain modes for $ka = 4.0$	5-8
5.5.	Total \hat{t} and $\hat{\phi}$ directed current densities ($n = 0-5$) for $ka = 4.0$ illuminated by E_{ϕ}^{inc} at $\theta = 90^\circ$	5-9
5.6.	Total $\hat{\phi}$ directed current density ($n = 0-5$) for $ka = 3.1$ illuminated by E_{ϕ}^{inc} at $\theta = 90^\circ$	5-10
5.7.	$\hat{\phi}$ directed current density coefficients for the T_0 - T_{10} entire-domain modes, grouped by Fourier mode	5-11
5.8.	\hat{t} directed current density for the $n = 2$ entire-domain modes for $ka = 4.0$	5-12
5.9.	\hat{t} directed current density coefficients for the T_0 - T_{10} entire-domain modes, grouped by Fourier mode	5-13
5.10.	$\hat{\phi}$ directed current density for the $n = 2$ entire-domain modes for $ka = 4.0$ illuminated by E_{ϕ}^{inc} at $\theta = 60^\circ$	5-15

Figure		Page
5.11.	Total \hat{t} and $\hat{\phi}$ directed current densities ($n = 0-5$) for $ka = 4.0$ illuminated by E_{ϕ}^{inc} at $\theta = 60^{\circ}$	5-16
5.12.	Backscatter from a PEC sphere using 5 subdomain segments, illuminated at $\theta = 90^{\circ}$ by E_{ϕ}^{inc}	5-18
5.13.	Backscatter from a PEC sphere using 5 entire-domain modes, illuminated at $\theta = 90^{\circ}$ by E_{ϕ}^{inc}	5-19
5.14.	Value of R as a function of t , t' , and ϕ'	5-21
5.15.	The integral of Z^{tt} as a function of minimum R for various orders of Gaussian quadrature integration.	5-22

List of Tables

Table		Page
3.1.	Chebyshev polynomials of the first kind.	3-7
5.1.	Average integration times	5-24
5.2.	Additional time required per Fourier mode to add an entire-domain mode	5-25
5.3.	Additional time required per Fourier mode to add a subdomain segment	5-26
5.4.	Summary of CPU time savings per Fourier mode	5-28

Abstract

Research into improved calibration targets for measurement of radar cross-section has created a need for the ability to accurately compute the scattering from perfectly conducting bodies of revolution. Common computational techniques use moment-method codes that employ subdomain basis functions to expand the unknown current density on segments of the surface. This approach has its shortcomings. Large numbers of basis functions are required to accurately describe the behavior of the induced current density. Also, increasing the number of basis functions to improve accuracy after an initial computation requires re-computation of previous results and lost processing time.

This research involves using basis functions to expand the unknown currents that have as their domain the entire length of the surface. Entire-domain basis functions are better able to model the current density on a smooth surface, and functions can be chosen that closely model the functionality of the expected current. Fewer modes are required resulting in smaller matrix sizes. In addition, accuracy can be increased by incrementally adding entire-domain modes while retaining previously computed results saving significant computation time.

Electric-field integral equations are developed and solved by an entire-domain implementation of the Method of Moments for a perfectly conducting sphere. Comparison is made to the exact Mie series. Convergence in fewer modes is demonstrated over an equivalent application of subdomain pulses. Matrix fill time saves as much as hours over subdomain discretization.

COMPUTATION OF SCATTERING FROM BODIES OF REVOLUTION USING AN ENTIRE-DOMAIN BASIS IMPLEMENTATION OF THE MOMENT METHOD

I. Introduction

Throughout history, many military operations, large and small, have been successful due to efforts to ensure surprise and improve survivability. In modern times, this has not changed. Stealth technology is essential in both of these areas. Incorporating stealth on today's complicated, hi-tech battlefield, however, requires technically advanced and costly equipment and weapons. Although achieving military stealth involves many scientific and non-scientific disciplines, one area of intensive research centers on reducing the radar cross-section (RCS) of aircraft and other weapon systems. In the process of design, test, modification, and use of these systems, measurement of the systems or components of the systems on controlled ranges is required. The RCS must be determined with extreme accuracy, ensuring that the RCS measured is that of the system and not of the system interacting with the background of the measurement range. Any effects of the measurement chamber or background must be subtracted out. Calibration involves a transfer process whereby the corrections for the radar measurement errors are transferred from a known calibration target to the target under test. Measurements are made of the fields scattered by the target and its mount, \bar{E}_T^s , the target mount alone, \bar{E}_{TM}^s , a calibration object and its mount, \bar{E}_C^s , and the calibration object mount alone, \bar{E}_{CM}^s . A calibrated measurement of the target, σ_T is obtained with vector background subtraction using the formula,

$$\sigma_T = \left| \frac{\bar{E}_T^s - \bar{E}_{TM}^s}{\bar{E}_C^s - \bar{E}_{CM}^s} \right|^2 \sigma_{cal}, \quad (1.1)$$

where σ_{cal} is the calculated RCS of the simple calibration target used. The quantity $\bar{E}_T^s - \bar{E}_{TM}^s$ is assumed to be a *clean* measurement of the target alone. Likewise, the quantity $\bar{E}_C^s - \bar{E}_{CM}^s$ is assumed to be a clean measurement of the calibration object alone.

A perfectly conducting sphere with its Mie series solution is commonly used as a calibration object. Other perfectly conducting bodies of revolution (BOR) may also be used—and may produce a better calibration. For example, the geometry of a right-circular cylinder eliminates certain interactions between the itself and the pylon on which it is mounted. Use of other BORs, however, is dependent upon the ability to calculate, or otherwise determine, the expected scattering to within a specified tolerance.

Current computer codes which calculate the scattering from bodies of revolution implement the Method of Moments. They subdivide the scattering surface into sections and use piecewise expansions of the unknown current density in an integral equation that describes the scattering while satisfying boundary conditions. The method of expanding the current on sub-sections of the surface results in two deficiencies. First, a prohibitively large number of these expansion functions are required to accurately describe the current density on electrically large bodies. Second, if sufficient accuracy is not obtained, a re-sectionalizing and re-calculation of the current density on the surface is required, resulting in lost computational time.

The approach proposed here is to expand the unknown current in the equations using functions which have the entire length of the surface as their domain. Functions are chosen that better represent the expected current density on the surface. The continuous nature of entire-domain functions allows them to better describe the current density on a smooth surface such as that of a BOR. Also, since re-discretization is not required to add additional expansion terms, accuracy can be improved without discarding previous calculations. Both of the shortcomings described for subdomain sectionalization are avoided.

The goal of this research is to demonstrate the utility of entire-domain basis functions in computing the scattering from bodies of revolution. Chapter II briefly outlines the Moment Method which is used to solve the radar scattering equations. It also describes subdomain basis functions that are commonly used to expand the unknown current density in the Moment Method solution. Entire-domain basis functions are introduced and the Chebyshev polynomials are chosen as a suitable family of expansion functions. Advantages and disadvantages are discussed for each type of function. An electric-field integral equation is developed in Chapter III for scattering from an arbitrary body of revolution.

The Chebyshev polynomials are then used in Chapter IV as the basis for expanding the unknown current density induced on a perfectly conducting sphere by plane wave excitation. The resulting matrix equations are implemented in a computer code and solved. The data reported in Chapter V demonstrates that the RCS can be computed in fewer entire-domain basis expansion modes than subdomain basis functions under the same conditions. An analysis of solution matrix fill time and potential savings is also performed. Chapter VI summarizes the results. Although it is shown that fewer entire-domain modes are required for the RCS computation, the singular nature of the integrals adds to the complexity of their robust implementation. The method of equivalent separation of the testing functions and basis functions used in subdomain methods did not yield an accurate solution for spheres of small electrical size. A more rigorous handling of the singularity and other recommendations for further research are suggested. The computer code and additional data are included in Appendix A and B, respectively.

II. Background

The problem of improving the accuracy and computation time of calculating the scattering from bodies of revolution centers on the numerical solution. An important step in a numerical solution is the choice of an appropriate basis function set by which to expand the unknown quantity. This chapter discusses the numerical method that will be used to solve the integral equations that describe the scattering from a body of revolution caused by an incident plane-wave. It also outlines in some detail the various types of basis functions and reasons for their consideration. Finally, justification for the choice of entire-domain basis functions is given.

2.1 Numerical Solution by the Method of Moments

While several methods exist for determining an asymptotic, or high frequency, approximate solution to a scattering problem, the task here is to find a solution that converges to the exact solution in regions where the asymptotic methods fail. One such method, the Method of Moments, produces a solution that can converge to the exact solution. This method is the foundation for many variants of differing names.

The Method of Moments was first developed to solve elastodynamic problems and later generalized to a method of solution for a wide variety of problems involving linear integral and differential operations [14]. Also called the Moment Method, it is a numerical technique by which a linear operator equation—one in which the unknown quantity is imbedded in an integrand or the argument of a differentiation and cannot be solved for analytically—can be solved approximately by transforming the operator equation into a system of linear equations. Once the problem is formulated by this method, the solution comes by computing the inverse matrix and performing a matrix multiplication. An integro-differential equation such as the one that will be developed for plane-wave scattering from bodies of revolution can be written as a linear operator acting upon the unknown current density to produce a functional effect. Such an operation is written mathematically as

$$f = L[u], \tag{2.1}$$

where L is the linear operator, u is the unknown function, and f is the effect which is often called the forcing function. The unknown quantity is expanded into a series of terms. Each term is one of a set of linearly independent functions—called basis functions—multiplied by a coefficient which describes that term's relative importance to the total sum. However, even with computers, an infinite number of terms cannot be handled computationally, so the series is truncated to a finite series of terms plus a final term which represents all remaining terms (the error, ϵ),

$$u = \sum_{n=-\infty}^{\infty} I_n \psi_n \quad (2.2)$$

$$= \sum_{n=-N_1}^{+N_2} I_n \psi_n + \epsilon. \quad (2.3)$$

Or, writing as a one-sided sum,

$$u = \sum_{n=0}^{+N} I_n \psi_n + \tilde{\epsilon}. \quad (2.4)$$

Substituting the above expression for u into Equation (2.1), the constants can pass through the operator because of its linearity giving

$$L \left[\sum_{n=0}^{+N} I_n \psi_n + \tilde{\epsilon} \right] = f \quad (2.5)$$

$$\sum_{n=0}^{+N} I_n (L[\psi_n]) + r_\epsilon = f, \quad (2.6)$$

where r_ϵ is called the residual. The residual is then minimized by taking an inner product with a family of testing functions, θ_m , and forcing it to be orthogonal to the testing function. Galerkin does this by choosing $\psi_n = \theta_m$ [11]. For many functions involving complex calculations, a suitable inner product is

$$\langle \theta_m, \psi_n \rangle = \int \int_S \theta_m^* \cdot \psi_n ds. \quad (2.7)$$

Applying this inner product to Equation (2.6) and choosing to enforce $\langle \theta_m, r_\epsilon \rangle = 0$ results in a system of linear equations,

$$\sum_{n=0}^N I_n \langle L[\theta_m, \psi_n] \rangle - \langle \theta_m, f \rangle = 0, \quad m = 0, 1, 2, \dots, N. \quad (2.8)$$

The choice of N testing functions and N basis functions leads to a system of N equations with N unknowns, I_n . Rearranging gives

$$\langle \theta_m, f \rangle = \sum_{n=0}^N I_n \langle L[\theta_m, \psi_n] \rangle, \quad m = 0, 1, 2, \dots, N, \quad (2.9)$$

which can be easily written in simple, block matrix notation

$$[V]_{N \times 1} = [Z]_{N \times N} [I]_{N \times 1}, \quad (2.10)$$

where

$$\begin{aligned} [V]_m &= \langle \theta_m, f \rangle \\ [Z]_{mn} &= \langle L[\theta_m, \psi_n] \rangle \\ [I]_n &= I_n \end{aligned}$$

$$\begin{aligned} \text{for } m &= 0, 1, 2, \dots, N \\ n &= 0, 1, 2, \dots, N. \end{aligned} \quad (2.11)$$

When solved for the unknown,

$$[I]_{N \times 1} = [Z]_{N \times N}^{-1} [V]_{N \times 1}, \quad (2.12)$$

where the elements of $[I]$ are the coefficients of the expansion terms of the unknown quantity in the original operator equation. The accuracy of the numerical expansion is limited by the number of expansion terms, N .

2.2 Choosing a Basis Function

Although there are infinitely many functions which could be used as basis functions, an illogical choice of functions may limit the accuracy that can be obtained from the solution or may demand a prohibitively large number of functions for convergence. An appropriate basis set for calculating the scattered electromagnetic fields from a body contains functions that approximate the suspected current density on the surface of the body (rapid convergence), and have inter-function relationships that offer numerical advantages in the computation process (saved computation time). It should be noted that some functions may meet the requirements for a basis set, but may never be able to approach the exact solution with accuracy. This situation would occur, for example, if one were to attempt a solution by using basis functions that have smoother properties than the unknown being represented [1]. Factors affecting the choice of a basis function set involve the desired solution accuracy, the relative complexity of the resulting matrix entries, and the computational constraints (resources and time) that limit the ultimate matrix size [11].

2.2.1 Subdomain Basis Functions. One of the simplest, and therefore most common, basis sets that are used are sets of subdomain functions. That is to say they are functions that are defined only over the domain of consecutive sections of the structure. A surface is discretized by dividing it into N sections. The sections need not be of equal size but commonly are for computational simplicity. A function is defined over the limits of each segment. Simple functions may be a pulse (constant amplitude), a triangle, an arc of a sinusoid, etc. The unknown current or other quantity being calculated is then approximated by multiplying each piecewise function by an amplitude factor. This is described mathematically by the Equation (2.13) where $f(x)$ is the unknown function being approximated, n is an index for each section, a_n is the amplitude factor and $g_n(x')$ is the basis function,

$$f(x) \simeq \sum_n a_n g_n(x'). \quad (2.13)$$

Given the subdivision of an axis shown in Figure 2.1, pulse—or piecewise constant—basis functions are placed on each section. The pulse function is defined by

$$g_n(x') = \begin{cases} 1 & x'_{n-1} \leq x' \leq x'_n \\ 0 & \text{elsewhere} \end{cases} . \quad (2.14)$$

The height of each pulse corresponds to the a_n for that section. The curve, $f(x)$, represented by the semi-circle is approximated by the pulses. An example is Glisson's use of pulse basis functions to expand the current in his body of revolution solution [4].

Triangular—or piecewise linear—basis functions are similarly used, but they are usually defined with a domain that covers two consecutive segments. They are used in an overlapping fashion as shown in Figure 2.2 so that, when summed, the amplitude approximates the desired curve. Triangular expansion functions are useful in that they generally simplify the evaluation of the integro-differential operator by approximating the curve over each segment as linear. Both Mautz' formulation [8] and Rogers' JRMBOR [13] are examples of the use of triangular basis functions. The triangle basis functions approximate the unknown curve with straight lines whose derivatives are constants. Many moment method based computer codes use triangular basis functions because they produce a continuous approximation to the current.

Subdomain expansion functions are not advantageous when it comes to adding more terms to the expansion to increase accuracy. Prior results based upon an N -segmented, equal-interval domain must be discarded to re-discretize the domain into greater than N segments.

2.2.2 Entire Domain Basis Functions. Basis functions may also be defined over the entire length of a surface under consideration. Such functions are appropriately called entire domain basis functions. Equation (2.13) is still valid with an appropriate entire-domain definition of $g_n(x')$. Since the structure is not segmented as in the case of subdomain basis functions, each expansion term, n , is referred to as a *mode* rather than a section or a segment.

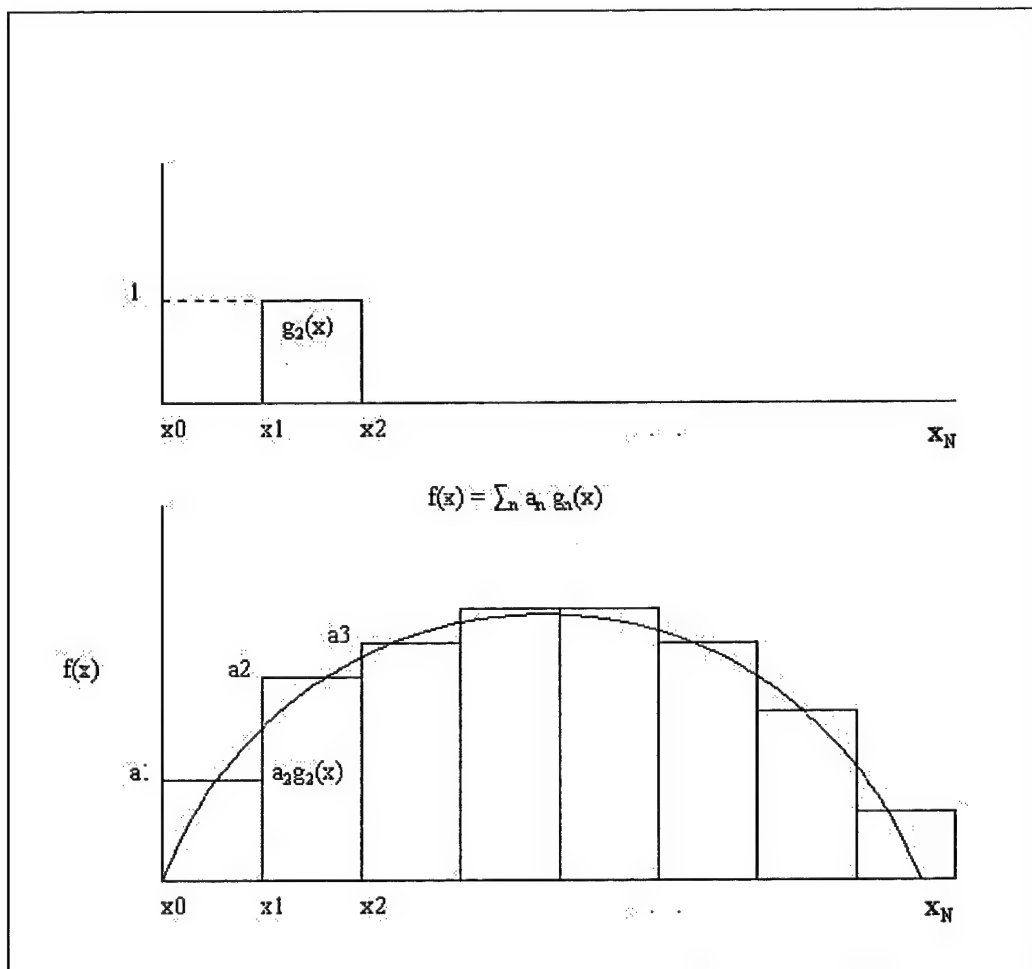


Figure 2.1 Pulse (piecewise constant) subdomain basis functions.

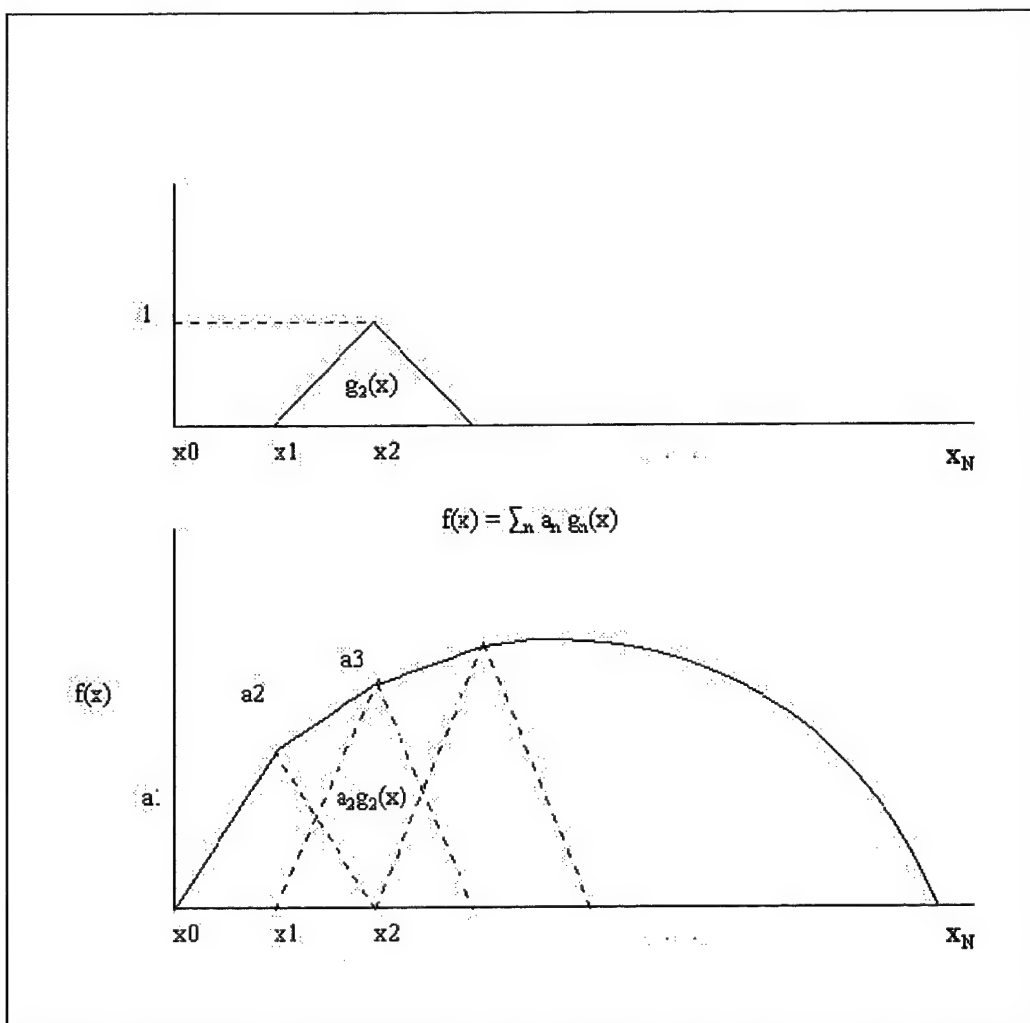


Figure 2.2 Triangular (piecewise linear) subdomain basis functions.

A familiar example of entire domain basis functions is the Fourier series in which a function is expanded in terms of exponentials (or sines and cosines),

$$x(\phi) = \sum_{n=-\infty}^{\infty} c_n e^{jn\phi}, \quad (2.15)$$

$$c_n = \int_{-\pi}^{\pi} x(\phi) e^{-jn\phi} d\phi. \quad (2.16)$$

An electrical pulse can be approximated in this way by adding together higher and higher orders of sinusoids from an oscillator until the edges of the pulse are sufficiently steep and the center ripple is sufficiently small for a given application. Balanis [2] points out that an entire domain sine is an appropriate basis for the current on a dipole antenna because the current is known to be zero at the ends and to oscillate approximately as a sine between the ends according to the frequency of the excitation. Poulsen [12] has experimented with sine and cosine basis functions for computing the fields induced on a frequency-selective surface of crossed-dipole arrays. While no evidence of any other use of entire-domain basis functions for computing the scattering from bodies of revolution was found, Kitazawa [7] and Butler [3] used Chebyshev polynomials to solve for the fields resonant in illuminated rectangular slots and waveguides.

Unlike subdomain basis functions, which when the interval is divided into sufficiently many intervals can approximate an arbitrary curve with the appropriate amplitudes applied, entire-domain modes can only be used effectively when the general nature of the curve is known *a priori* allowing choice of a basis that exhibits similar features [1]. This can be a disadvantage or an advantage depending upon the extent of information known or assumed about the problem at hand. A clear advantage of entire-domain basis functions is that if accuracy is not sufficient for an initial finite number of modes, additional modes can be added to the expansion while retaining the sum of previous modes.

2.2.3 Physical Basis Functions. One subset of entire domain basis functions is physical basis functions. These functions are unique in that they are based upon knowledge of current components that have actual physical interpretations. For example, some bodies exhibit scattering currents that can be traced to actual physical features or properties of

the body. Kent [6] found them useful in reducing matrix size in the solution of scattering from a dielectric coated strip. Physical basis functions are particularly useful for bodies of larger electrical size because they can reduce the order of the system to be solved.

2.2.4 Hybrid Basis Functions. Some methods may use several different types of basis functions simultaneously. One hybrid method involves using basis functions which represent the current as determined by a high frequency asymptotic approach such as Physical Optics or Geometrical Theory of Diffraction and combining it with subdomain basis functions near edges or other singularities [15]. This approach also has as its goal reducing the order of the system of equations to be solved which has benefits for solutions to problems involving electrically large bodies.

Combining physical basis functions with other basis functions may also be useful. A large body may be analyzed with physical basis functions and subdomain basis functions, for example. Physical basis functions are used to reduce the number of unknowns over electrically large regions, and subdomain basis functions are used to increase accuracy near edges or other smaller features.

2.2.5 Vector Basis Functions. The subdomain and entire-domain basis functions as described above have only employed a scalar representation which can be used in the solutions to three-dimensional problems by separately expanding the coordinate components of the unknown function. Under some conditions, this may not be desirable. If a problem centers on the solution at interfaces between different media, a boundary condition can be difficult to impose on an expansion that does not naturally separate into components along the boundary. Also, scalar expansions tend to be continuous, while with some vector quantities, enforcing this characteristic can introduce additional errors. Peterson shows that vector basis functions provide not only a function amplitude in a region, but a direction as well [11]. Figure 2.3 shows a notional example of directional functions within a triangular, multi-dimensional, subdomain cell. The vector basis functions can be defined appropriately at medium interfaces to satisfy continuous or discontinuous boundary conditions.

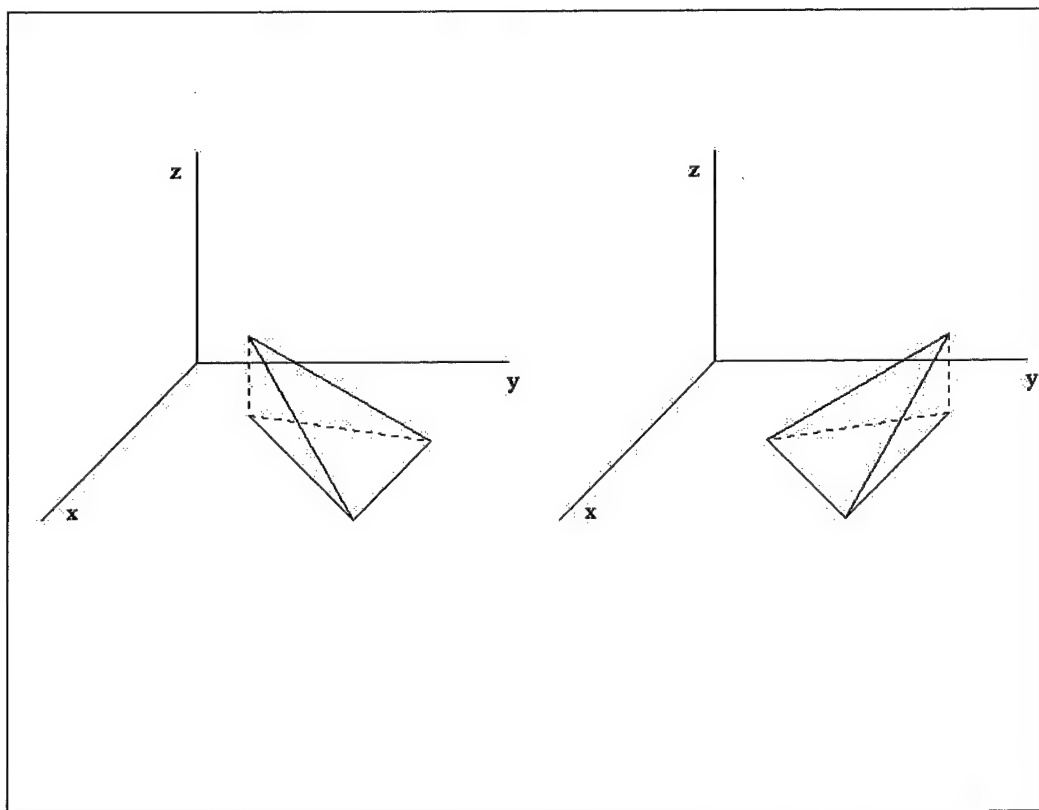


Figure 2.3 A notional example of a directional (vector) basis function on a surface cell.

2.3 Testing Functions

In order to determine the electromagnetic scattering from a body of revolution, the body is illuminated by an incoming wave and measurements are made at various points around the body to determine the scattering pattern. Accuracy depends upon the number of measurements made as well as the type of measuring device used. This measurement is accomplished numerically by means of testing functions placed around the body. Just as in the case of the basis functions used to expand the unknown current, the testing functions can be subdomain or entire-domain functions. The measurement of the scattering by each testing function *mode* can be thought of as a passive measurement of the scattering of the basis function modes which is induced by the incident wave. Electromagnetic reciprocity also allows thinking about this as the same problem in reverse. In this case, the body is excited by each test function which results in scattering by each basis function. The resulting fields are then measured. It is from this point of view that the numerical solution is developed. The reaction of the basis functions to each testing function is computed via an inner product.

Any number of kinds of testing functions exist. However, two kinds are commonly used because of the numerical advantages they offer. The first, and possibly the most commonly used, type is the Dirac delta distribution. In an integral equation, these functions allow elimination of one dimension of integration for each dimension in which they are used, thereby simplifying the numerical computation. For this simplicity, a trade-off is made by relaxing the boundary conditions so that they are only enforced at discrete points. Therefore, proper placement of the points is important.

Another possible choice of testing functions is a set of functions identical to the expansion basis functions. This is known as Galerkin's method. For certain integral equations, choosing testing functions equal to the basis functions allows an orthogonal projection of the unknown quantity onto the basis functions resulting in numerical convergence in the limit as the number of basis functions goes to infinity. The integral operators that arise in electromagnetics are generally not quite so ideal. However, Galerkin's method is often chosen for other reasons, one being that its use with electrical field integral equations produces matrices with diagonal symmetry. This permits an approximately 50% reduc-

tion in matrix fill computation time. This choice is acceptable in electromagnetic integral equations because even in the case where orthogonality is possible, an infinite number of functions can never be used. An error always exists and is monitored and controlled by the number and type of functions used [11].

2.4 Summary and Implications to Bodies of Revolution

The types of basis functions that exist are as varied as the types of problems to be solved. The categories include subdomain functions, entire-domain functions, hybrid basis functions, and directional (vector) functions. The problem of interest here is one of computing the scattering from a body of revolution in free space. While subdomain basis functions are commonly used, they are not the most time-efficient choice for a desired accuracy. In this development, the surface shape of the body is kept arbitrary throughout the solution, eliminating the usefulness of physical basis functions. Also, since this problem is posed as a free-space problem (constant medium), vector basis functions are not necessary or helpful. Choosing entire-domain basis functions offers several desired advantages. Using entire-domain basis functions results in a smoother approximation to the actual current density than using subdomain basis functions. An accurate approximation of the current density is also possible in fewer modes assuming an appropriate entire-domain function is used (exact convergence is only possible if the basis function is also an exact solution). Lastly, computational time is saved due to the ability to incrementally monitor and add modes as required without re-computation of previous modes. In using entire-domain basis functions, proper placement of delta testing functions is not obvious and Galerkin's method is used. The integral equation derived in Chapter III is written as a matrix equation in Chapter IV for an arbitrary choice of basis and testing functions. Chebyshev entire-domain basis functions and Galerkin testing are used to generate the results in Chapter V.

III. Theory

In this chapter, the geometry for an arbitrary perfectly electric conducting (PEC) body of revolution is established. For a PEC body, the electric field components tangential to the surface must vanish at every point on the surface. Using this boundary condition, an electric field integral equation is formed to describe the scattering from the body. Also, the Chebyshev polynomials that will be used as basis functions in the numerical solution of the integral equation are described. The conventions, notation, and overall development follows that of Mautz and Harrington [9].

3.1 Definition and Geometry

A body of revolution is created by rotating a generating arc around an axis. Consider a generating arc defined by a continuous function in the XZ -plane whose endpoints are on the z -axis. The function may be defined in piecewise fashion, and does not need to be differentiable in the sense that the resulting curve can have corners. This function is then rotated axially around the z -axis to create a closed surface that is symmetric in the cylindrical direction ϕ . The surface and the volume it encloses is called a body of revolution because it is created by revolving a function around an axis, not because of any motion of the body itself. Such a body of revolution is depicted in Figure 3.1. Although the body is depicted as being defined entirely in the positive- z half-space, this is not necessary. However, the equations used herein to define the geometric parameters of the body are written assuming positive- z and may not be valid for other conventions.

It is convenient to write the generating arc as a parametric equation of a curvilinear coordinate system on the surface of the body of revolution. In Figure 3.1, ρ , ϕ , and z are the ordinary cylindrical coordinates and \hat{t} and $\hat{\phi}$ are orthogonal unit vectors at a point, S , on the surface which satisfy $\hat{\phi} \times \hat{t} = \hat{n}$. Letting t_0 be the zero arclength point of the generating arc (located at the origin), \hat{t} points in the direction of increasing arclength, and $\hat{\phi}$ points in the direction of increasing cylindrical ϕ . This leads to choosing \hat{n} as the outward normal unit vector to the surface S . The body of revolution is excited by an incident plane wave as shown in Figure 3.2. The vector \hat{k}_i indicates the direction of

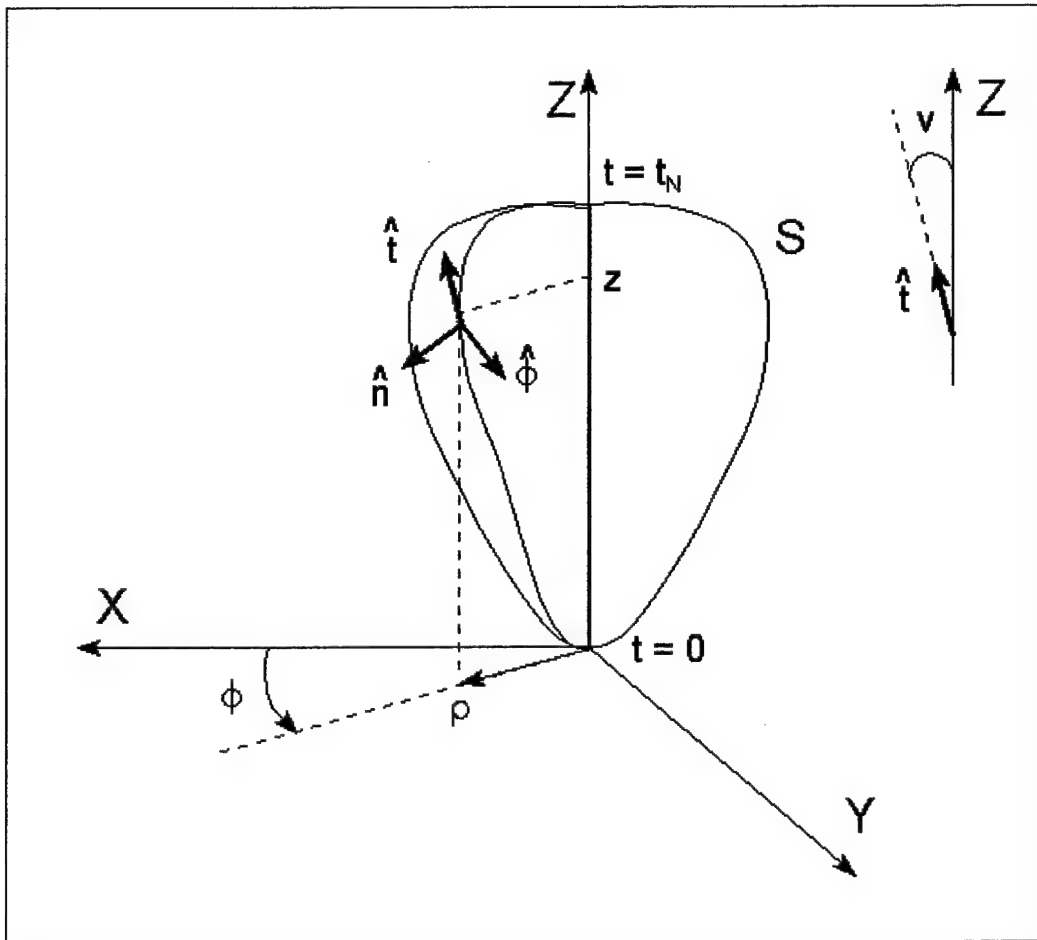


Figure 3.1 Geometry of the body of revolution

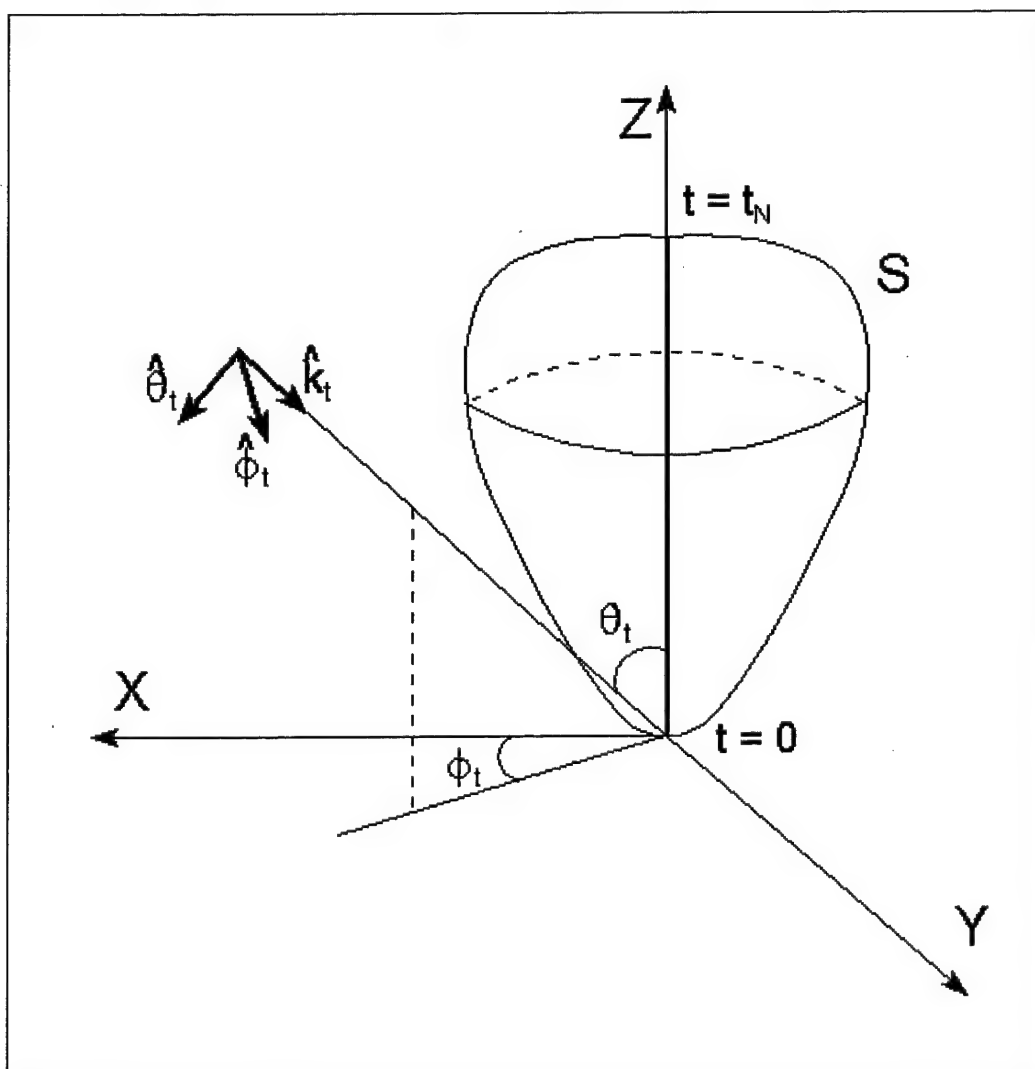


Figure 3.2 A plane wave incident on the body of revolution

plane wave propagation. The coordinates ϕ_t and θ_t indicate the transmitter location. The vectors $\hat{\phi}_t$ and $\hat{\theta}_t$ are unit vectors in the ϕ_t and θ_t directions, respectively. The resulting scattered field components will be measured in the monostatic (backscatter) direction. It will be assumed for the purposes of this problem that the body of revolution has a perfect electrically conducting surface.

3.2 Integral Equations

The problem of scattering from the body of revolution is solved as an electromagnetic boundary value problem by forming either an electric field integral equation or a magnetic field integral equation. It has been shown by Mautz and Harrington [9] that the solutions to the E-field and H-field integral equations deteriorate near internal resonances of the conducting surface, but a solution involving a weighted linear combination of the E-field and H-field integral equations does not. However, they also show that although the error in current density near the resonances using the E-field integral equations can be tremendous, the error in scattering cross-section is quite small compared to that of the H-field solution and is comparable to that of the combined field solution. Using both E-field and H-field integral equations in a combined equation effectively doubles the computation time for each element in the solution while giving minimal improvement in the scattering cross-section data. For this reason, development and use of the E-field integral equation for this concept demonstration is considered sufficient. The H-field integral equation can be similarly derived and used to trade computation time for increased accuracy.

Maxwell's equations require that the tangential electrical fields at the surface of a perfect electrical conductor sum to zero. This boundary condition is written as

$$\bar{E}_{tan}^{inc} + \bar{E}_{tan}^s = 0, \quad (3.1)$$

where \bar{E}^{inc} is the incident electric field and \bar{E}^s is the field scattered from the surface. The subscript *tan* denotes the tangential component on S . The incident field is defined to be

either $\hat{\theta}$ or $\hat{\phi}$ directed and is written as

$$\bar{E}_{\theta}^{inc} = \hat{\theta} k \eta e^{-j\hat{k}_t \cdot \bar{r}} \quad (3.2)$$

or

$$\bar{E}_{\phi}^{inc} = \hat{\phi} k \eta e^{-j\hat{k}_t \cdot \bar{r}}, \quad (3.3)$$

where k is the propagation constant, η is the intrinsic impedance (377Ω for free-space), and \bar{r} is the radius vector from the origin to a point on the surface. The scattered field is found via the magnetic vector potential, \bar{A} and the electric scalar potential, Φ_e ,

$$\bar{E}^s = -j\omega\bar{A}(\bar{J}) - \nabla\Phi_e(\bar{J}). \quad (3.4)$$

The magnetic vector potential, \bar{A} , and the electric scalar potential, Φ_e , written in terms of the free-space Green's function are [2]

$$\bar{A}(\bar{J}) = \frac{\mu}{4\pi} \iint_S \bar{J}(\bar{r}') \frac{e^{jk|\bar{r}-\bar{r}'|}}{|\bar{r}-\bar{r}'|} ds' \quad (3.5)$$

$$\Phi_e(\bar{J}) = -\frac{1}{j\omega 4\pi\epsilon} \iint_S [\nabla \cdot \bar{J}(\bar{r}')] \frac{e^{jk|\bar{r}-\bar{r}'|}}{|\bar{r}-\bar{r}'|} ds'. \quad (3.6)$$

Here, \bar{r} and \bar{r}' are vectors to the measurement and source points, respectively. The quantity $\bar{J}(\bar{r}')$ is the electric current density on S , k is the propagation constant, and μ and ϵ are the permeability and permittivity, respectively. The operator $\nabla \cdot$ is the divergence. The quantity $|\bar{r} - \bar{r}'|$ can be written in terms of the cylindrical coordinates as

$$R = |\bar{r} - \bar{r}'| = \sqrt{(\rho - \rho')^2 + (z - z')^2 + 4\rho\rho' \sin^2\left(\frac{\phi - \phi'}{2}\right)} \quad (3.7)$$

where ρ , z , and ϕ are functions of arclength, t as shown in Figure 3.1. Similarly, ρ' , z' , and ϕ' are functions of t' . Substituting Equation (3.4) with (3.5), (3.6) and (3.7) into Equation (3.1) gives

$$\bar{E}_{tan}^{inc} - j\omega\mu 4\pi \iint_S \bar{J}(\bar{r}') \frac{e^{jkR}}{R} ds' + \frac{1}{j\omega 4\pi\epsilon} \iint_S [\nabla \cdot \bar{J}(\bar{r}')] \frac{e^{jkR}}{R} ds' = 0, \quad (3.8)$$

which is an electric field integral equation describing the tangential electric fields at the surface. This is a complicated integro-differential equation where \bar{J} is the unknown quantity which can be determined numerically using the Method of Moments. Once \bar{J} is known, it can be used to compute the scattered electric fields.

3.3 Chebyshev Polynomial Basis Functions

There are many entire-domain functions that could be used as a basis to expand the unknown current density on the surface of the body. Some common orthogonal functions to which the entire-domain of the generating arc could be mapped are sinusoids, Jacobi polynomials, Chebyshev polynomials, Legendre polynomials, Maclaurin series, Laguerre polynomials, and Hermite polynomials [10].

Since one of the purposes in using an entire-domain basis is to reduce the number of modes or terms required to approximate the current density when expanded as a series, the shape of the basis functions themselves should closely model the functionality of the expected current density. The function must also have higher modes that exhibit a sufficient degree of oscillatory behavior or other fluctuation in its derivatives to define the changes in the current density across the length of the body. The current density should be systematically improved by increasing the number of basis functions.

The Chebyshev polynomials of the first kind are found to have the required characteristics in the domain of $-1 \leq s \leq 1$. An additional advantage of this choice is that the positive and negative ends are symmetric and finite. Table 3.1 gives the functional form of the first nine polynomials which are illustrated in Figure 3.3. The polynomials are easily referenced in a computer code by a lookup table of the coefficients. The higher order polynomials can be generated by a recursion relationship [10],

$$T_n(x) = 2xT_{n-1}(x) - T_{n-2}(x). \quad (3.9)$$

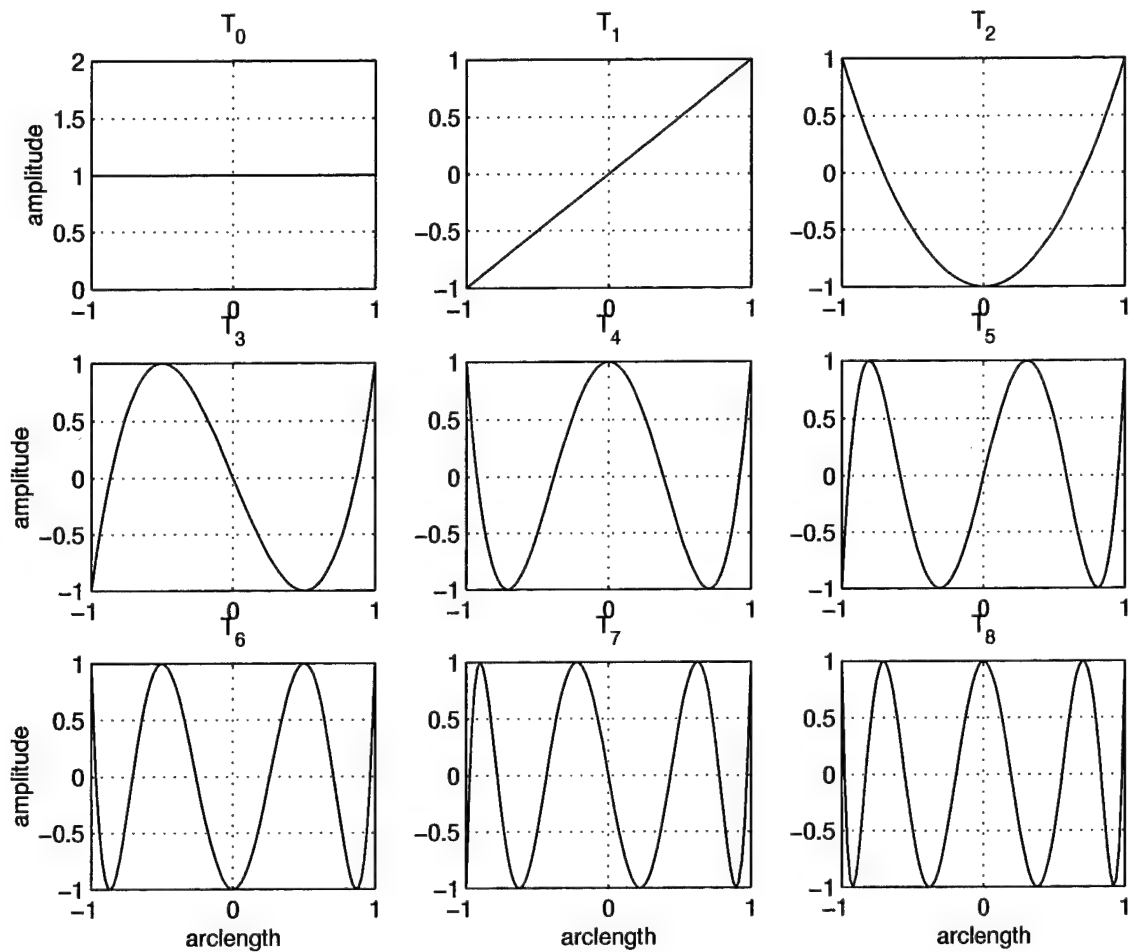


Figure 3.3 The first nine modes of the Chebyshev polynomial of the first kind (T_0 - T_8).

$$\begin{aligned}
 T_0 &= 1 \\
 T_1 &= x \\
 T_2 &= 2x^2 - 1 \\
 T_3 &= 4x^3 - 3x \\
 T_4 &= 8x^4 - 8x^2 + 1 \\
 T_5 &= 16x^5 - 20x^3 + 5x \\
 T_6 &= 32x^6 - 48x^4 + 18x^2 - 1 \\
 T_7 &= 64x^7 - 112x^5 + 56x^3 - 7x \\
 T_8 &= 128x^8 - 256x^6 + 160x^4 - 32x^2 + 1
 \end{aligned}$$

Table 3.1 Chebyshev polynomials of the first kind.

The Chebyshev basis functions are orthogonal with respect to a weighting function, $w(x) = 1/(1 - x^2)^{1/2}$,

$$\int_{-1}^1 T_m(x)T_n(x)(1 - x^2)^{-1/2} dx = \begin{cases} 0, & m \neq n \\ \pi/2, & m = n \neq 0 \\ \pi, & m = n = 0 \end{cases} . \quad (3.10)$$

However, the weighting is not necessary for convergence if the operator, L , is self-adjoint with respect to the inner product, $\langle La, b \rangle = \langle a, Lb \rangle$, and is positive definite, $\langle a, La \rangle > 0$ for all nonzero a [11]. The linear independence of the Chebyshev polynomials is sufficient to force the residual error of the inner product to zero and establishes the convergence of the finite expansion. In practice, Galerkin testing is used with the electric-field integral equation without regard to true orthogonality because it produces matrices with diagonal symmetry reducing the required computations.

In summary, an electric-field integral equation, Equation (3.8) was formed as a function of the unknown current density. The equation applies on the surface and is based on the vanishing tangential electric fields. Also, the Chebyshev polynomials were defined and will be used to expand the current density in the numerical solution outlined in Chapter IV.

IV. Application to the Integral Equation

In this chapter, the electric field integral equation given in Equation (3.8) is solved for the unknown current density by means of the Method of Moments using entire-domain basis functions.

Equations (3.1) and (3.4) are rewritten in terms of the tangential component of the incident field, \bar{E}_{tan}^{inc} ,

$$\begin{aligned}\bar{E}_{tan}^{inc} &= -\bar{E}_{tan}^s \\ &= -[-\nabla\Phi_e(\bar{J}) - j\omega\bar{A}(\bar{J})]_{tan}.\end{aligned}\quad (4.1)$$

Define a linear operation on the unknown current density, \bar{J} , as

$$L(\bar{J}) = [j\omega\bar{A}(\bar{J}) + \nabla\Phi(\bar{J})]_{tan}.\quad (4.2)$$

The current density is written in a series expansion of linearly independent basis functions

$$\bar{J} = \sum_j I_j \bar{\psi}_j.\quad (4.3)$$

Because the unknown currents \bar{J} are periodic in ϕ (body of revolution), each $\bar{\psi}_j$ can be represented as a Fourier series in ϕ . The Fourier series is an entire-domain expansion where the domain is $0 \leq \phi \leq 2\pi$ and the basis is the complex exponential $e^{jn\phi}$ which represents a Fourier mode indexed by n . Now,

$$\bar{J}(t', \phi') = \sum_n \sum_j I_{nj} \bar{J}_j(t') e^{jn\phi'}.\quad (4.4)$$

Primes are used here and in the remainder of this document to denote association with a source (surface scattering) point. Unprimed quantities refer to field points where the electric field is measured or tested. The current density at each point, t , along the generating arc is completely described by the sum of the current densities in two orthogonal, curvilinear component directions, \hat{t} and $\hat{\phi}$. Separately expanding $I_{nj}\bar{J}_j$ in each direction

gives

$$\begin{aligned} I_{nj} \bar{J}_j &= I_{nj}^{t'} \bar{J}_j^{t'} + I_{nj}^{\phi'} \bar{J}_j^{\phi'} \\ &= \hat{t} I_{nj}^{t'} f_j(t') + \hat{\phi} I_{nj}^{\phi'} f_j(t'), \end{aligned} \quad (4.5)$$

where t' is a point on the generating arc, $0 \leq t' \leq t_N$ and $f_j(t')$ is the j 'th basis function.

The current expansions are, therefore, defined as

$$\begin{aligned} \bar{J}_{nj}^{t'} &= \hat{t}' f_j(t') e^{jn\phi'} \\ \bar{J}_{nj}^{\phi'} &= \hat{\phi}' f_j(t') e^{jn\phi'}. \end{aligned} \quad (4.6)$$

Substituting Equation (4.4) and (4.5) into Equation (4.3) gives a final expression for the current density,

$$\bar{J} = \sum_n \sum_j \left[\hat{t} I_{nj}^{t'} f_j(t') + \hat{\phi} I_{nj}^{\phi'} f_j(t') \right] e^{jn\phi'}. \quad (4.7)$$

The integral equations now can be written as

$$\bar{E}_{tan}^i = L \left[\sum_{n,j} I_{nj}^{t'} \bar{J}_{nj}^{t'} + \sum_{n,j} I_{nj}^{\phi'} \bar{J}_{nj}^{\phi'} \right]. \quad (4.8)$$

The linearity of L allows interchanging the order of summation and integration/differentiation, for finite sums, to produce

$$\bar{E}_n^i = \sum_{n,j} \left[I_{nj}^{t'} L \left(\bar{J}_{nj}^{t'} \right) + I_{nj}^{\phi'} L \left(\bar{J}_{nj}^{\phi'} \right) \right]. \quad (4.9)$$

Since each Fourier expansion mode is linearly independent from and orthogonal to every other, the above formulation is separable in n and involves a separate solution to determine the current coefficients for each Fourier mode. Rewriting as a separate equation for each n permits simplification of the notation by dropping the subscript n ,

$$\bar{E}^i = \sum_j \left[I_j^{t'} L \left(\bar{J}_j^{t'} \right) + I_j^{\phi'} L \left(\bar{J}_j^{\phi'} \right) \right], \quad \forall n. \quad (4.10)$$

Testing functions are chosen equivalent to the basis (current expansion) functions according to Galerkin's method,

$$\begin{aligned}\bar{W}_{mi}^t &= \hat{t}f_i(t)e^{jm\phi} \\ \bar{W}_{mi}^\phi &= \hat{\phi}f_i(\phi)e^{jm\phi}.\end{aligned}\quad (4.11)$$

Multiplying both sides of the integral Equation (4.10) by the testing functions and using the inner product of Equation (2.7) results in

$$\left\langle \sum_i \bar{W}_{mi}, \bar{E}_{tan}^{inc} \right\rangle_n = \left\langle \sum_i \bar{W}_{mi}, \sum_j I_j L(\bar{J}_j) \right\rangle_n. \quad (4.12)$$

Because of the Fourier orthogonality, the inner product is zero for $m \neq n$ and non-zero for $m = n$. From now on, only the subscript n is used. Equation (4.12) expanded in matrix form is

$$\begin{aligned}\begin{bmatrix} \langle \bar{W}_1, \bar{E}_{tan}^{inc} \rangle \\ \langle \bar{W}_2, \bar{E}_{tan}^{inc} \rangle \\ \vdots \\ \langle \bar{W}_N, \bar{E}_{tan}^{inc} \rangle \end{bmatrix}_n &= \begin{bmatrix} \langle \bar{W}_1, \sum_j I_j L(\bar{J}_j) \rangle \\ \langle \bar{W}_2, \sum_j I_j L(\bar{J}_j) \rangle \\ \vdots \\ \langle \bar{W}_N, \sum_j I_j L(\bar{J}_j) \rangle \end{bmatrix}_n \\ &= \begin{bmatrix} \langle \bar{W}_1, I_1 L(\bar{J}_1) \rangle & \langle \bar{W}_1, I_2 L(\bar{J}_2) \rangle & \cdots & \langle \bar{W}_1, I_N L(\bar{J}_N) \rangle \\ \langle \bar{W}_2, I_1 L(\bar{J}_1) \rangle & \langle \bar{W}_2, I_2 L(\bar{J}_2) \rangle & \cdots & \langle \bar{W}_2, I_N L(\bar{J}_N) \rangle \\ \vdots & & \ddots & \\ \langle \bar{W}_N, I_1 L(\bar{J}_1) \rangle & \langle \bar{W}_N, I_2 L(\bar{J}_2) \rangle & \cdots & \langle \bar{W}_N, I_N L(\bar{J}_N) \rangle \end{bmatrix}_n \\ &= \begin{bmatrix} \langle \bar{W}_1, L(\bar{J}_1) \rangle & \langle \bar{W}_1, L(\bar{J}_2) \rangle & \cdots & \langle \bar{W}_1, L(\bar{J}_N) \rangle \\ \langle \bar{W}_2, L(\bar{J}_1) \rangle & \langle \bar{W}_2, L(\bar{J}_2) \rangle & \cdots & \langle \bar{W}_2, L(\bar{J}_N) \rangle \\ \vdots & & \ddots & \\ \langle \bar{W}_N, L(\bar{J}_1) \rangle & \langle \bar{W}_N, L(\bar{J}_2) \rangle & \cdots & \langle \bar{W}_N, L(\bar{J}_N) \rangle \end{bmatrix}_n \begin{bmatrix} I_1 \\ I_2 \\ \vdots \\ I_N \end{bmatrix}_n \\ [V]_n &= [Z]_n [I]_n.\end{aligned}\quad (4.13)$$

Equation (4.13) represents, for each Fourier mode, N equations and N unknowns, I_n . Recall that \bar{W}_i and \bar{J}_j both have \hat{t} and $\hat{\phi}$ terms. This further expands Equation (4.13) into a pair of N equations for each component. Instead of doing this, however, the mathematics of linear algebra and the matrix notation, allow simultaneous solutions for the \hat{t} and $\hat{\phi}$ component equations by vertically stacking the equations. The impedance matrix, $[Z]$, contains the $(\bar{W}_i^t + \bar{W}_i^\phi) \cdot (\bar{J}_j^t + \bar{J}_j^\phi)$ cross-terms,

$$\begin{bmatrix} [V_n^t] \\ [V_n^\phi] \end{bmatrix} = \begin{bmatrix} [Z_n^{tt}] & [Z_n^{t\phi}] \\ [Z_n^{\phi t}] & [Z_n^{\phi\phi}] \end{bmatrix} \begin{bmatrix} [I_n^t] \\ [I_n^\phi] \end{bmatrix}, \quad \forall n \quad (4.14)$$

where,

$$\begin{aligned} V_n^t &= \langle \bar{W}_i^t, \bar{E}_{tan}^{inc} \rangle \\ V_n^\phi &= \langle \bar{W}_i^\phi, \bar{E}_{tan}^{inc} \rangle \\ Z_n^{tt} &= \langle \bar{W}_i^t, L(\bar{J}_j^t) \rangle \\ Z_n^{t\phi} &= \langle \bar{W}_i^t, L(\bar{J}_j^\phi) \rangle \\ Z_n^{\phi t} &= \langle \bar{W}_i^\phi, L(\bar{J}_j^t) \rangle \\ Z_n^{\phi\phi} &= \langle \bar{W}_i^\phi, L(\bar{J}_j^\phi) \rangle \\ I_n^t &= I_j^t \\ I_n^\phi &= I_j^\phi. \end{aligned} \quad (4.15)$$

4.1 The Impedance Matrix

Performing the inner products for $[Z_n]$ in Equation (4.15) results in the expressions given in Equations (4.16) through (4.19) below. The integration in ϕ has been performed analytically. The equations are found to match those given in by Mautz [9] if the operator, L , and the incident field, \bar{E}^{inc} , are scaled by $1/\eta$, where η is the intrinsic impedance. The integrations in ϕ' can be written as integrations over half a period due to the even and odd

symmetry of their integrands,

$$\begin{aligned} [Z_n^{tt}]_{ij} = & \int_t \int_{t'} j \left\{ k^2 \rho f_i(t) \rho' f_j(t') [G_2 \sin(v) \sin(v') + G_1 \cos(v) \cos(v')] \right. \\ & \left. - \frac{\partial}{\partial t} [\rho f_i(t)] \frac{\partial}{\partial t'} [\rho' f_j(t')] G_1 \right\} dt' dt \end{aligned} \quad (4.16)$$

$$[Z_n^{\phi t}]_{ij} = \int_t \int_{t'} -\rho f_i(t) \left\{ k^2 \rho' f_j(t') G_3 \sin(v') + \frac{n}{\rho} \frac{\partial}{\partial t'} [\rho' f_j(t')] G_1 \right\} dt' dt \quad (4.17)$$

$$[Z_n^{t\phi}]_{ij} = \int_t \int_{t'} \rho' f_j(t') \left\{ k^2 \rho f_i(t) G_3 \sin(v) + \frac{n}{\rho'} \frac{\partial}{\partial t} [\rho f_i(t)] G_1 \right\} dt' dt \quad (4.18)$$

$$[Z_n^{\phi\phi}]_{ij} = \int_t \int_{t'} j \rho f_i(t) \rho' f_j(t') \left(k^2 G_2 - \frac{n^2}{\rho \rho'} G_1 \right) dt' dt, \quad (4.19)$$

with the following definitions,

$$G_1 = \int_0^\pi \frac{e^{-jkR}}{kR} \cos(n\phi') d\phi' \quad (4.20)$$

$$G_2 = \int_0^\pi \frac{e^{-jkR}}{kR} \cos(\phi') \cos(n\phi') d\phi' \quad (4.21)$$

$$G_3 = \int_0^\pi \frac{e^{-jkR}}{kR} \sin(\phi') \sin(n\phi') d\phi' \quad (4.22)$$

$$R = \sqrt{(\rho - \rho')^2 + (z - z')^2 + 4\rho\rho' \sin^2\left(\frac{\phi'}{2}\right)}. \quad (4.23)$$

The quantities ρ , z , and v are functions of arclength, t as shown in Figure 3.1. Similarly, ρ' , z' , and v' are functions of t' . The $\phi - \phi'$ functionality in the expression for R is written as ϕ' only because of the rotational symmetry. This is shown by a simple change of variables in the integrals involving R . Note that replacing ij by ji in Equations (4.16) through (4.19) implies replacing t dependent quantities by t' dependent quantities, and vice-versa. The following symmetries are apparent (a result of Galerkin testing) and will reduce the number of computations required.

$$\begin{aligned} [Z_n^{tt}]_{ij} &= [Z_n^{tt}]_{ji} \\ [Z_n^{\phi t}]_{ij} &= - [Z_n^{t\phi}]_{ji} \\ [Z_n^{\phi\phi}]_{ij} &= [Z_n^{\phi\phi}]_{ji} \end{aligned} \quad (4.24)$$

4.2 The Voltage Matrix

The inner products of Equation (4.15) for the voltage matrix, $[V_n]$, give Equations (4.25) and (4.26). The voltage matrix represents the incident excitation of the system,

$$[V_n^t]_i = \int_t \int_\phi k \rho f_i(t) (\hat{t} \cdot \hat{u}^{inc}) e^{-\hat{k} \cdot \hat{r} - n\phi} d\phi dt \quad (4.25)$$

$$[V_n^\phi]_i = \int_t \int_\phi k \rho f_i(t) (\hat{\phi} \cdot \hat{u}^{inc}) e^{-\hat{k} \cdot \hat{r} - n\phi} d\phi dt, \quad (4.26)$$

where \hat{u}^{inc} is the polarization of the incident electric field, $\hat{\theta}^{inc}$ or $\hat{\phi}^{inc}$.

4.3 Scattered Field Equation

The current density induced on the surface of the body re-radiates to create the scattered field. Using the current density determined by the Moment Method solution, an equation can be derived based on reciprocity which describes the scattered field. A row matrix can be identified in the equation that parallels the voltage matrix of the previous section allowing it to be filled using the same computer subroutines. For this it is useful to rewrite the scalar potential in Equation (3.4) in terms of the magnetic vector potential,

$$\Phi_e = -\frac{1}{j\omega\mu\epsilon} \nabla \cdot \bar{A}. \quad (4.27)$$

The expression for \bar{E}^s becomes

$$\bar{E}^s = -j \frac{1}{\omega\mu\epsilon} \nabla(\nabla \cdot \bar{A}) - j\omega \bar{A}. \quad (4.28)$$

Balanis [1] notes that the first term in Equation (4.28) contains only variations of the order $1/r^2$, $1/r^3$, $1/r^4$, etc. The variation of order $1/r$ is contained in the second term and is the dominant variation. In the far-field (large r), the first term is neglected and the remaining radial component becomes negligible compared to the θ and ϕ components.

The field radiated in the far-zone is due to the current density on the surface. By reciprocity, this is equivalent to saying that the field on the surface is due to radiation from an infinitesimal current element in the far-zone. The field at the surface, S , is determined

by Equation (4.28) and is shown by Harrington [5] to be

$$\bar{E}_S^r(I_0 \hat{u}) = \frac{-jk\eta e^{jkr_r}}{4\pi r_r} I_0 \hat{u} e^{-j\bar{k}_r \cdot \bar{r}}, \quad (4.29)$$

where $I_0 \hat{u}$ is the current element vector pointing in the θ or ϕ direction, r_r is the distance from the far field point to the origin, r is the distance from the origin to a point on the surface, and \bar{k}_r is the propagation vector of the plane wave coming from the current element. Taking the inner product of \bar{E}_S^r and the current density expansion gives the magnitude of the scattered field due to \bar{J} in either the $\hat{\theta}$ or $\hat{\phi}$ direction,

$$E^s = \frac{-jk\eta e^{jkr_r}}{4\pi r_r} \sum_{n=-\infty}^{\infty} \begin{bmatrix} \bar{R}_n^t \\ \bar{R}_n^\phi \end{bmatrix}^T \begin{bmatrix} \bar{I}_n^t \\ \bar{I}_n^\phi \end{bmatrix} e^{jn\phi_r}, \quad (4.30)$$

where the superscript T signifies matrix transpose and the elements of the row matrix, $[R_n] = [R_n^t \ R_n^\phi]$ are given by

$$[R_n^t]_i = \int_t \int_\phi k \rho f_i(t) (\hat{t} \cdot \hat{u}^r) e^{-\bar{k} \cdot \bar{r} + n\phi} d\phi dt \quad (4.31)$$

$$[R_n^\phi]_i = \int_t \int_\phi k \rho f_i(t) (\hat{\phi} \cdot \hat{u}^r) e^{-\bar{k} \cdot \bar{r} + n\phi} d\phi dt, \quad (4.32)$$

where \hat{u}^r is the receiver polarization unit vector, $\hat{\theta}^r$ or $\hat{\phi}^r$. Comparison of Equations (4.31) and (4.32) with Equations (4.25) and (4.26) show that when the measured field unit vector is replaced by the incident field unit vector, the only difference is the sign on n . The following unit vector dot products are derived from the geometry and are tabulated here for use in the equations for $[V_n]$ and $[R_n]$,

$$\begin{aligned} \hat{t} \cdot \hat{\theta}^{r,t} &= -\sin(\theta^{r,t}) \cos(v) + \cos(\theta^{r,t}) \sin(v) \cos(\phi) \\ \hat{\phi} \cdot \hat{\theta}^{r,t} &= -\cos(\theta^{r,t}) \sin(\phi) \\ \hat{t} \cdot \hat{\phi}^{r,t} &= \sin(v) \sin(\phi) \\ \hat{\phi} \cdot \hat{\phi}^{r,t} &= \cos(\phi) \\ -\bar{k}^{r,t} \cdot \bar{r} &= kz \cos(\theta^{r,t}) + k\rho \sin(\theta^{r,t}) \cos(\phi), \end{aligned} \quad (4.33)$$

where $\theta^{r,t}$ is the transmitted and received electric field elevation angle, respectively (Figure 3.2). The angles ϕ and v are as shown in Figure 3.1.

4.4 Three-dimensional Scattering Cross-section

A useful measure of the scattering properties of a body is the *scattering cross-section*. This quantity describes the area that would be required to intercept the amount of power that a source would have to scatter isotropically to create the same power density at the receiver as does the actual scattering body [2]. Once the scattered electric field, E^s , is determined, this scattering cross-section can be calculated and is useful to compare the scattering of bodies of various sizes and shapes. For a three-dimensional body, the scattering cross-section, σ , is defined for plane-wave incidence as a ratio of the power in the scattered field to the power in the incident field [2]. Noting that the power is proportional to the field magnitude squared,

$$\sigma = \lim_{r \rightarrow \infty} 4\pi r^2 \left| \frac{\bar{E}^s}{\bar{E}^{inc}} \right|^2. \quad (4.34)$$

Writing the expression for scattered field in Equation (4.30) as a one-sided sum in n using the even and odd symmetries of the real and imaginary components of $e^{jn\phi_r}$ and allowing ϕ_r to equal zero (monostatic measurement) gives,

$$E^s(\bar{J}) = \frac{-j\eta e^{jk r_r}}{4\pi r_r} \left\{ [R_0^t][I_0^t] + [R_0^\phi][I_0^\phi] + \frac{1}{2} \sum_{n=1}^{\infty} \left([R_n^t][I_n^t] + [R_n^\phi][I_n^\phi] \right) \right\}. \quad (4.35)$$

Also, as an aid in the comparison of objects of different sizes at different frequencies, σ can be normalized with respect to the wavelength, $\lambda = 2\pi/k$, of the incident field. Substituting in $|E^{inc}| = k\eta$ from Equation (3.3), the normalized far field ($r \rightarrow \infty$) cross-section reduces to

$$\frac{\sigma}{\lambda^2} = \frac{1}{4\pi^3} \left| \frac{2\pi r_r \bar{E}^s(\bar{J})}{\eta} \right|^2. \quad (4.36)$$

4.5 Summary

The boundary condition on the tangential electric fields at the surface of the PEC body was used in Chapter III to develop an integral equation to which the Moment Method was applied in this chapter. Matrix elements were defined in terms of an inner product with Galerkin testing functions for a *voltage matrix* and an *impedance matrix*. The elements of a *scattering matrix* were also defined. These elements were computed using a computer and the system of equations was solved. The results are reported in Chapter V.

V. Results

Both perfectly electrically conducting spheres and closed right-circular cylinders are used as calibration objects on radar ranges. An exact solution exists for the scattering from spheres. Desire for the ability to accurately calculate the scattering from cylinders is, in part, the motivation for this research. The equations of the previous chapter are derived for arbitrary body of revolution geometries and choice of expansion function. However, since the exact solution is known for a sphere, it is chosen for the *proof of concept* data presented in this chapter.

The impedance matrix and the voltage matrix were created for spheres of various radii by implementing the equations of the previous chapter in a computer code written for Matlab 5. The computer code was executed on a Sun Microsystems Sparc 20 workstation running the Solaris 2.6 operating system. A function is called by the main program to generate the body of revolution and compute an array of \hat{t} and $\hat{\phi}$ current density expansion coefficients given input parameters of sphere radius, maximum sub/entire-domain mode, fourier mode range, backscatter angle, and specification of sub- or entire-domain method. The far-field scattering cross-section is also computed. The source-code is included in Appendix A of this document and can be easily modified for other geometries and basis functions.

In this chapter, computed results are presented for the scattering from spheres ranging in electrical size from $ka = 1$ to $ka = 7^1$. The scattering is calculated for subdomain current expansions using pulse functions and entire-domain current expansions using Chebyshev polynomials of the first kind. Galerkin testing is used in both cases. The data shows that the entire-domain expansions converge more accurately and in fewer modes than the subdomain expansions. A comparison showing the potential computation time savings of the entire-domain method over the subdomain method is also presented. It was found that phase approximations used in the discretization and numerical solution limit the accuracy of the computed scattering for spheres of small electrical size. Recommendations for improving the computations are given.

¹ $k = 2\pi/\lambda$ and a = sphere radius.

5.1 The Computer Code

The main routine of the computer code, MAINSPHERE, is written in modular fashion for clarity. The subroutines MAKET, MAKEZV, COMPRCS, MAKELIMITS, and PLOT RCS are written separately only for readability. MAINSPHERE initiates all variables and calls the subroutines. MAKET creates a 25×25 matrix of the polynomial coefficients of the Chebyshev polynomial of the first kind to be used as an entire-domain basis. MAKEZV computes the impedance matrix, the voltage matrix, and the measurement matrix. The current coefficients are determined by computing the inverse of the impedance matrix and performing a matrix multiplication. COMPRCS computes the far-field scattering cross-section which is plotted by PLOT RCS. MAKELIMITS creates an array of integration limits used if the subdomain method is chosen. A flowchart of the code is shown in Figures 5.1 through 5.3.

The integrands of Equations (4.16) through (4.19) for $[Z^{tt}]_{ij}$, $[Z^{t\phi}]_{ij}$, $[Z^{\phi t}]_{ij}$, and $[Z^{\phi\phi}]_{ij}$ of the impedance matrix are written as functions of their variables, t , t' , and ϕ' . These functions are ZTTARG2, ZTPARG2, ZPTARG2, and ZPPARG2, respectively. Integration is performed by the functions similarly named (without the suffix ARG, i.e., ZTT2, etc.) which call GQUAD3D to create a three-dimensional array of integration points according to a Gaussian quadrature rule and evaluate the integrands at those points. Matlab allows a "simultaneous" function evaluation (2-3 sec total CPU time for a Z integral evaluation) of all points in the array using built-in matrix operations. An early draft of the code attempted to evaluate the integrand by stepping through each point separately. This took the same CPU time per integration point and was prohibitive. Mautz [8] used 20 integration points for the ϕ' integration and a four-delta amplitude approximation per subdomain segment with satisfactory results. Since MAINSPHERE is used to compute the solution using either subdomain or entire-domain basis functions, Gaussian quadrature is used to integrate with respect to t and t' as well as ϕ' . Using 20 integration points for all three variables produced integral convergence to at least eight significant digits. Convergence to more than ten significant digits was obtained using 30 integration points. Since computation time was comparable, 30 integration points for each variable is used

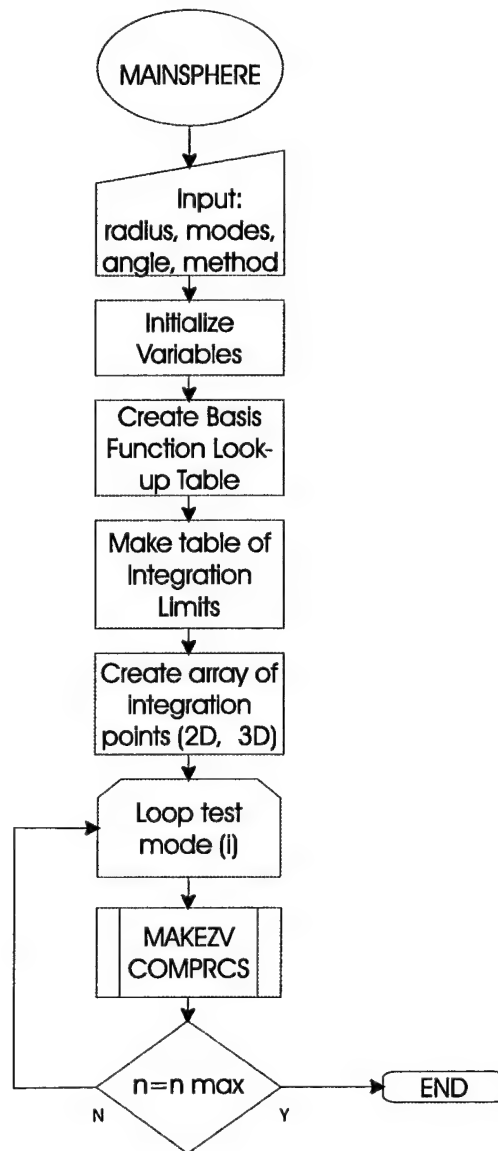


Figure 5.1 Flowchart of MAINSPHERE

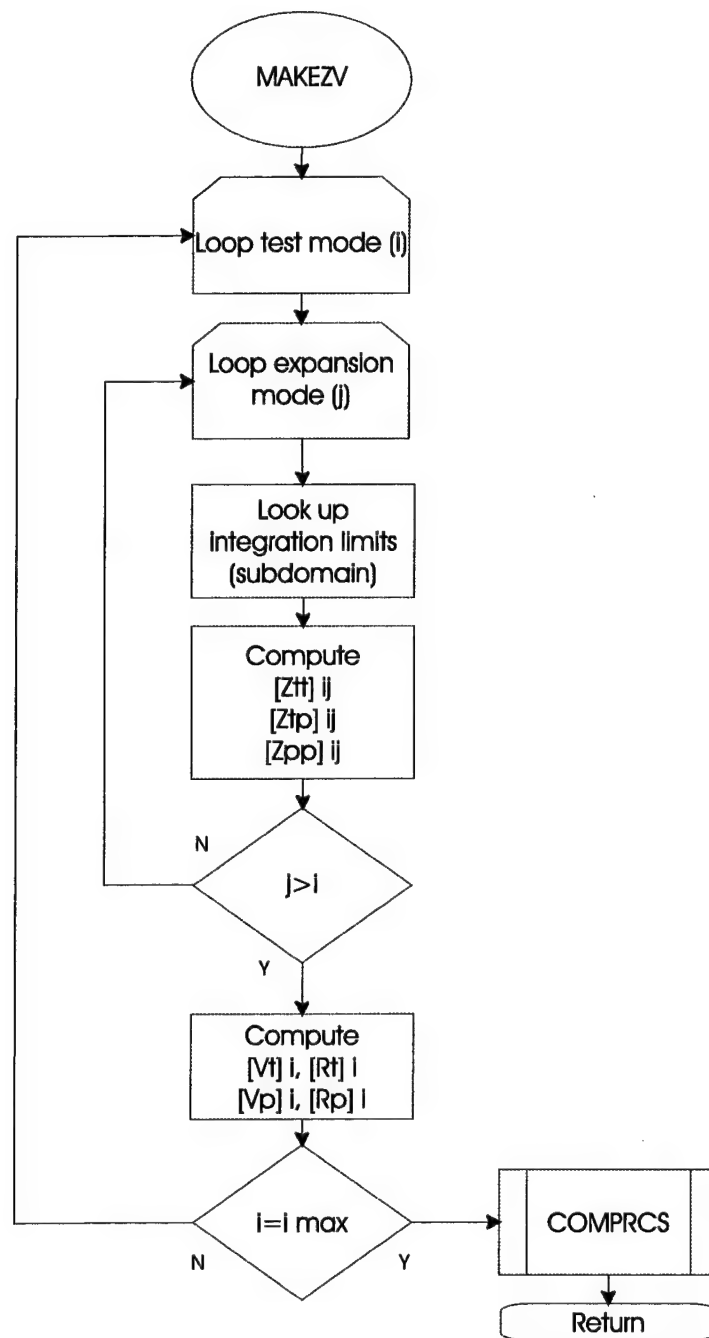


Figure 5.2 Flowchart of MAKEZV

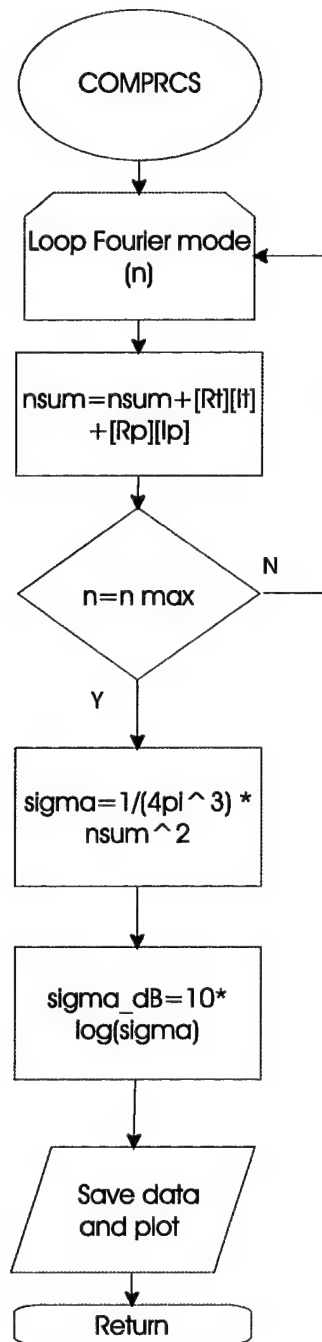


Figure 5.3 Flowchart of COMPRCS

for all results presented here. The symmetries expressed in Equation (4.24) are exploited thereby cutting computation time roughly in half.

The integrands of equations for $[V_i^t]$ and $[V_i^\phi]$ are similarly written as functions of their variables, t and ϕ . Integration is performed by a two-dimensional, 30 point Gaussian quadrature method. The measurement vectors, $[R_i^t]$ and $[R_i^\phi]$ are produced by integrating $[V_i^t]$ and $[V_i^\phi]$ with the Fourier mode index negated, $-n$.

The function GEO returns the parameters *rho*, *zee*, and *vee* which define the body of revolution generating arc as a function of arclength, t or t' as appropriate. The parameters *rho* and *zee* represent the lengths of the $\rho(t)$ and $z(t)$ components of a vector from the origin to a point on the generating arc defined by t as shown in Figure 3.1. The parameter *vee* represents the angle between the rotational axis, \hat{z} , and the tangent vector to the generating arc at t , pointing in the direction of increasing t . The sign of *vee* is defined and used as a positive number if the tangent at t points away from \hat{z} and a negative number if the tangent at t points toward \hat{z} . The parameters that define a sphere in positive z are,

$$\begin{aligned}\rho &= a \sin(t/a) \\ z &= -a \cos(t/a) + a \\ v &= \sin^{-1} \left(\frac{\Delta \rho}{\sqrt{\Delta \rho^2 + \Delta z^2}} \right),\end{aligned}\tag{5.1}$$

where a is the radius and $\Delta \rho$ and Δz are increments in ρ and z due to an infinitesimally small increase in the arclength, t , at the point on the generating arc specified by a given t .

The function BASIS takes a mode and an arclength as inputs and returns the value of the requested basis function mode at that arclength. This is done via a mapping of the arclength domain in t' to the Chebyshev basis function domain of $-1 \leq s \leq +1$. For impedance integral calculation, the functions DERIVTP and DBASIS are used to compute the value of the derivative of the quantity $\rho' f_j(t')$. The companion functions TEST, DERIVT, and DTEST compute similar quantities with respect to the testing functions. Since Galerkin testing is used, these routines are exactly the same as the basis function routines and can be combined. The code was written to call them separately, however, for readability and demonstration purposes.

5.2 The Currents

The subroutine MAKEZV fills the $[Z]$ matrix and the $[V]$ matrix. The current density expansion coefficients I_i from Equation (4.15) are determined by the inverse impedance matrix, $[I] = [Z]^{-1} [V]$, where $[I]$ is the transpose of $[I^t I^\phi]$. The elements of both $[I^t]$ and $[I^\phi]$ are the coefficients of the corresponding terms in the current expansions in the t and ϕ directions for a given Fourier mode, n . The total currents are determined by (using function and variable names from the computer code), for each n ,

$$\begin{aligned}\bar{J}_n^{t'} &= \hat{t}' \sum_{j=0}^{edmax} I_t(j) * basis(j, t') \\ \bar{J}_n^{\phi'} &= \hat{\phi}' \sum_{j=0}^{edmax} I_\phi(j) * basis(j, \phi'),\end{aligned}\tag{5.2}$$

where t' is a vector of samples across the arclength, $0 \leq t' \leq tmax$. $Edmax$ is the maximum number of entire-domain modes used. Adding across all n gives,

$$\bar{J}^{t'} = \hat{t}' \sum_{n=0}^{fmax} J_n^{t'} * exp(j * n * \phi'),\tag{5.3}$$

where $fmax$ is the maximum number of Fourier modes. It is convenient to evaluate the currents along the $\phi' = 0$ longitude (in the XZ -plane), because the exponential becomes unity. Figure 5.4 shows the $\hat{\phi}$ directed current densities represented by each entire-domain mode for a sphere of $ka = 4.0$ excited by a $\hat{\phi}$ directed incident electric field when $n = 2$ evaluated at broadside ($\theta = \pi/2$). There is a similar set of currents for every Fourier mode used in the current expansion. The top two subplots show the contribution to the current density of each of the T_0 – T_5 entire-domain modes. The modes are recognizable as the function of Figure 3.3 scaled by the corresponding element of $[I^t]$. The scaling for some modes is very small or zero, minimizing their effect on the overall current. Only the modes that serve to accurately represent the functionality of the actual current density as described by the integral equation are selected by the method. The bottom subplot of Figure 5.4 shows the sum of each entire-domain mode above. The solid line here represents the current density magnitude for the $n = 2$ Fourier mode. The total current density is the

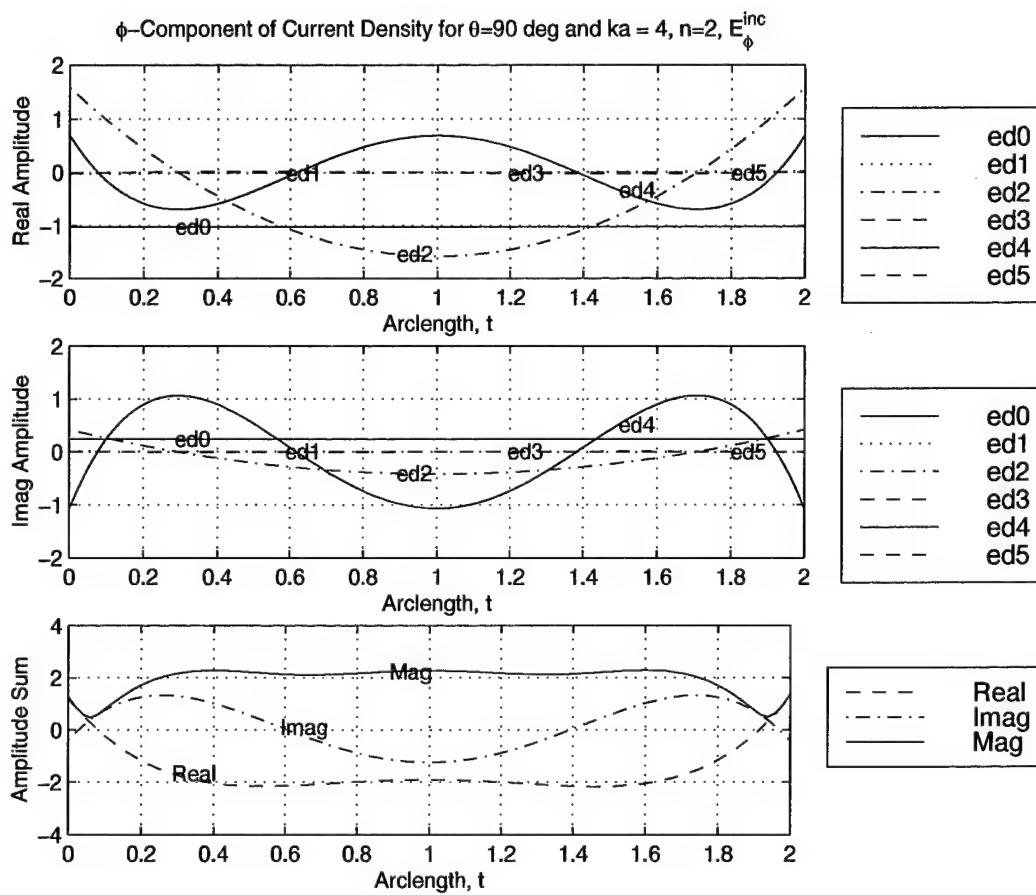


Figure 5.4 $\hat{\phi}$ directed current density for the $n = 2$ entire-domain modes for $ka = 4.0$

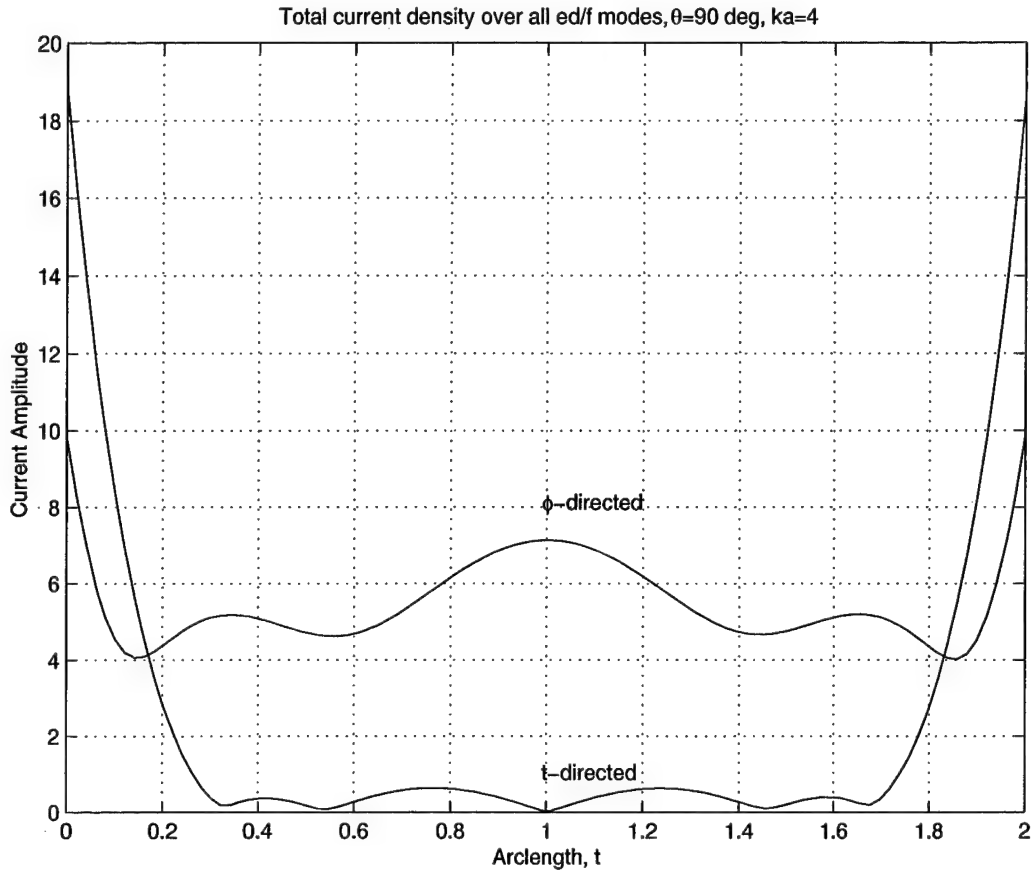


Figure 5.5 Total \hat{t} and $\hat{\phi}$ directed current densities ($n = 0-5$) for $ka = 4.0$ illuminated by E_{ϕ}^{inc} at $\theta = 90^\circ$

sum of all entire-domain contributions for all Fourier modes. The total $\hat{\phi}$ directed current density for a sphere of $ka = 4.0$ evaluated at broadside ($\theta = \pi/2$) is shown in Figure 5.5. A sphere of radius $a = 4.0/k$ has a circumference of four wavelengths. The current density around the sphere exhibits more oscillations than does a sphere of smaller radius. Consider the smoother total current density for a sphere of radius $a = 3.1/k$ as shown in Figure 5.6. The circumference is now approximately three wavelengths. More Fourier series expansion terms of higher oscillation orders, $e^{jn\phi'}$, are required to accurately describe the current density for spheres of larger electrical size.

The $\hat{\phi}$ directed current density coefficients for each entire-domain mode are plotted in Figure 5.7 for sphere sizes of $ka = 0.9$, $ka = 2.1$, and $ka = 4.0$. The coefficients are grouped by Fourier mode in sequential order of $I_{nj} = I_{n0}$ through I_{n10} . The vertical axis of

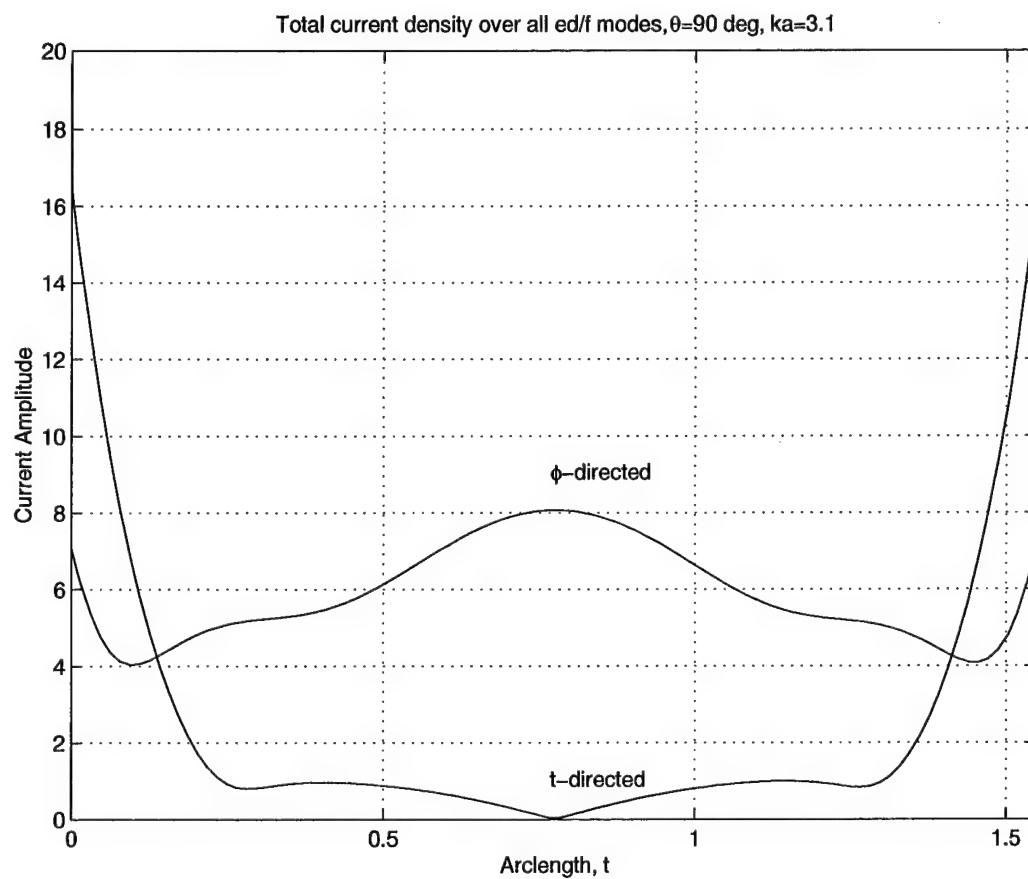


Figure 5.6 Total $\hat{\phi}$ directed current density ($n = 0-5$) for $ka = 3.1$ illuminated by E_{ϕ}^{inc} at $\theta = 90^{\circ}$

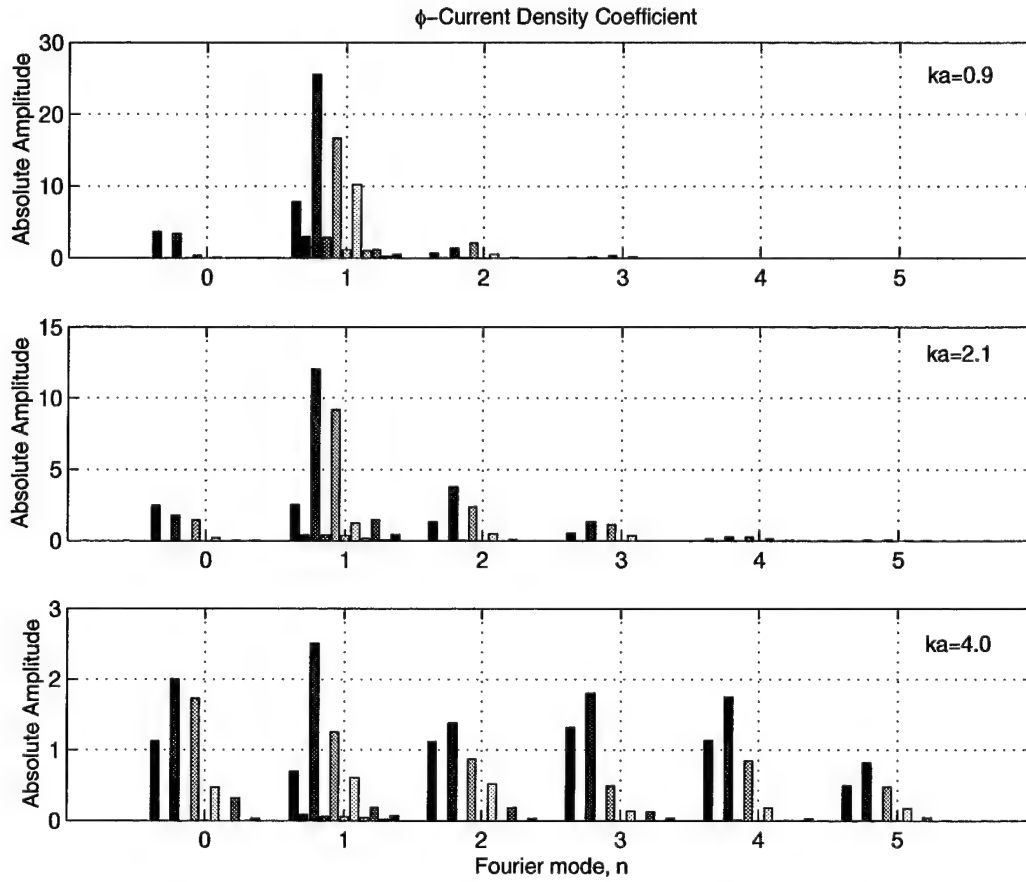


Figure 5.7 $\hat{\phi}$ directed current density coefficients for the T_0 - T_{10} entire-domain modes, grouped by Fourier mode

each plot is scaled to show the appropriate detail for each sphere size. It is easily seen that as the sphere size increases, more Fourier modes are required to capture the total *energy* of the current density. In other words, more Fourier modes must be considered before the current density coefficients decrease sufficiently in amplitude. Also, for a given Fourier mode, it is obvious that most of the energy is captured in the T_0 through T_5 entire-domain modes.

Figure 5.8 shows the \hat{t} directed current densities represented by each entire-domain mode for a sphere of $ka = 4.0$, $n = 2$ when excited at broadside ($\theta = \pi/2$) by a $\hat{\phi}$ polarized incident electric field. There is a similar set of currents for every Fourier mode used in the current expansion. Note that as in the $\hat{\phi}$ directed current, some entire-domain modes are emphasized while others are minimized. As before, this serves to represent the actual

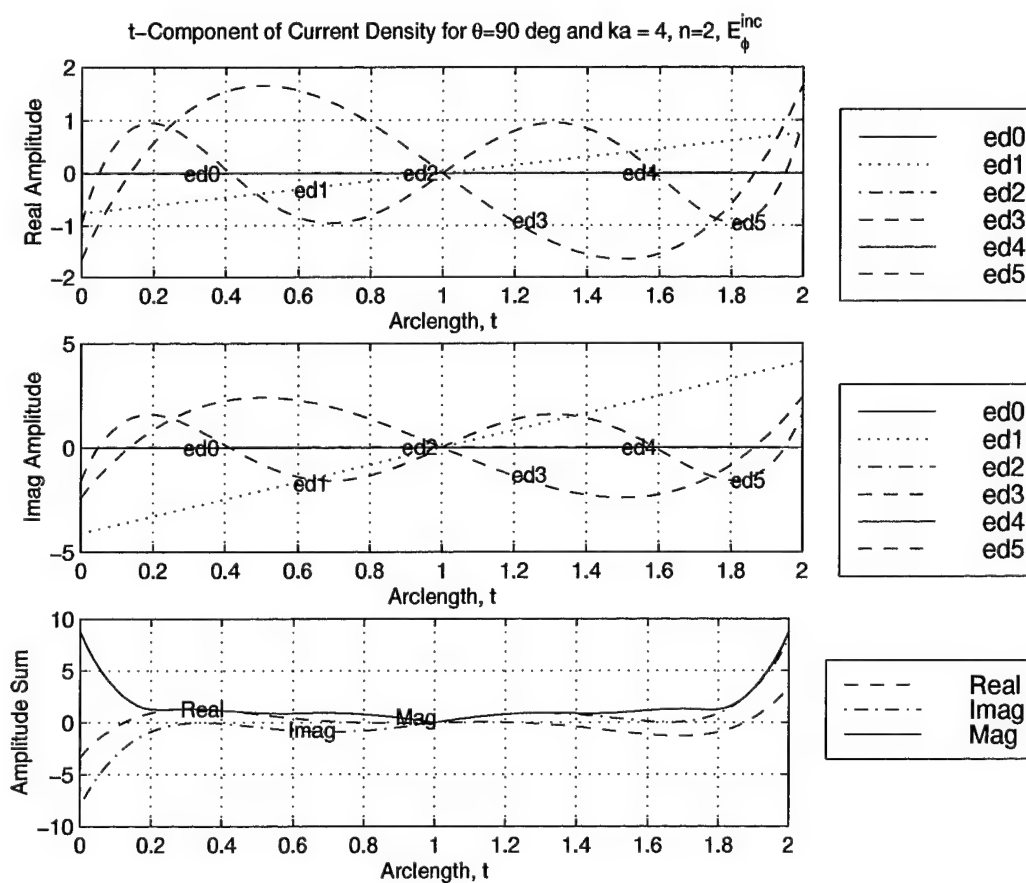


Figure 5.8 \hat{t} directed current density for the $n = 2$ entire-domain modes for $ka = 4.0$

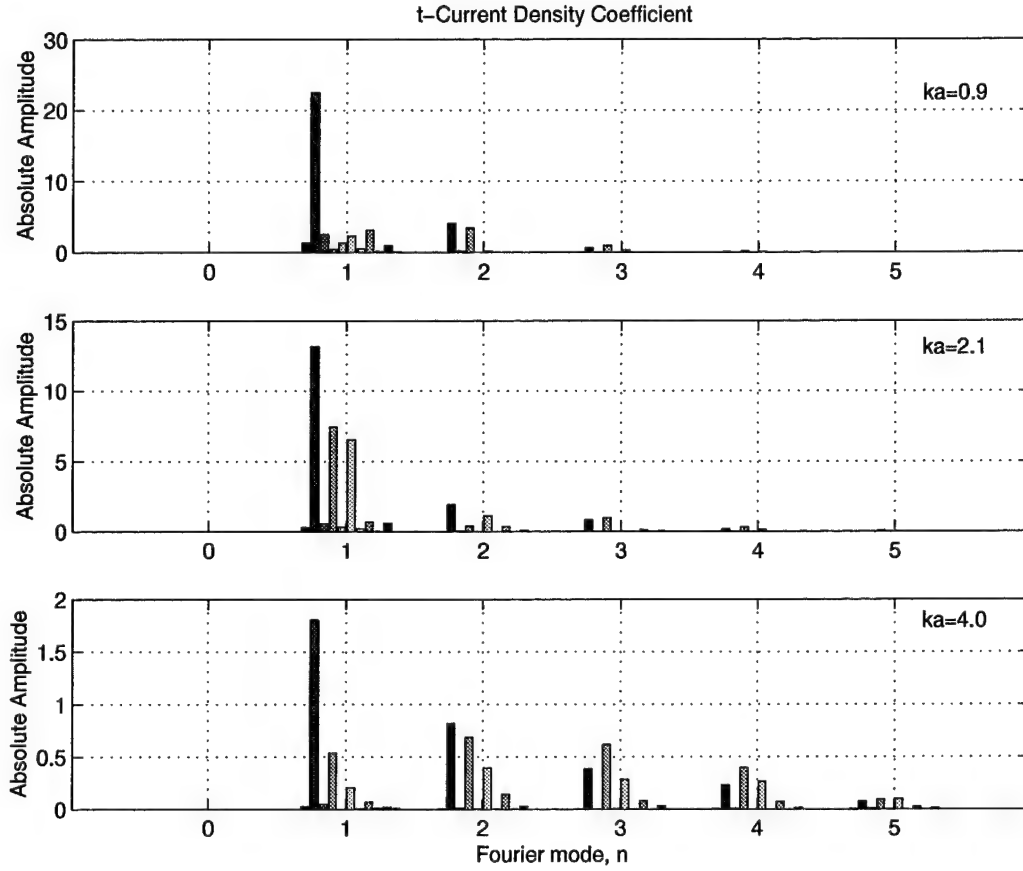


Figure 5.9 \hat{t} directed current density coefficients for the T_0 – T_{10} entire-domain modes, grouped by Fourier mode

current density functionality in this direction. The sum of the entire-domain modes is represented in the bottom plot of Figure 5.8 where the functionality is seen to be near zero across most of the arclength. The total \hat{t} directed current density for the sphere of $ka = 4.0$ evaluated at broadside ($\theta = \pi/2$) is shown in Figure 5.5. The \hat{t} directed current density coefficients for each entire-domain mode are plotted in Figure 5.9 for sphere sizes of $ka = 0.9$, $ka = 2.1$, and $ka = 4.0$. The trends are similar to those of the $\hat{\phi}$ directed current density coefficients. The current densities for all modes of the $ka = 4.0$ sphere in both the \hat{t} and $\hat{\phi}$ directions are given in Appendix B.

Wood's subdomain analysis of the current density excited on the surface of a spherical cavity finds that, with the exception of the $n = 1$ Fourier mode, both the \hat{t} and $\hat{\phi}$ current density vanishes at the poles [16]. The amplitude coefficient for each term in the current

density expansion is determined by the Moment Method computation based on the *need* for the frequency content that term offers. Emphasis of a particular term is based on a weighted average over the domain of the portion of the generating arc to which the term applies. In a subdomain method, the coefficient for the function which represents the current density amplitude at the poles can be zero without respect to any other segment of the generating arc. In an entire-domain method, the domain of each mode is the entire length of the generating arc, and the amplitude coefficient of each mode is the best choice across the domain of the arc. In choosing Chebyshev expansion functions, there is a potential disadvantage in that each mode has a positive or negative finite amplitude at both ends. The only way for the current to vanish at the poles is by cumulative addition of many modes scaled by their coefficients. This is not a disadvantage of using entire-domain basis functions, but rather, an indication that another entire-domain family of functions may be more appropriate for this specific geometry. Given enough Chebyshev modes, however, it is expected that the current would approach the anticipated value across the entire domain of the sphere, including at the poles. Because of the decreased amplitude of the higher order modes, many more may be required than that necessary for determining the current density at points away from the poles. Had the fact that the current should vanish at the poles been considered at the beginning of this research, a Fourier expansion (exponential basis functions) may have been chosen for the expansion of the current density along the arclength as well as in ϕ . This would have allowed a build-up of the needed frequency content satisfied by the lower order modes without adversely affecting the current density at the poles.

When the sphere is excited by a plane wave incident at an angle other than broadside, the poles shift and are no longer at the ends of the generating arc. A corresponding shift in the current density distribution along the arclength is expected. Figure 5.10 shows the accumulation of current density for $ka = 4.0$ and E_{ϕ}^{inc} incident at $\theta = \pi/3$. Each entire-domain mode for the $n = 2$ Fourier mode of the $\hat{\phi}$ component of current density is plotted in the top two subplots. A different weighting of the entire-domain modes is seen when compared to the broadside case of Figure 5.4. This weighting serves to enhance the current density on the generating arc near the $\theta = \pi/3$ region and contains

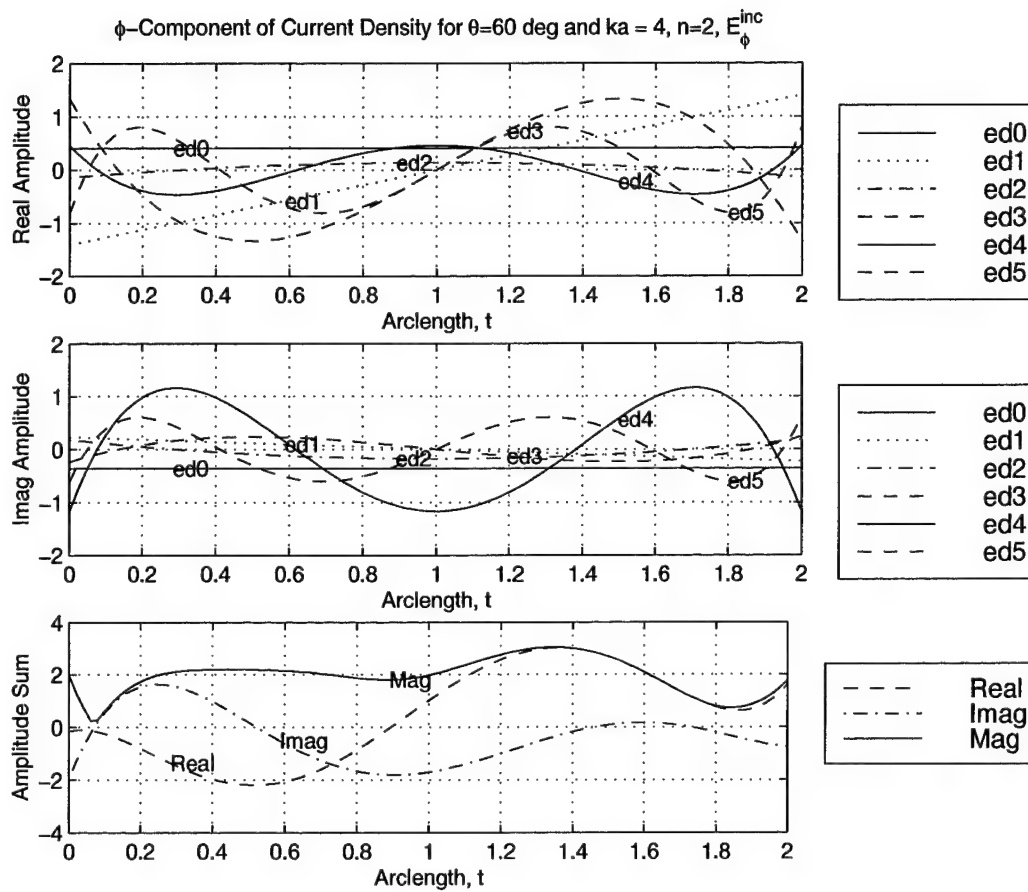


Figure 5.10 $\hat{\phi}$ directed current density for the $n = 2$ entire-domain modes for $ka = 4.0$ illuminated by E_ϕ^{inc} at $\theta = 60^\circ$

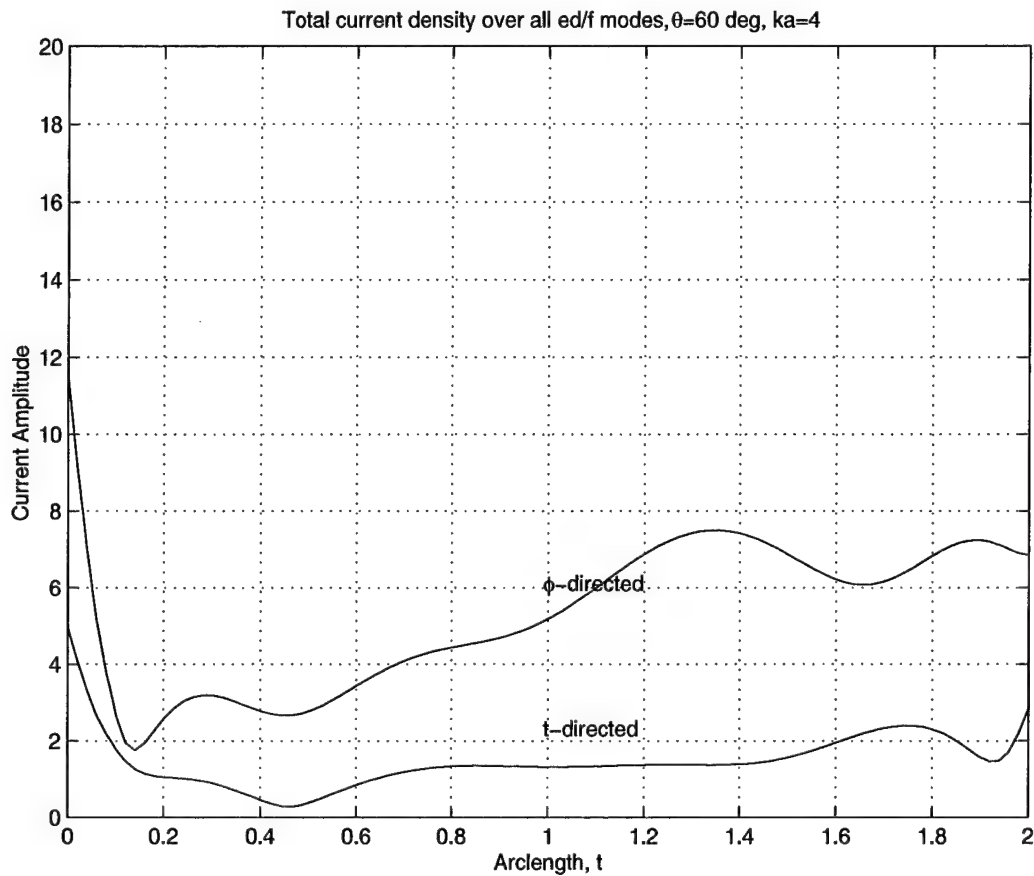


Figure 5.11 Total \hat{t} and $\hat{\phi}$ directed current densities ($n = 0-5$) for $ka = 4.0$ illuminated by E_{ϕ}^{inc} at $\theta = 60^\circ$

the appropriate frequency content for this excitation. Note that there is still a rise in the current density near the ends of the arclength due to the finite sum of the Chebyshev functions. The cumulative total over all entire-domain and Fourier modes (5 modes in each case) is plotted in Figure 5.11. The expected shift in the pattern is seen with a peak at $t = 1.33$ corresponding to the illumination angle, θ .

5.3 The Scattering Cross-Section

5.3.1 Assessment of Accuracy. The solution to the integral equations given in Chapter IV is the vector $[I]$ which contains the coefficients to the expansion of the current density, \bar{J} . The accuracy of the solution, therefore, is best measured by comparison to known currents. Production codes (subdomain basis) such as CICERO and JRMBOR that

are currently in use calculate the current internally and output only the electromagnetic field components or the scattering cross-section as the quantity of interest. Although the currents computed in these codes are also an approximation limited by the smallness of the subdomain discretization used, they would serve as a useful check of what is obtained here. Without modification to the codes themselves, however, the currents are not available to the user. Mautz [9] assesses accuracy by defining a metric that relates the currents resulting from his magnetic- and electric-field integral equations to his combined-field integral equation (a linear combination of the two). His purpose is to show a deviation from an assumed norm of stray data points resulting from physical resonances of the body. This is suitable for showing how well the combined-field integral equation discriminates against the resonances.

Accuracy in the computation of the current is paramount to obtaining an accurate scattering cross-section. The averaging effect of the scattering cross-section calculation, however, allows for some variation in current quantities without largely affecting the scattering cross-section itself. It will here suffice to use the far-field scattering cross-section as the figure of merit and compare that computed by MAINSPHERE using both subdomain and entire-domain expansions of the current density to that produced by the Mie series [5] which is an exact solution.

5.3.2 Subdomain Data. The code MAINSPHERE and its supporting subroutines and functions listed in Appendix A were used to compute the scattering cross-section of a perfectly electrically conducting sphere of electrical size ranging from $ka = 0.5$ to $ka = 5.0$. Approximately 30 data points were computed in this range. For this formulation, the surface current density was expanded in the \hat{t}' and $\hat{\phi}'$ directions using unit amplitude pulses as basis functions. The current was expanded additionally by a common Fourier series exponential in ϕ . MAINSPHERE was run in the subdomain ('sd') mode. The resulting quantities are normalized with respect to electrical size and wavelength so as to oscillate about a constant value. Comparison is made to the exact normalized scattering cross-section calculated by means of the Mie series given by Harrington [5].

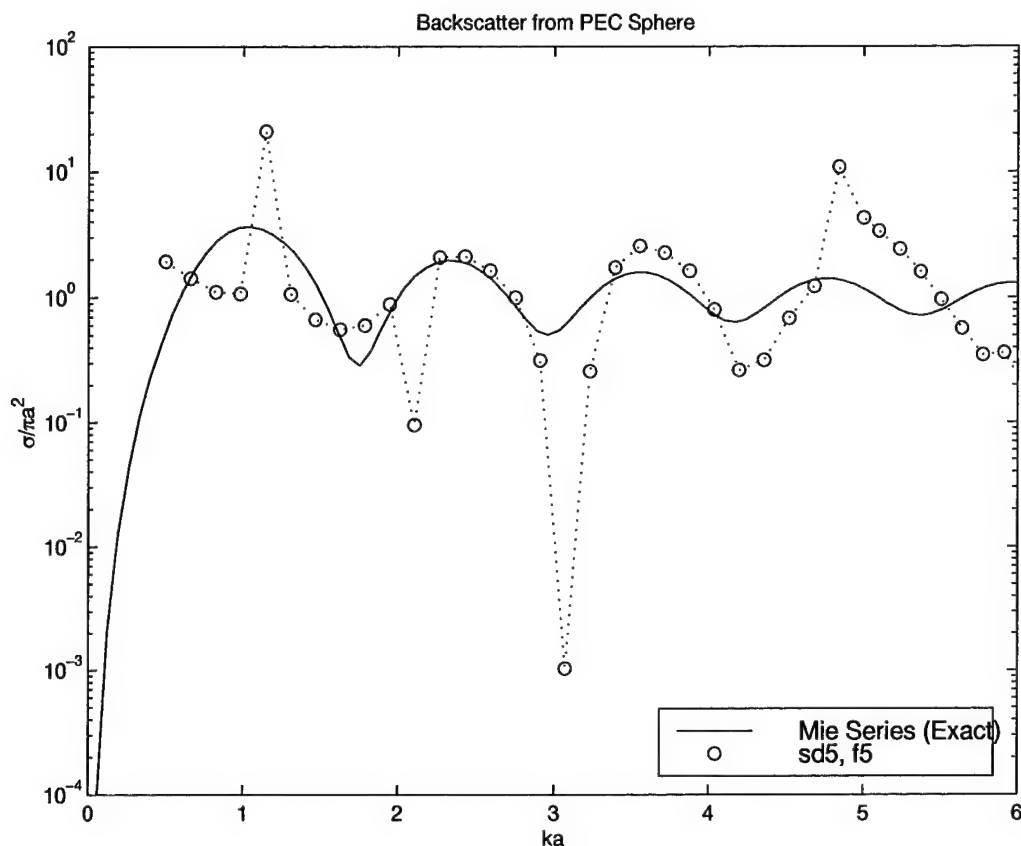


Figure 5.12 Backscatter from a PEC sphere using 5 subdomain segments, illuminated at $\theta = 90^\circ$ by E_ϕ^{inc} .

The first data set shows the scattering cross-section computed with five subdomain segments on the generating arc for the selected range of electrical sizes. Five Fourier modes were used in the ϕ expansion for this and all other data presented. The data points are shown in Figure 5.12 as discrete points (circles). The data points are connected by a dotted line to make the sequence more apparent where neighboring points follow the same pattern. The line is not, however, intended to indicate an accurate interpolation between points. An occasional stray point gives the impression that addition of another point near it would result in nearly the same magnitude, but this is not necessarily the case. Although data points in the $ka = 2.25$ to $ka = 2.75$ region approach the exact solution and points in the $ka = 3.5$ to $ka = 4.0$ approach the exact solution to a lesser degree, the data overall is somewhat erratic. It is clearly obvious that five subdomain segments are insufficient to accurately represent scattering cross section. A large number of data points differ by

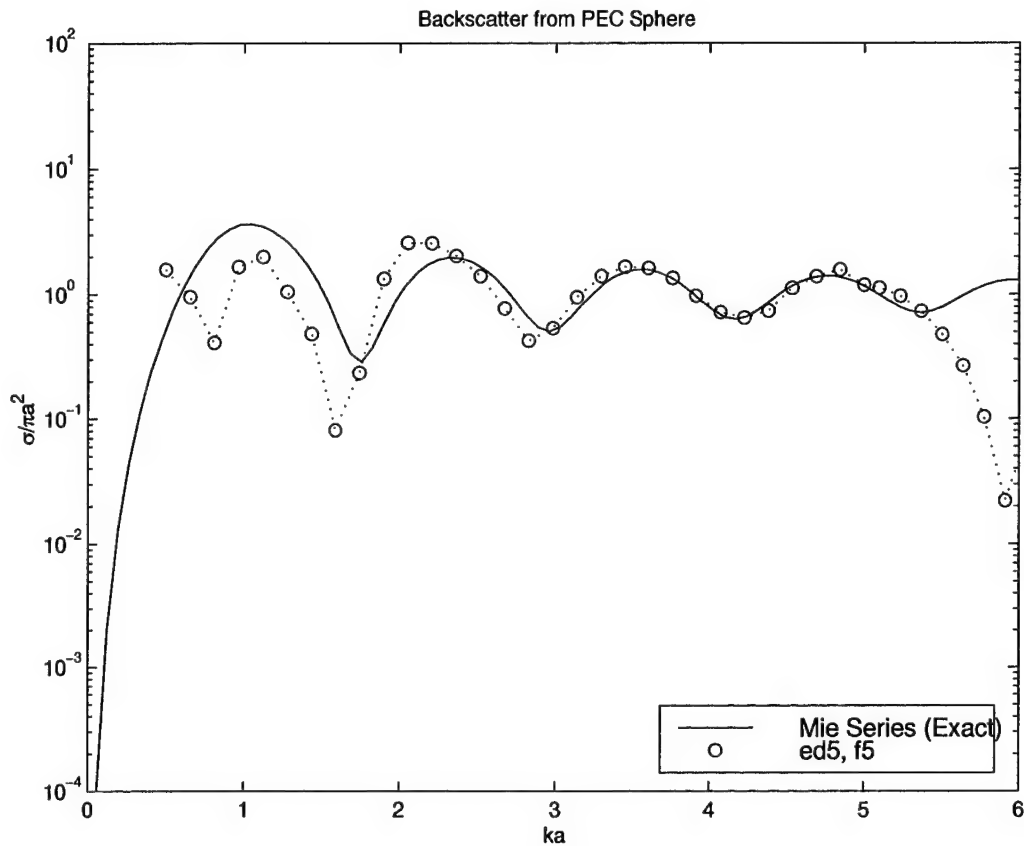


Figure 5.13 Backscatter from a PEC sphere using 5 entire-domain modes, illuminated at $\theta = 90^\circ$ by E_ϕ^{inc} .

± 3 –10dB. The largest deviation is a cross-section of 0.001 at $ka = 3.1$ which differs from the Mie series by -27dB. Mautz shows that at least fifteen subdomain sections are required to model the current density with accuracy sufficient to match the Mie series [9].

5.3.3 Entire-Domain Data. The next data set shows the scattering cross-section computed with five entire-domain modes on the generating arc for the selected range of electrical sizes. The data points are shown as circles connected by a dotted line in Figure 5.13. It is readily apparent that five entire-domain modes result in a much closer conformity to the Mie series than do an equivalent number of subdomain segments. The entire-domain basis functions are better able to accurately represent the smoothness and functionality of the surface current density. The data points in the $ka = 3.0$ to $ka = 5.5$ region closely follow the Mie series curve with less than 0.5dB error. The region from

$ka = 1.75$ to $ka = 3.0$ exhibits an error of 2dB to 3dB. Electrical sizes smaller than $ka = 1.75$ differ by an almost constant -4dB.

At larger electrical sizes ($ka \geq 5.5$) the data begins to fall away from the Mie series curve. This is due to the fact that as the sphere gets larger, the current around the surface becomes more varied and, as a result, requires more and more Fourier expansion modes (higher values of n) to accurately represent the current oscillations (see Figure 5.7). The current density at smaller electrical sizes is more constant around the sphere circumference, and is adequately covered by a few Fourier modes (2 or 3 for $ka \leq 2$) [9].

The inaccuracy in normalized cross-section seen in this data for smaller ka is introduced by an approximation made in the integrands of MAINSPHERE to allow integration through the singularity which occurs when the difference between the radial distance between the far-field observation point and the testing/basis functions, R in the equations, goes to zero. In subdomain methods, the only time this occurs is when the testing function coincides with the basis function. When entire-domain basis functions are used, the domain of every mode coincides with every other. The value of R is zero when t equals t' and ϕ' equals zero. It is also zero at any value of ϕ' when t and t' are both at their minimum or maximum value. This behavior of R is shown in Figure 5.14. The radial projection in the XY -plane of the vector to a point on the generating arc, ρ , also goes to zero at the ends of the generating arc causing a singular behavior in the impedance matrix integrands. The effect of the ρ related singularity is lessened by the fact that the Gaussian quadrature integration does not involve a function evaluation of the integrand exactly at the endpoints. Also, the higher density of integration points at the ends of the integration domain allow a more accurate integration in those regions. To keep R from going to zero in the integrations, an incremental distance, *skosh*, is added to R . This method is called the method of equivalent separation and has been used in scattering problems [9]. The distance R is kept slightly above zero allowing integration without extraction and separate handling of the singularity. However, since R represents a path of phase accumulation, a phase error is introduced into the integrands. The smaller the sphere gets in electrical size, the larger this phase error gets relative to the sphere size. It was found that using this equivalent separation for spheres of $ka \leq 2$, the integrals converge to an approximate

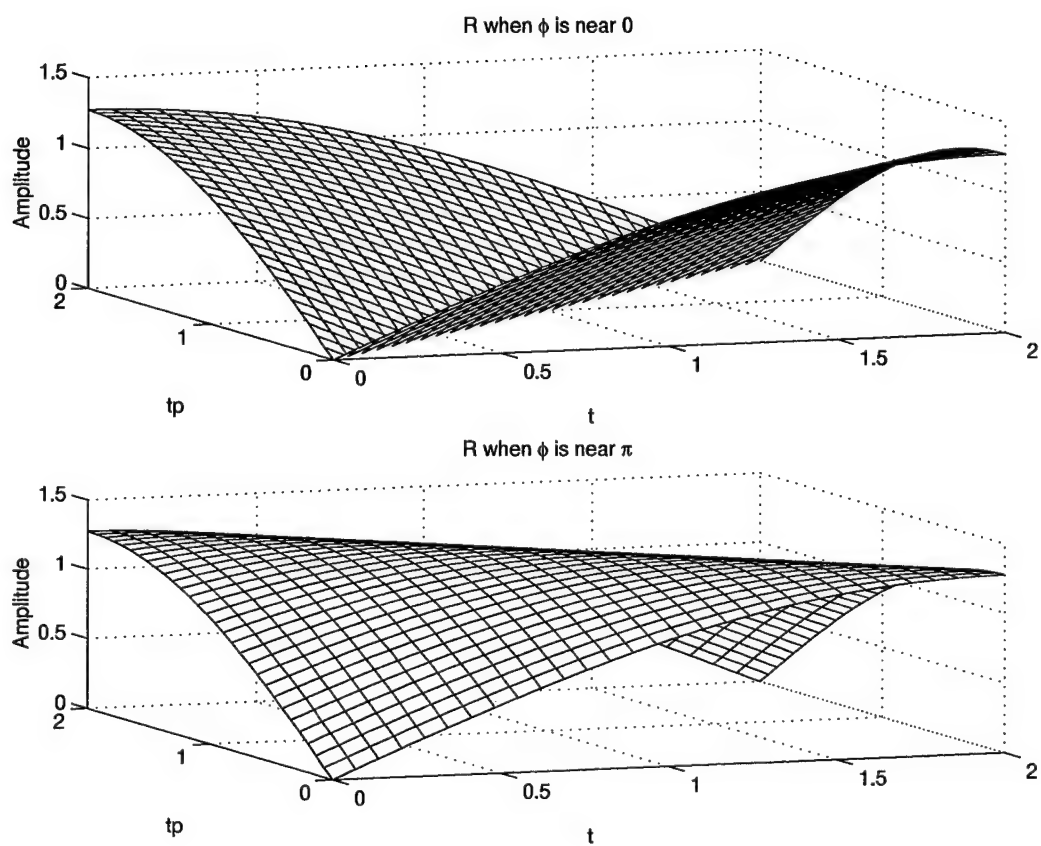


Figure 5.14 Value of R as a function of t , t' , and ϕ' .

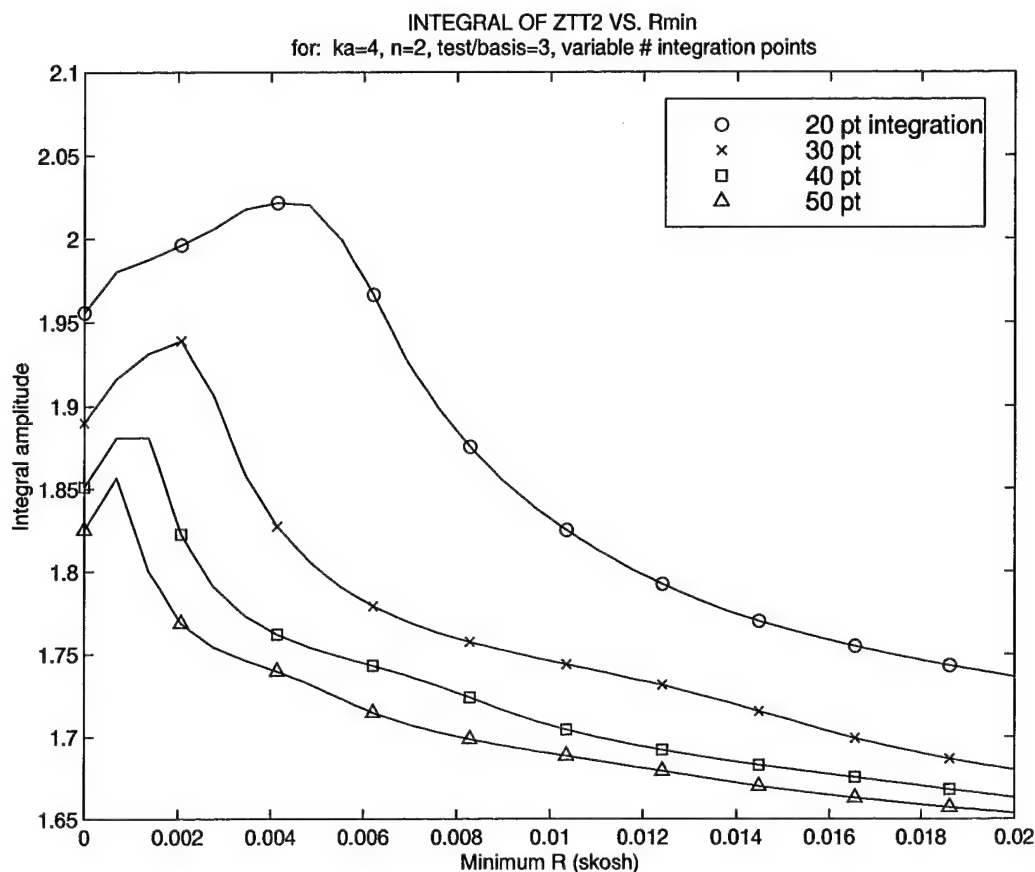


Figure 5.15 The integral of Z^{tt} as a function of minimum R for various orders of Gaussian quadrature integration.

solution, but not to the Mie series curve. Re-computing with additional entire-domain or Fourier modes did not improve the results in this region. Reducing the minimum phase distance, *skosh*, brought the cross-section points slightly closer to the Mie series curve, but did not solve the problem. Also, increasing the order of Gaussian quadrature quickly became computation time inhibitive. Figure 5.15 is a plot of the integrated amplitude of Z^{tt} versus minimum phase distance for a sphere of $ka = 4.0$, the $n = 2$ Fourier mode, and the T_3 testing and basis modes. Data is plotted for 20, 30, 40, and 50 point Gaussian quadrature integration. As the Gaussian quadrature order is increased, there is less variation in number given by the integration. This is seen by the curves getting closer together as the order is increased. As the minimum R is varies, the integration yields a result that does not converge. A similar behavior is also seen when the testing function and basis function

are not the same although, in general, the variation is less pronounced. It is concluded that accuracy is only improved by a more rigorous handling of the singularity by means of singularity extraction and separate evaluation of the integrals in the region surrounding the singularity.

5.4 Computation and Matrix Fill Time

It is seen that increasing the number of modes used to compute the system of matrices results in a more accurate solution for the unknown current and, therefore, a more exact calculation of scattering cross-section. A major advantage of using entire-domain basis functions to expand the current density is that additional modes can be added by superposition without complete re-computation of each matrix element. The integration limits on the inner product for the entire-domain method remain the same for every combination of testing and expansion mode, i and j . In other words, each mode has as its domain, the entire length of the generating arc. Higher order modes are simply added *in parallel* to lower order modes. This is not true for subdomain basis functions. The integration limits on the inner product for the subdomain method correspond to the length of each segment. Each segmental subdomain *mode* adds to the others *in series*. In order to increase the number of segments in the subdomain discretization, the length of every segment must change. This requires complete re-computation of all matrices. As a result, increasing the order of the discretization to improve the accuracy of the solution wastes all computation time up to that point. A comparison of matrix fill times and computation times for the entire-domain method and the subdomain method is shown below.

Elapsed computer processor time was tracked through all trials for the following computations: $[Z_{ij}^{tt}]$, $[Z_{ij}^{t\phi}]$, $[Z_{ij}^{\phi\phi}]$, $[V^t]$, $[V^p]$, and $[Z]$ inversion. The time to add an additional mode was also tracked. These times are shown in Table 5.1. The majority of the total computation time is in the evaluation of the integrals to determine the elements of the impedance matrix, $[Z]$. Processor time averages 3.0 seconds per integration. Slightly more than half of the elements of $[Z]$ must be computed to fill $[Z]$ because of symmetries. Because the fill time for $[Z]$ dominates, proper choice of basis function (entire-domain vs. subdomain and actual function) offers an important advantage.

Element	Time
$[Z_{ij}^{tt}]$	3.5 sec
$[Z_{ij}^{t\phi}]$	3.0 sec
$[Z_{ij}^{\phi\phi}]$	2.5 sec
$[V^t]$	0.5 sec
$[V^p]$	0.5 sec
$[Z]^{-1}$	0.5 sec

Table 5.1 Average integration times

Based on the computation time observations, the additional time required to add a mode to the impedance matrix given an initial number of modes is determined and is shown in Tables 5.2 and 5.3.

Consider an example of overall computation time to fill $[Z]$. Starting with an initial choice of five entire-domain expansion modes, 2.75 minutes (165 seconds) are required to compute the $N(2N + 1) = 55$ symmetric elements of $[Z]$. Suppose that after determining the current and checking it against a specified tolerance, more modes are added. This is repeated until ten modes are used to achieve an accurate solution. Every time a mode is added, a new row is added to $[Z^{tt}]$ and $[Z^{\phi\phi}]$ and a row and a column are added to $[Z^{t\phi}]$ as shown in Equation (5.4) for a total of $4N + 3$ new computations, where N is the initial number of modes. The x 's represent elements of previously calculated modes, o 's represent new elements that must be computed, and \bullet 's represent new elements filled by symmetry.

$$[Z] = \left[\begin{array}{c} \left[\begin{array}{cccc} x & x & x & \bullet \\ x & x & x & \bullet \\ x & x & x & \bullet \\ o & o & o & o \end{array} \right] \\ \left[\begin{array}{cccc} x & x & x & \bullet \\ x & x & x & \bullet \\ x & x & x & \bullet \\ \bullet & \bullet & \bullet & \bullet \end{array} \right] \end{array} \right] \left[\begin{array}{c} \left[\begin{array}{cccc} x & x & x & o \\ x & x & x & o \\ x & x & x & o \\ o & o & o & o \end{array} \right] \\ \left[\begin{array}{cccc} x & x & x & \bullet \\ x & x & x & \bullet \\ x & x & x & \bullet \\ o & o & o & o \end{array} \right] \end{array} \right] \quad (5.4)$$

This additional computation time is added to the initial matrix fill time to get the overall computation time. Doubling the number of entire-domain modes to ten adds 7.75 minutes

Initial modes	Elements to fill	Fill time	ENTIRE-DOMAIN			Computation overhead
			Elements req'd to add mode	Add time	Total CPU time	
1	3	9	7	21	30	0
2	10	30	11	33	63	0
3	21	63	15	45	108	0
4	36	108	19	57	165	0
5	55	165	23	69	234	0
6	78	234	27	81	315	0
7	105	315	31	93	408	0
8	136	408	35	105	513	0
9	171	513	39	117	630	0
10	210	630	43	129	759	0
11	253	759	47	141	900	0
12	300	900	51	153	1053	0
13	351	1053	55	165	1218	0
14	406	1218	59	177	1395	0
15	465	1395	63	189	1584	0
16	528	1584	67	201	1785	0
17	595	1785	71	213	1998	0
18	666	1998	75	225	2223	0
19	741	2223	79	237	2460	0
20	820	2460	83	249	2709	0
21	903	2709	87	261	2970	0
22	990	2970	91	273	3243	0
23	1081	3243	95	285	3528	0
24	1176	3528	99	297	3825	0
25	1275	3825	103	309	4134	0

Based on average integration time of 3 sec.

All quantities in seconds unless specified otherwise.

Table 5.2 Additional time required per Fourier mode to add an entire-domain mode

			SUBDOMAIN			
Initial modes	Elements to fill	Fill time	Elements req'd to add mode	Add time	Total CPU time	Computation overhead
1	3	9	10	30	39	9 sec
2	10	30	21	63	93	30 sec
3	21	63	36	108	171	1.05 min
4	36	108	55	165	273	1.8 min
5	55	165	78	234	399	2.75 min
6	78	234	105	315	549	3.9 min
7	105	315	136	408	723	5.25 min
8	136	408	171	513	921	6.8 min
9	171	513	210	630	1143	8.55 min
10	210	630	253	759	1389	10.5 min
11	253	759	300	900	1659	12.65 min
12	300	900	351	1053	1953	15 min
13	351	1053	406	1218	2271	17.55 min
14	406	1218	465	1395	2613	20.3 min
15	465	1395	528	1584	2979	23.25 min
16	528	1584	595	1785	3369	26.4 min
17	595	1785	666	1998	3783	29.75 min
18	666	1998	741	2223	4221	33.3 min
19	741	2223	820	2460	4683	37.05 min
20	820	2460	903	2709	5169	41 min
21	903	2709	990	2970	5679	45.15 min
22	990	2970	1081	3243	6213	49.5 min
23	1081	3243	1176	3528	6771	54.05 min
24	1176	3528	1275	3825	7353	58.8 min
25	1275	3825	1378	4134	7959	1.0625 hr

Based on average integration time of 3 sec.

All quantities in seconds unless specified otherwise.

Table 5.3 Additional time required per Fourier mode to add a subdomain segment

(465 seconds) to the fill time for a total of 10 minutes (630 seconds),

$$\begin{aligned} CPU \text{ time} &= (165)_5 \text{ initial modes} + 69 + 81 + 93 + 105 + 117 \\ &= 630 \text{ seconds to compute 10 modes.} \end{aligned} \quad (5.5)$$

The same calculation is made for an initial choice of five subdomain segments. It takes the same 2.75 minutes (165 seconds) to fill the subdomain $[Z]$ as it does for entire-domain. Doubling the number of segments to ten adds 35 minutes (2100 seconds) to the fill time for a total of 37.75 minutes (2265 seconds). This is 387% more time to fill,

$$\begin{aligned} CPU \text{ time} &= (165)_5 \text{ initial segments} + 234 + 315 + 408 + 513 + 630 \\ &= 2265 \text{ seconds to compute 10 segments.} \end{aligned} \quad (5.6)$$

A more realistic situation, however, is that because of the smoothness and appropriate functionality of the entire-domain basis functions, many more subdomain segments will be required to achieve the same accuracy. The processing time for ten entire-domain modes is 10.5 minutes (630 seconds), whether ten are chosen initially or additional modes are added to make ten. Since ten entire-domain modes achieves the accuracy desired, let the subdomain comparison start with ten segments. Suppose that to achieve accuracy in this case, the number of segments is incrementally doubled to twenty. This results in 4.27 additional hours (15,375 seconds) for a total of 4.45 hours (16,005 seconds) to fill $[Z]$. This is 3.76 hours more (551% longer) than if twenty segments were initially chosen and 4.32 hours more (2440% longer) than it took to achieve the same results as in the entire-domain case! The time difference is even worse than this because it is also compounded by the number of Fourier modes,

$$\begin{aligned} CPU \text{ time} &= (630)_{10} + 759 + 900 + 1053 + 1218 + 1395 + 1584 + 1785 + 1998 + 2223 + 2460 \\ &= 16005 \text{ seconds to compute 20 segments.} \end{aligned} \quad (5.7)$$

A summary of the savings in computation time for the above examples is presented in Table 5.4.

	Add time	Total time	
SUBDOMAIN			
Initial modes = 5		2.75 min	
Final modes = 10	35 min	37.75 min	
Initial modes = 10		10.50 min	
Final modes = 20	4.27 hrs	4.45 hrs	

ENTIRE-DOMAIN			<i>Savings over subdomain</i>
Initial modes = 5		2.75 min	
Final modes = 10	7.75 min	10.5 min	<i>4.32 hours saved</i>

Table 5.4 Summary of CPU time savings per Fourier mode

VI. Conclusions and Recommendations

This chapter discusses the achievements of this research. The impacts of this work are summarized and recommendations are made for future work in this area.

6.1 Conclusions

The primary motivation for this research involved improving the numerical methods used to obtain the electromagnetic scattering from perfectly electrically conducting bodies of revolution. Such bodies are used to calibrate the measurement systems of radar ranges using a background subtraction method. Current approaches use Method of Moments based computer codes which employ subdomain basis expansion functions to calculate an approximate solution to the current density induced on the surface of the body by an incoming plane-wave. The accuracy of the approximation is limited by the number of subdomain segments used in the expansion. A large number of these segments are required to accurately represent the current density. Computation time becomes inhibitive for an accurate solution, particularly for a body of large electrical size. Incrementally increasing the number of subdomain segments used in order to increase accuracy requires re-discretization and loss of previously calculated results. Entire-domain basis functions can solve both of these problems. Although many texts make reference to the possibility of using entire-domain basis functions for expansion of the current density, they all default to the apparent simplicity of subdomain basis functions. A search of the literature also yields few examples of the use of entire-domain basis functions.

As a proof of the concept of using entire-domain basis functions to compute the scattering of a body of revolution, the unknown current density on a perfectly electrically conducting sphere was expanded using Chebyshev polynomials of the first kind. The Method of Moments was then used to solve for the current density. Galerkin's method of testing allowed an approximate 50% reduction in required computations. A sphere was chosen to enable comparison to the Mie series, a known exact solution. The entire-domain solution using the Chebyshev basis was shown to be a better approximation of the

scattering cross-section in many fewer modes (about 5) than an equivalent trial using a subdomain pulse basis.

Since the current density is a smooth variation over the surface, the Chebyshev basis functions were a better approximation than discontinuous subdomain pulses. This was a significant factor in reducing the number of modes required in the approximation and the matrix size of the solution. Computation time was dramatically decreased. The computational time required to obtain an initial solution and then double the number of entire-domain modes used in order to increase the accuracy of the solution was found to be the same as if the final number of modes were used initially. Using subdomain basis segments took hours longer—clearly an advantage of entire-domain basis functions that overcomes the initial complexity of their implementation.

6.2 Recommendations for Future Research

Although the results presented in this report accomplish the goal of the research effort by showing the obvious computational advantages and time savings of using entire-domain basis functions for the given problem, there are several areas in which further work could follow.

First, an accurate solution was not obtained for spheres of smaller electrical sizes. This was due to the handling of the weak singular nature of the three-dimensional free-space Green's function by means of imposing an equivalent separation in the minimum distance between the testing functions and the current expansion functions—an approach that has been successful in other similar problems. The small phase approximation introduced was found to be unacceptable for spheres of smaller electrical sizes. Methods exist for extracting the singularity and evaluating the integrals in the region surrounding the singular point separately. Future research would use such a method to handle the singular behavior of the integrands more rigorously. The Chebyshev weighting factor for true orthogonality could also be implemented.

Second, a sphere was chosen in this effort to demonstrate the advantages of entire-domain basis functions because an exact solution exists for comparison. Real interest

in this method lies in the ability to accurately calculate the scattering from bodies of revolution to which no exact solution is known. Applying appropriately chosen entire-domain basis functions to the solution of scattering from more complex and advantageous geometries would be useful. Examples of such geometries might be elliptical bodies of low cross-section, the right-circular cylinder used in cylindrical calibration methods for radar ranges, and other bodies of revolution with discontinuities (such as corners) in their generating arc. Investigation might be made into the appropriateness of the method for bodies with concave and/or convex regions. Additionally, it would be useful to study the effects of using various entire-domain basis functions on a given body of revolution.

Third, actual range measurements could be made under the best of controlled conditions following computation of the scattering by this entire-domain method for various bodies of revolution. Quantification of the actual number of entire-domain modes required to achieve given tolerances could be done.

Fourth, an error analysis study could be performed based on the fact that the entire-domain functions contain frequency content information, and thus, the expansion coefficients are related to the frequency content of the unknown current. The study would show the relationship between the error and the number of entire-domain basis functions used (something that cannot be done with subdomain basis functions).

Appendix A. The Computer Code

This appendix contains MATLAB 5 computer code for computing the scattering cross-section from a body of revolution. The function GEO defines the geometry for a sphere and can be rewritten to return similar parameters for another geometry. The code is initiated by a call to MAINSPHERE with the appropriate inputs as outlined in the code. The other functions are called by MAINSPHERE.

```
%%%%%%%%%%%%%%%%%%%%%%%%%%%%%%%%%%%%%%%%%%%%%%%%%%%%%%%%%%%%%%%%%%%%%%%%%%%%%%
function [sdout] = mainsphere(p1, p2, p3, p4, p5, p6)
%usage: [sdout] = mainsphere(a_samples, sdmax, fmin, fmax, theta, 'ed' or 'sd')
%%%%%%%%%%%%%%%%%%%%%%%%%%%%%%%%%%%%%%%%%%%%%%%%%%%%%%%%%%%%%%%%%%%%%%%%%%%%%%
%% This in the main program for the entire (or sub) domain analysis %%
%%%%%%%%%%%%%%%%%%%%%%%%%%%%%%%%%%%%%%%%%%%%%%%%%%%%%%%%%%%%%%%%%%%%%%%%%%%%%%

%%%%%%%%%%%%%%%%%%%%%%%%%%%%%%%%%%%%%%%%%%%%%%%%%%%%%%%%%%%%%%%%%%%%%%%%%%%%%%
%%%%% INITIALIZE VARIABLES %%%%%
%%%%%%%%%%%%%%%%%%%%%%%%%%%%%%%%%%%%%%%%%%%%%%%%%%%%%%%%%%%%%%%%%%%%%%%%%%%%%%
global k a skosh % geo and other constants
global fidd % output control, 1=display
global n ntest nbasis % mode indices
global tlo thi tplo tphi % integration limits
global theta_t % monostatic angle
global T % basis polynomial table
global bpx bpy wfx % 2d gaussian roots and weights (for v)
global bpx3 bpy3 bpz3 wfxyz % 3d gaussian roots and weights (for z)

if p6=='sd'
    T = zeros(25,25);
    T(:,25) = [1]; % pulse basis polynomial coefficient
else
    T = maket; % make the Chebyshev basis lookup table
end;

fidd = 1; % display
lambda = 1; % wavelength (1 = normalized)
k = 2*pi/lambda; % wave number

%%%%%%%%%%%%%%%%%%%%%%%%%%%%%%%%%%%%%%%%%%%%%%%%%%%%%%%%%%%%%%%%%%%%%%%%%%%%%%
%%%%% CHANGEABLES %%%%%
```



```

%%%%%%%%%%%%%%%%%%%%%%%%%%%%%%%%%%%%%%%%%%%%%%%%%%%%%%%%%%%%%%%%%%%%%%%%
a_samples = p1; % sphere radii vector
sdmax      = p2; % initial max sub-domain mode
fmin       = p3; % min fourier mode (set ~0 for partial computation)
fmax       = p4; % max fourier mode
theta      = p5; % increments in theta
zpoints    = [30 30 30]; % # of integration points for z-matrix
vpoints    = [30 30]; % # of integration points for v-matrix
%fname (below) % save filename.mat
%fdir (below) % save directory

%%%%%%%%%%%%%%%%%%%%%%%%%%%%%%%%%%%%%%%%%%%%%%%%%%%%%%%%%%%%%%%%%%%%%%%%
%%%%%% ENTIRE DOMAIN, MOMENT METHOD %%%%%%
%%%%%%%%%%%%%%%%%%%%%%%%%%%%%%%%%%%%%%%%%%%%%%%%%%%%%%%%%%%%%%%%%%%%%%%%

for aindex=1:length(a_samples)
    a      = a_samples(aindex)/k; % sphere radius
    tmax   = pi*a; % total arclength of generating curve
    skosh  = .01;

    fname  = ['sp' num2str(floor(k*a*10)) p6 num2str(sdmax) 'f' num2str(fmax)];
    fdir   = '~/outfiles/';
    eval(['save ', fdir, fname, ' a sdmax fmin fmax theta zpoints vpoints;']);

    if p6=='sd'% make array of integration limits
        limits = makelimits(tmax, sdmax);
    else
        tlo = 0;
        thi = pi*a;
        tplo = tlo;
        tphi = thi;
    end;

    [bpx bpy wfx] = grule2d(vpoints(1), vpoints(2));
    [bpx3 bpy3 bpz3 wfxyz] = grule3d(zpoints(1), zpoints(2), zpoints(3));

    for nfourier = fmin:fmax % fourier mode loop

        makezv; % make Z, V, R, I

        % a test In for convergence here

        % Store variables
        ns = num2str(nfourier);
        eval(['Rt' ns ' = transpose(Rt);']);
    end
end

```

```

        eval(['Rp' ns ' = transpose(Rp);']);
        eval(['I' ns '=In;']);
        eval(['z' ns '=z;']);
        eval(['v' ns '=v;']);
        eval(['save ', fdir, fname, ' Rt' ns ' Rp' ns ' I'...
ns ' z' ns ' v' ns ' -append;']);

    end; % for nfourier

    if fmin==0
        comprcs; % compute rcs
        eval(['save ', fdir, fname, ' sigma_lam2 sigma_db -append;']);
        plotrcs; % plot rcs
        sdout = sigma_db;
    else
        disp('Partial series of f-modes computed, no sigma calculated.');
```

sdout = 9999;

```

    end; % if

end; % for aindex

%%%%%%%%%%%%%%%%%%%%%%%%%%%%%%%%%%%%%%%%%%%%%%%%%%%%%%%%%%%%%%%%%%%%%%%%
% Procedure: makezv.m
% Makes the z and v matrices and computes I
% Also makes the Rt and Rp matrices

t_0 = cputime;

n = nfourier;
A = zeros(sdmax+1);
B = A;
C = A;
D = A;
E = zeros(sdmax+1, length(theta));
F = E;

%%%%%%%%%%%%%%%%%%%%%%%%%%%%%%%%%%%%%%%%%%%%%%%%%%%%%%%%%%%%%%%%%%%%%%%%
% Compute for initial number of sd modes
for ntest = 0:sdmax

    for nbasis = 0:sdmax
        if p6=='sd'
            tlo = limits(ntest+1,1);
```

```

        thi = limits(ntest+1,2);
        tplo = limits(nbasis+1,1);
        tphi = limits(nbasis+1,2);
    end; % if

    fprintf(fidd,'\n----ztp----\n');
    tc=cputime; B(ntest+1,nbasis+1) = ztp2; t_cpu=cputime-tc;
    fprintf(fidd,'\nElapsed cpu time:  %f seconds.\n',t_cpu);

    if nbasis <= ntest
        fprintf(fidd,'\n----ztt----\n');
        tc=cputime; A(ntest+1,nbasis+1) = ztt2; t_cpu=cputime-tc;
        fprintf(fidd,'\nElapsed cpu time:  %f seconds.\n',t_cpu);
        fprintf(fidd,'\n----zpp----\n');
        tc=cputime; D(ntest+1,nbasis+1) = zpp2; t_cpu=cputime-tc;
        fprintf(fidd,'\nElapsed cpu time:  %f seconds.\n',t_cpu);
    end; % if

end; % for nbasis

for th = 1:length(theta);
    theta_t = theta(th);

    fprintf(fidd,'\n----vt----\n');
    tc=cputime; E(ntest+1, th) = vt; t_cpu=cputime-tc;
    fprintf(fidd,'\nElapsed cpu time:  %f seconds.\n',t_cpu);
    fprintf(fidd,'\n----vp----\n');
    tc=cputime; F(ntest+1, th) = vp; t_cpu=cputime-tc;
    fprintf(fidd,'\nElapsed cpu time:  %f seconds.\n',t_cpu);

    n = -n;
    Rt(ntest+1, th) = vt;
    Rp(ntest+1, th) = vp;
    n = -n; % restore

end; % for th

end; % for ntest

A = tril(A) + transpose(tril(A, -1)); % exploit symmetries
D = tril(D) + transpose(tril(D, -1));
C = -transpose(B);

z = [A, B; C, D];
v = [E; F];

```

```

    fprintf(fiddd, '\n----Invert----\n');
    tc=cputime; In = inv(z) * v; t_cpu=cputime-tc;
    fprintf(fiddd, '\nElapsed cpu time:  %f seconds.\n', t_cpu);

t_tot=cputime - t_0;
disp(['Total runtime:  ' num2str(t_tot)]);

%%%%%%%%%%%%%%%%%%%%%%%%%%%%%%%%%%%%%%%%%%%%%%%%%%%%%%%%%%%%%%%%%%%%%%%%
% Procedure:  comprcs.m

fprintf(fiddd, '\n----Compute RCS----\n');

for th = 1:length(theta)
    theta_t = theta(th);
    nsum = 0;
    for n = 1:fmax
        fprintf(fiddd, '\nAdd n=%d\n', n);
        ns = num2str(n);
        eval(['In = I' ns '(:, th);']);
        len = length(In);
        mid = len/2;
        It = In(1:mid);
        Ip = In(mid+1:len);
        nsum = nsum + eval(['Rt' ns '(th, :) * It + Rp' ns '(th, :) * Ip']);
    end; % for n

    In = IO(:, th);
    len = length(In);
    mid = len/2;
    It0 = In(1 : mid);
    Ip0 = In(mid+1 : len);
    sigma_lam2(th) = 1/(4*pi^3) * ( abs(.5 * Rt0(th, :) * It0 + ...
.5 * Rp0(th, :) * Ip0 + nsum) )^2;

end; % for th

if exist('aindex')==1
    sigma_db(aindex) = 10*log10(sigma_lam2);
else
    sigma_db=10*log10(sigma_lam2);
end;

```

```
%%%%%%%%%%%%%%%%%%%%%%%%%%%%%%%%%%%%%%%%%%%%%%%%%%%%%%%%%%%%%%%%%%%%%%%%
```

```
% Procedure: plotrcs.m
```

```
figure;  
plot(theta*180/pi, sigma_db);  
title({'Scattering Cross-Section', ['Date: ', date, ' Datafile: ', ...  
fdir, ' ', fname]});
```

```
sdata = num2str([sigma_db(1:10); sigma_db(11:20)]);  
xlabel({'Theta (deg)', sdata});  
ylabel('Sigma/lambda^2 (dBsm)');  
grid on;
```

```
%%%%%%%%%%%%%%%%%%%%%%%%%%%%%%%%%%%%%%%%%%%%%%%%%%%%%%%%%%%%%%%%%%%%%%%%
```

```
function [A] = makelimits(tmax, sdmax)  
% makes an n x 2 array of integration limits  
% for the subdomain analysis
```

```
% as in entire domain, the modes include the 0-mode  
delta = tmax / (sdmax + 1);  
lo(1) = 0;  
hi(1) = delta;  
for index = 2:sdmax+1  
    lo(index) = hi(index-1);  
    hi(index) = lo(index) + delta;  
end;  
  
A = [lo', hi'];
```

```
%%%%%%%%%%%%%%%%%%%%%%%%%%%%%%%%%%%%%%%%%%%%%%%%%%%%%%%%%%%%%%%%%%%%%%%%
```

```
function [A] = maket  
% returns the vector of coefficients  
% of the Chebyshev polynomial of mode "mode"
```

```
hi=25;  
t=zeros(hi);  
  
t(1,hi) = [1];  
t(2,hi-1:hi) = [1 0];
```

```

for nn=3:25
    s = conv([2 0],t(nn-1,:));
    t(nn,1:hi) = s(2:hi+1) - t(nn-2,:);
end; % for

```

```

A = t;

```

```

%%%%%%%%%%%%%%%%%%%%%%%%%%%%%%%%%%%%%%%%%%%%%%%%%%%%%%%%%%%%%%%%%%%%%%%%

```

```

function [bpx,bpy,wfxy] = grule2d (nquadx,nquady)

```

```

[bpxv,wfxv]=grule(nquadx);
[bpyv,wfyv]=grule(nquady);
[bpx,bpy]=meshgrid(bpxv,bpyv);
[wfx,wfy]=meshgrid(wfxv,wfyv);
wfxy=wfx.*wfy;

```

```

%%%%%%%%%%%%%%%%%%%%%%%%%%%%%%%%%%%%%%%%%%%%%%%%%%%%%%%%%%%%%%%%%%%%%%%%

```

```

function [bpx,bpy,bpz,wfxyz] = grule3d (nquadx,nquady,nquadz)

```

```

[bpxv,wfxv]=grule(nquadx);
[bpyv,wfyv]=grule(nquady);
[bpzv,wfzv]=grule(nquadz);
[bpx,bpy,bpz]=meshgrid(bpxv,bpyv,bpzv);
[wfx,wfy,wfz]=meshgrid(wfxv,wfyv,wfzv);
wfxyz=wfx.*wfy.*wfz;

```

```

%%%%%%%%%%%%%%%%%%%%%%%%%%%%%%%%%%%%%%%%%%%%%%%%%%%%%%%%%%%%%%%%%%%%%%%%

```

```

function [bp,wf]=grule(n)

```

```

% This function computes Gauss base points and weight factors
% using the algorithm given by Davis and Rabinowitz in 'Methods
% of Numerical Integration', page 365, Academic Press, 1975.
% by Howard Wilson of the University of Alabama, 1990
% included in the Numerical Integration Toolbox*
% *duplicated here for convenience of the reader
bp=zeros(n,1); wf=bp; iter=2; m=fix((n+1)/2); e1=n*(n+1);
mm=4*m-1; t=(pi/(4*n+2))*(3:4:mm); nn=(1-(1-1/n)/(8*n*n));
xo=nn*cos(t);
for j=1:iter
    pkm1=1; pk=xo;
    for k=2:n

```

```

        t1=xo.*pk; pkp1=t1-pkm1-(t1-pkm1)/k+t1;
        pkm1=pk; pk=pkp1;
    end
    den=1.-xo.*xo; d1=n*(pkm1-xo.*pk); dpn=d1./den;
    d2pn=(2.*xo.*dpn-e1.*pk)./den;
    d3pn=(4*xo.*d2pn+(2-e1).*dpn)./den;
    d4pn=(6*xo.*d3pn+(6-e1).*d2pn)./den;
    u=pk./dpn; v=d2pn./dpn;
    h=-u.*(1+(.5*u).*(v+u.*(v.*v-u.*d3pn./(3*dpn)))));
    p=pk+h.*(dpn+(.5*h).*(d2pn+(h/3).*(d3pn+.25*h.*d4pn)));
    dp=dpn+h.*(d2pn+(.5*h).*(d3pn+h.*d4pn/3));
    h=h-p./dp; xo=xo+h;
end
bp=-xo-h;
fx=d1-h.*e1.*(pk+(h/2).*(dpn+(h/3).*(...
    d2pn+(h/4).*(d3pn+(.2*h).*d4pn))));
wf=2*(1-bp.^2)./(fx.*fx);
if (m+m) > n, bp(m)=0; end
if ~(m+m) == n, m=m-1; end
jj=1:m; n1j=(n+1-jj); bp(n1j)=-bp(jj); wf(n1j)=wf(jj);
% end

```

%%

function vol = gquad2d(fun,xlow,xhigh,ylow,yhigh,bpx,bpy,wfxy)
 %based on a routine by Bryce Gardner, Purdue University, Spring 1993

%Map to x

```

qx=(xhigh-xlow)/2;
px=(xhigh+xlow)/2;
x=qx*bpx+px;

```

%Map to y

```

qy=(yhigh-ylow)/2;
py=(yhigh+ylow)/2;
y=qy*bpy+py;

```

```

fv = feval(fun,x,y);
vol = sum(sum(wfxy.*fv))*qx*qy;

```

```

fprintf(1,'The %d point integration of ''%s'' gives\n %20.15f ...
+ i%20.15f\n', length(bpx), fun, real(vol), imag(vol));

```

```
%%%%%%%%%%%%%%%%%%%%%%%%%%%%%%%%%%%%%%%%
```

```
function vol = gquad3d(fun,xlow,xhigh,ylow,yhigh,zlow,zhigh,bpx,bpy,bpz,wfxyz)
%based on a routine by Bryce Gardner, Purdue University, Spring 1993
```

```
%Map to x
```

```
qx=(xhigh-xlow)/2;
px=(xhigh+xlow)/2;
x=qx*bpx+px;
```

```
%Map to y
```

```
qy=(yhigh-ylow)/2;
py=(yhigh+ylow)/2;
y=qy*bpy+py;
```

```
%Map to z
```

```
qz=(zhigh-zlow)/2;
pz=(zhigh+zlow)/2;
z=qz*bpz+pz;
```

```
fv = feval(fun,x,y,z);
```

```
vol = sum(sum(sum(wfxyz.*fv)))*qx*qy*qz;
```

```
fprintf(1,'The %d point integration of ''%s'' gives\n%20.15f ...
+ i%20.15f\n',length(bpx),fun,real(vol),imag(vol));
```

```
%%%%%%%%%%%%%%%%%%%%%%%%%%%%%%%%%%%%%%%%
```

```
function [A] = basis(mode, tp)
```

```
% Returns the value of the basis function
% of mode 'mode' evaluated at tp.
```

```
global T tphi
```

```
s = 2 * tp ./ tphi - 1; % scales domain to +-1
```

```
% workaround for 3d (nu1, nu2 are not needed)
```

```
A1=polyval(T(mode+1,:),s(:,1,1));
[nu1, A, nu2]=meshgrid(A1, A1, A1);
```

```
%%%%%%%%%%%%%%%%%%%%%%%%%%%%%%%%%%%%%%%%
```

```
function [A] = derivtp(mode, tp)
```

```
% Computes the partial derivative with respect to tp
```



```

% of rho(tp) * basis(tp)
% assumes sphere
global a

A = cos(tp/a) .* basis(mode, tp) + a*sin(tp/a) .* dbasis(mode, tp);

```

```

%%%%%%%%%%%%%%%%%%%%%%%%%%%%%%%%%%%%%%%%%%%%%%%%%%%%%%%%%%%%%%%%%%%%%%%%
function [A] = dbasis(mode, tp)
% returns the value of the derivative
% of the basis function @ mode, tp
global T tphi

s = 2 * tp ./ tphi - 1; % scales domain to +-1

% workaround for 3d (nu1, nu2 are not needed)
A1 = polyval(polyder(T(mode+1,:)),s(:,1,1));
[nu1, A, nu2]=meshgrid(A1, A1, A1);

```

```

%%%%%%%%%%%%%%%%%%%%%%%%%%%%%%%%%%%%%%%%%%%%%%%%%%%%%%%%%%%%%%%%%%%%%%%%
function [rho, zee, vee] = geo(t)
% Computes the geometric parameters for a
% *** SPHERE ***
% all positive z
global a skosh

next_t = t + .00001;
rho = a * sin(t/a);
rho_next = a * sin(next_t/a);
zee = -a * cos(t/a) + a;
zee_next = -a * cos(next_t/a) + a;
drho = rho_next - rho;
dzee = zee_next - zee;
hyp = sqrt(drho.^2 + dzee.^2);
vee = asin(drho./hyp);

```

```

%%%%%%%%%%%%%%%%%%%%%%%%%%%%%%%%%%%%%%%%%%%%%%%%%%%%%%%%%%%%%%%%%%%%%%%%
function [A] = test(mode, t)
% Returns the value of the testing function
% of mode 'mode' evaluated at t.

```

```

% Galerkin (basis = test)
global T thi

s = 2 * t ./ thi - 1; % scales domain to +-1

if length(size(s)) == 3
    % workaround for 3d (nu1, nu2 are not needed)
    A1=polyval(T(mode+1,:),s(1,:,1));
    [A, nu1, nu2]=meshgrid(A1, A1, A1);
else
    A=polyval(T(mode+1,:),s);
end;

%%%%%%%%%%%%%%%%%%%%%%%%%%%%%%%%%%%%%%%%%%%%%%%%%%%%%%%%%%%%%%%%%%%%%%%%
function [A] = derivt(mode, t)
% computes the partial derivative with respect
% to t of rho(t) * test(t).
% assumes sphere
global a

A = cos(t/a) .* test(mode, t) + a*sin(t/a).*dtest(mode, t);

%%%%%%%%%%%%%%%%%%%%%%%%%%%%%%%%%%%%%%%%%%%%%%%%%%%%%%%%%%%%%%%%%%%%%%%%
function [A] = dtest(mode, t)
% returns the value of the derivative
% of the test function @ mode, t
% galerkin: test = basis
global T thi

s = 2 * t ./ thi - 1; % scales domain to +-1

% workaround for 3d (nu1, nu2 are not needed)
A1 = polyval(polyder(T(mode+1,:)),s(1,:,1));
[A, nu1, nu2]=meshgrid(A1, A1, A1);

%%%%%%%%%%%%%%%%%%%%%%%%%%%%%%%%%%%%%%%%%%%%%%%%%%%%%%%%%%%%%%%%%%%%%%%%
function [A] = ztt2
% Computes an impedance matrix element of ztt
global tplo tphi tlo thi
global bpx3 bpy3 bpz3 wfxyz

```

```
A = gquad3d('zttarg2', tlo, thi, tplo, tphi, 0, pi, bpx3, bpy3, bpz3, wxyz);
```

```
%%%%%%%%%%%%%%%%%%%%%%%%%%%%%%%%%%%%%%%%%%%%%%%%%%%%%%%%%%%%%%%%%%%%%%%%%
```

```
function [A] = zttarg2(t,tp,phip)
```

```
% Argument for ztt integration
```

```
global k n skosh ntest nbasis
```

```
[rho_t, zee_t, vee_t] = geo(t);
```

```
[rho_tp, zee_tp, vee_tp] = geo(tp);
```

```
R = sqrt( skosh.^2 + (rho_t-rho_tp).^2 + (zee_t-zee_tp).^2 + ...
```

```
4*rho_t.*rho_tp.*(sin(hip/2)).^2 );
```

```
arg4 = exp(-j*k*R)./(k*R) .* cos(n*phip);
```

```
arg5 = exp(-j*k*R)./(k*R) .* cos(hip) .* cos(n*phip);
```

```
A1 = j*k^2*rho_t.*test(ntest,t).*rho_tp.*basis(nbasis,tp).* ...
```

```
( arg5.*sin(vee_t).*sin(vee_tp) + arg4.*cos(vee_t).*cos(vee_tp) );
```

```
A2 = -j.*derivt(ntest,t).*derivtp(nbasis,tp).*arg4;
```

```
A = A1 + A2;
```

```
%%%%%%%%%%%%%%%%%%%%%%%%%%%%%%%%%%%%%%%%%%%%%%%%%%%%%%%%%%%%%%%%%%%%%%%%%
```

```
function [A] = ztp2
```

```
% Computes an impedance matrix element of ztp
```

```
global tplo tphi tlo thi
```

```
global bpx3 bpy3 bpz3 wxyz
```

```
A = gquad3d('ztparg2', tlo, thi, tplo, tphi, 0, pi, bpx3, bpy3, bpz3, wxyz);
```

```
%%%%%%%%%%%%%%%%%%%%%%%%%%%%%%%%%%%%%%%%%%%%%%%%%%%%%%%%%%%%%%%%%%%%%%%%%
```

```
function [A] = ztparg2(t,tp,phip)
```

```
% Argument for ztp integration
```

```
global k n skosh ntest nbasis
```

```
[rho_t, zee_t, vee_t] = geo(t);
```

```
[rho_tp, zee_tp, vee_tp] = geo(tp);
```

```
R = sqrt( skosh.^2 + (rho_t-rho_tp).^2 + (zee_t-zee_tp).^2 + ...
```

```
4*rho_t.*rho_tp.*(sin(hip/2)).^2 );
```

```

arg4 = exp(-j*k*R)./(k*R) .* cos(n*phip);
arg6 = exp(-j*k*R)./(k*R) .* sin(phip) .* sin(n*phip);

A1 = rho_tp.*basis(nbasis,tp).*k^2.*rho_t.*test(ntest,t).*arg6.*sin(vee_t);
A2 = rho_tp.*basis(nbasis,tp).* n./rho_tp .*derivt(ntest,t).*arg4;
A = A1 + A2;

```

```

%%%%%%%%%%%%%%%%%%%%%%%%%%%%%%%%%%%%%%%%%%%%%%%%%%%%%%%%%%%%%%%%%%%%%%%%

```

```

function [A] = zpt2
% Computes an impedance matrix element of zpt
global tplo tphi tlo thi
global bpx3 bpy3 bpz3 wfxyz

A = gquad3d('zptarg2', tlo, thi, tplo, tphi, 0, pi, bpx3, bpy3, bpz3, wfxyz);

```

```

%%%%%%%%%%%%%%%%%%%%%%%%%%%%%%%%%%%%%%%%%%%%%%%%%%%%%%%%%%%%%%%%%%%%%%%%

```

```

function [A] = zptarg2(t,tp,phip)
% Argument for zpt integration
global k n skosh ntest nbasis

[rho_t, zee_t, vee_t] = geo(t);
[rho_tp, zee_tp, vee_tp] = geo(tp);

R = sqrt( skosh.^2 + (rho_t-rho_tp).^2 + (zee_t-zee_tp).^2 + ...
4*rho_t.*rho_tp.*(sin(phip/2)).^2 );
arg4 = exp(-j*k*R)./(k*R) .* cos(n*phip);
arg6 = exp(-j*k*R)./(k*R) .* sin(phip) .* sin(n*phip);

A1 = -rho_t.*test(ntest, t).*k^2.*rho_tp.*basis(nbasis,tp).*arg6.*sin(vee_tp);
A2 = -rho_t.*test(ntest, t).* n./rho_t .*derivtp(nbasis,tp).*arg4;
A = A1 + A2;

```

```

%%%%%%%%%%%%%%%%%%%%%%%%%%%%%%%%%%%%%%%%%%%%%%%%%%%%%%%%%%%%%%%%%%%%%%%%

```

```

function [A] = zpp2
% Computes an impedance matrix element of zpp
global tplo tphi tlo thi
global bpx3 bpy3 bpz3 wfxyz

A = gquad3d('zpparg2', tlo, thi, tplo, tphi, 0, pi, bpx3, bpy3, bpz3, wfxyz);

```

```

%%%%%%%%%%%%%%%%%%%%%%%%%%%%%%%%%%%%%%%%%%%%%%%%%%%%%%%%%%%%%%%%%%%%%%%%
function [A] = zpparg2(t,tp,phip)
% Argument for zpp integration
global k n skosh ntest nbasis

[rho_t, zee_t, vee_t] = geo(t);
[rho_tp, zee_tp, vee_tp] = geo(tp);

R = sqrt( skosh.^2 + (rho_t-rho_tp).^2 + (zee_t-zee_tp).^2 + ...
4*rho_t.*rho_tp.*(sin(hip/2)).^2 );
arg4 = exp(-j*k*R)./(k*R) .* cos(n*phip);
arg5 = exp(-j*k*R)./(k*R) .* cos(hip) .* cos(n*phip);

A = j*rho_t.*test(ntest,t).*rho_tp.*basis(nbasis,tp).* ...
( k^2.*arg5 - n^2./(rho_t.*rho_tp) .* arg4 );

```

```

%%%%%%%%%%%%%%%%%%%%%%%%%%%%%%%%%%%%%%%%%%%%%%%%%%%%%%%%%%%%%%%%%%%%%%%%
function [A] = vt
% Computes a voltage matrix element of vt
global tlo thi
global bpx bpy wfxxy

A = gquad2d('vtarg', tlo, thi, 0, 2*pi, bpx, bpy, wfxxy);

```

```

%%%%%%%%%%%%%%%%%%%%%%%%%%%%%%%%%%%%%%%%%%%%%%%%%%%%%%%%%%%%%%%%%%%%%%%%
function [A] = vtarg(t,phi)
% argument for vt integral.
global k n ntest theta_t

[rho, zee, vee] = geo(t);
dphi = sin(vee) .* sin(phi);
%dtheta = sin(vee(t)) .* cos(phi);
minus_kr = k * zee .* cos(theta_t) + k * rho .* sin(theta_t) .* cos(phi);
preA = k * rho .* test(ntest,t) .* exp(j.*(minus_kr - n.*phi));
A = preA .* dphi;

```

```

%%%%%%%%%%%%%%%%%%%%%%%%%%%%%%%%%%%%%%%%%%%%%%%%%%%%%%%%%%%%%%%%%%%%%%%%
function [A] = vp
% Computes a voltage matrix element of vp
global tlo thi
global bpx bpy wfx

A = gquad2d('vparg', tlo, thi, 0, 2*pi, bpx, bpy, wfx);

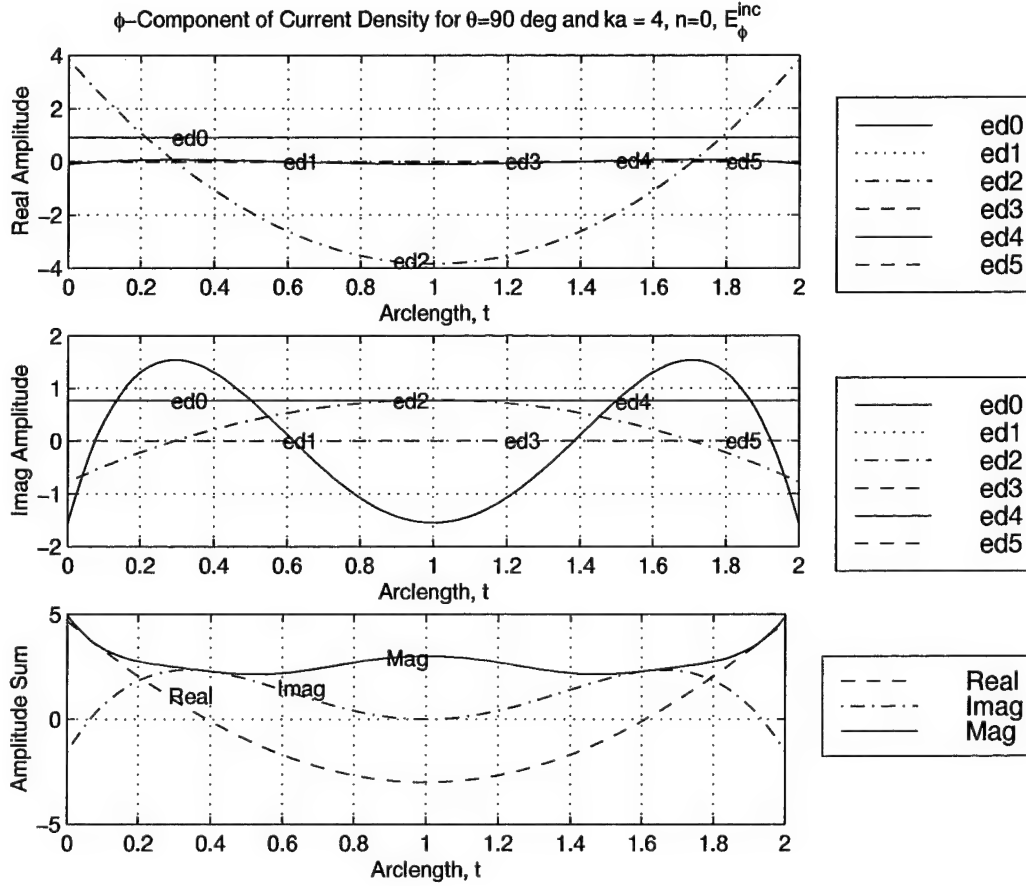
%%%%%%%%%%%%%%%%%%%%%%%%%%%%%%%%%%%%%%%%%%%%%%%%%%%%%%%%%%%%%%%%%%%%%%%%
function [A] = vparg(t,phi)
% argument for vp integral.
global k n ntest theta_t

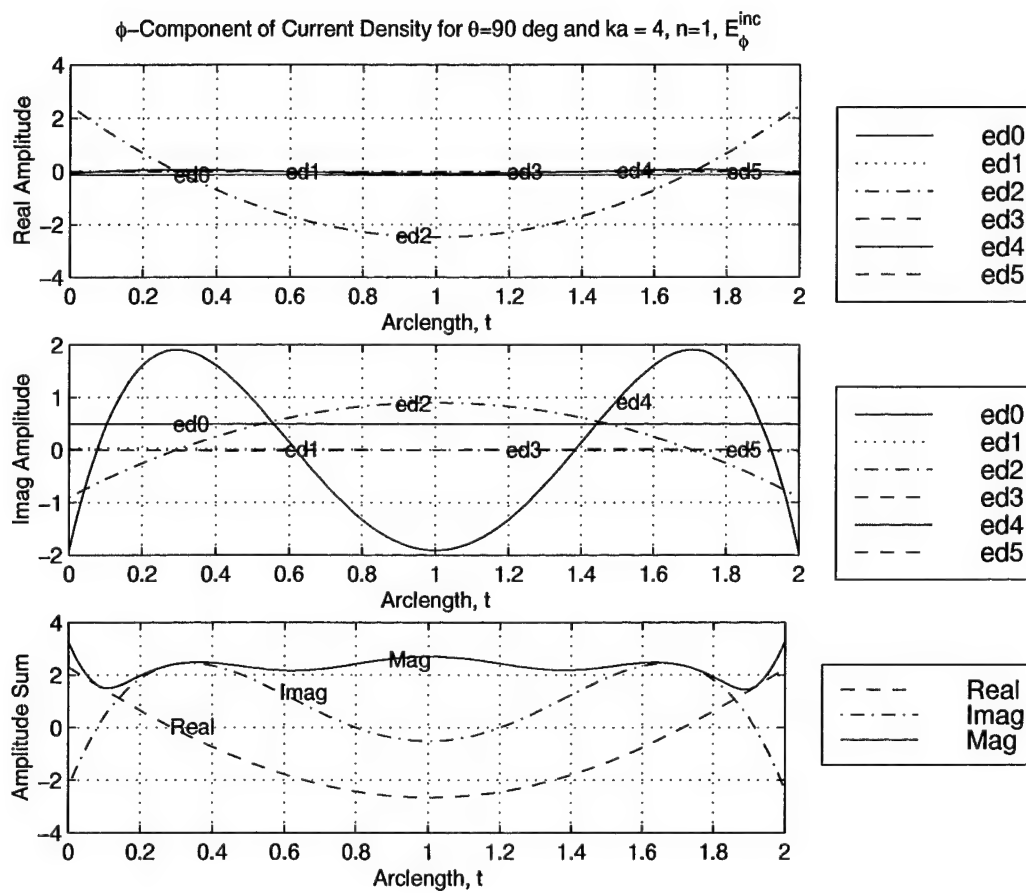
[rho, zee, vee] = geo(t);
dphi = cos(phi);
% dtheta = -sin(phi);
minus_kr = k * zee .* cos(theta_t) + k * rho .* sin(theta_t) .* cos(phi);
preA = k * rho .* test(ntest,t) .* exp(j*(minus_kr - n.*phi));
A = preA .* dphi;

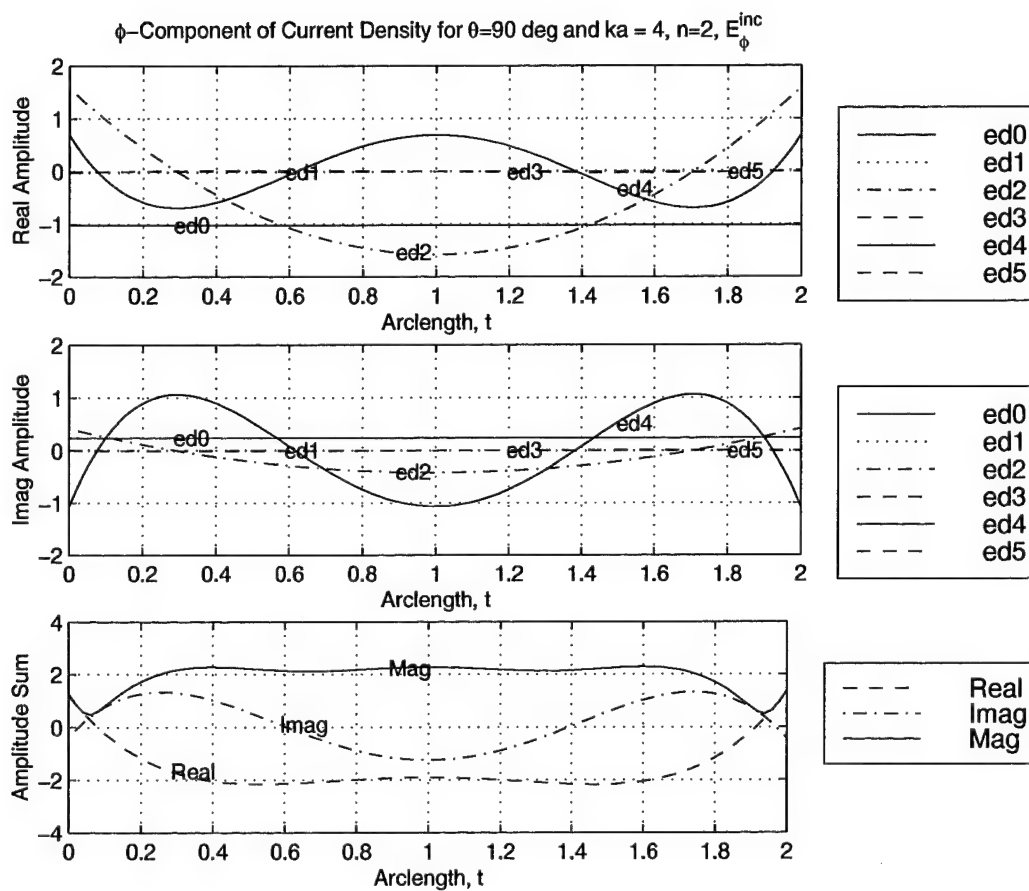
```

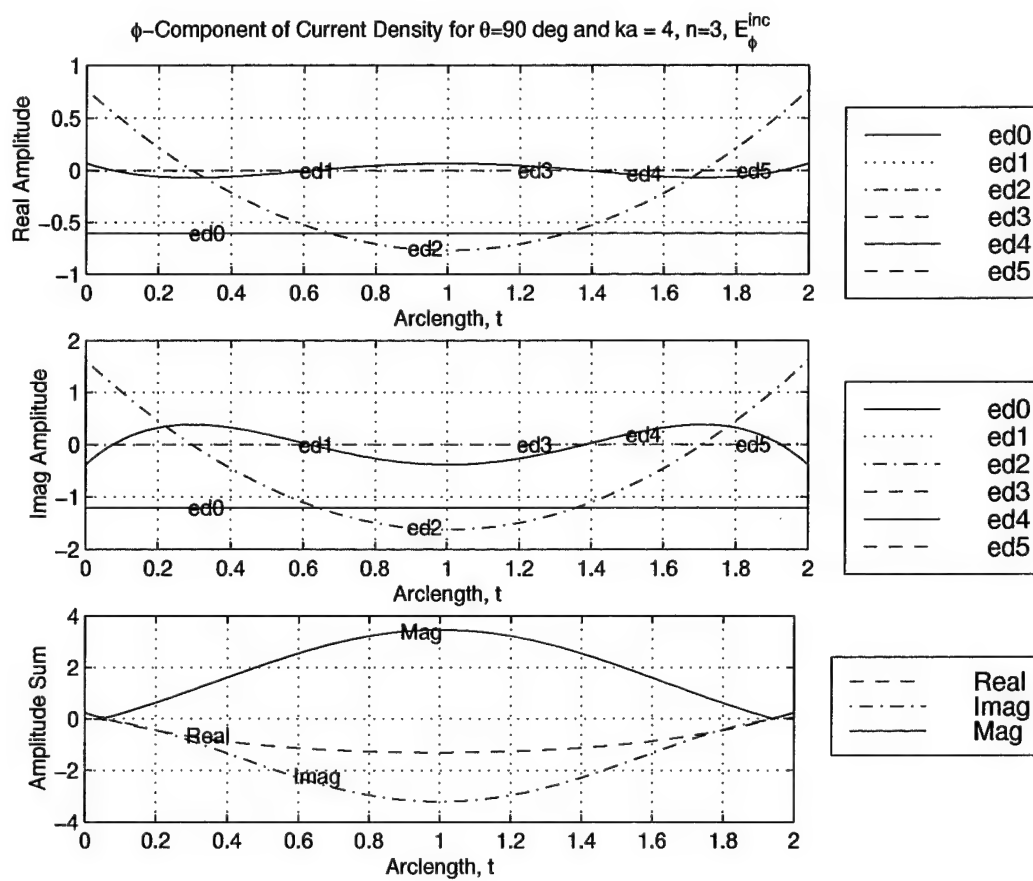
Appendix B. Current Densities by Mode

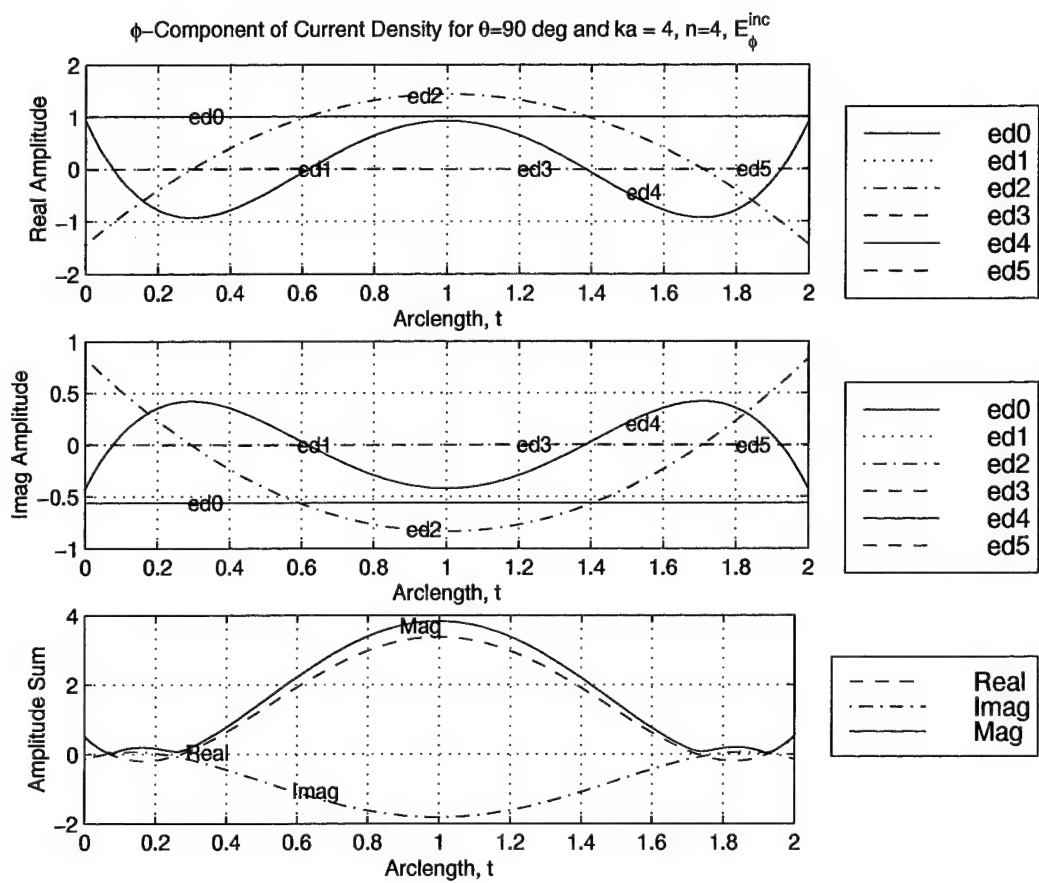
This appendix contains the current density components for all modes of the $ka = 4.0$ sphere in both the \hat{t} and $\hat{\phi}$ directions for \bar{E}_{ϕ}^{inc} incident at $\theta = 90^\circ$. The total current density over accumulated over the T_0 - T_5 Chebyshev modes and the $n = 0$ - $n = 5$ is also included.

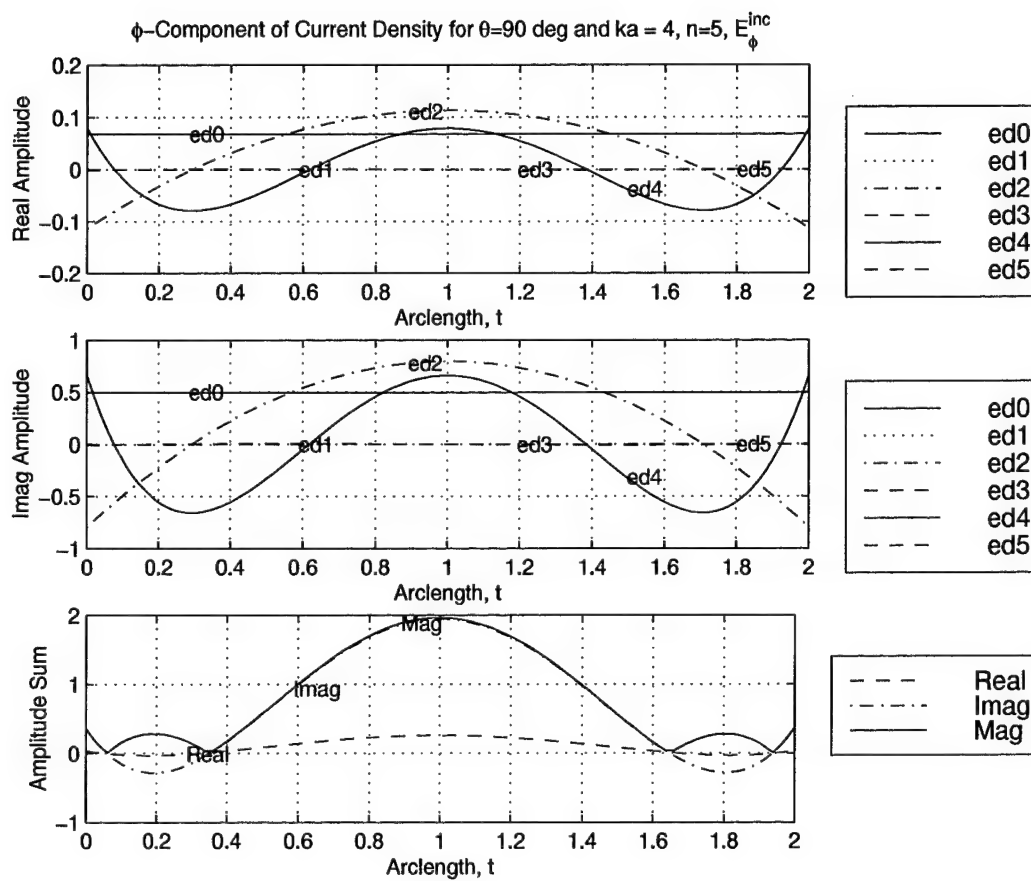


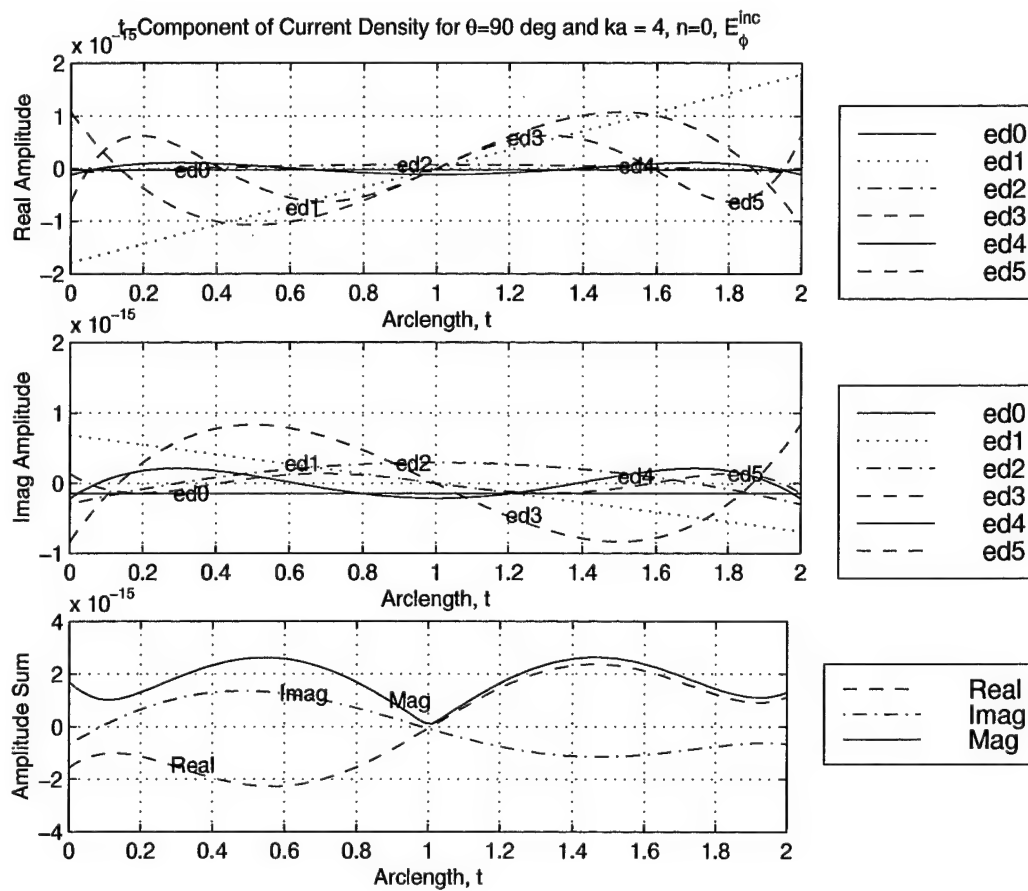


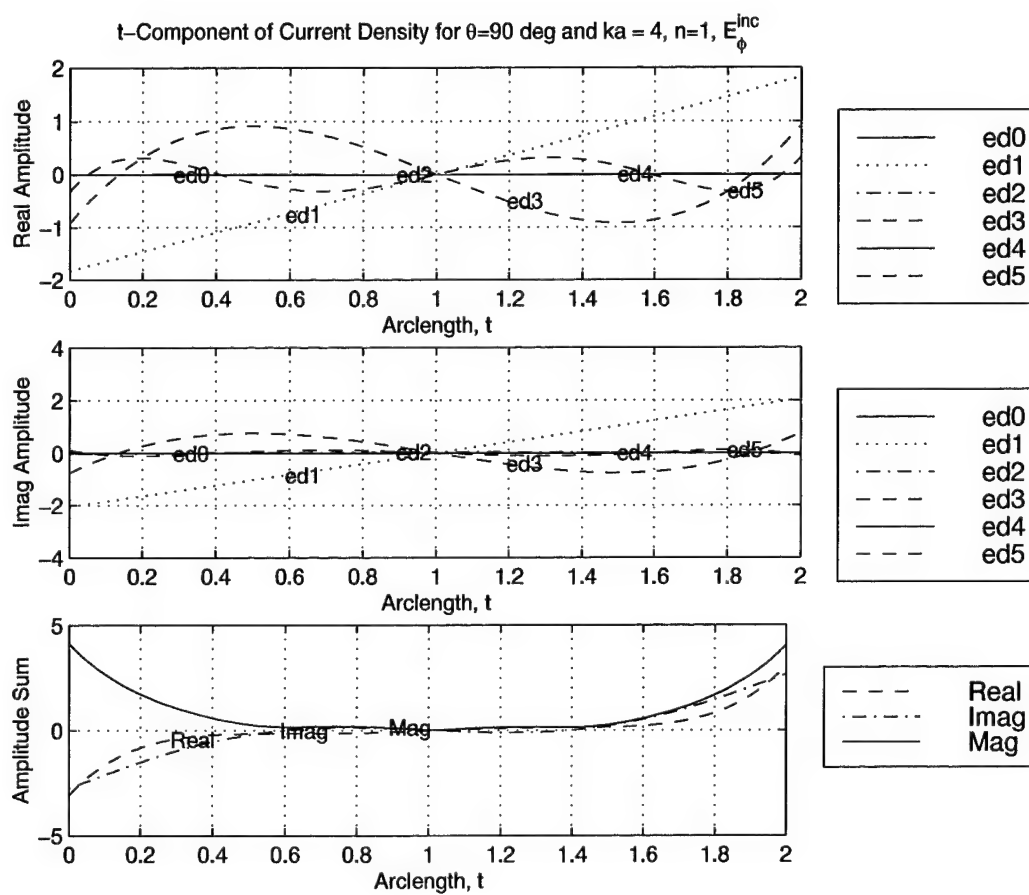


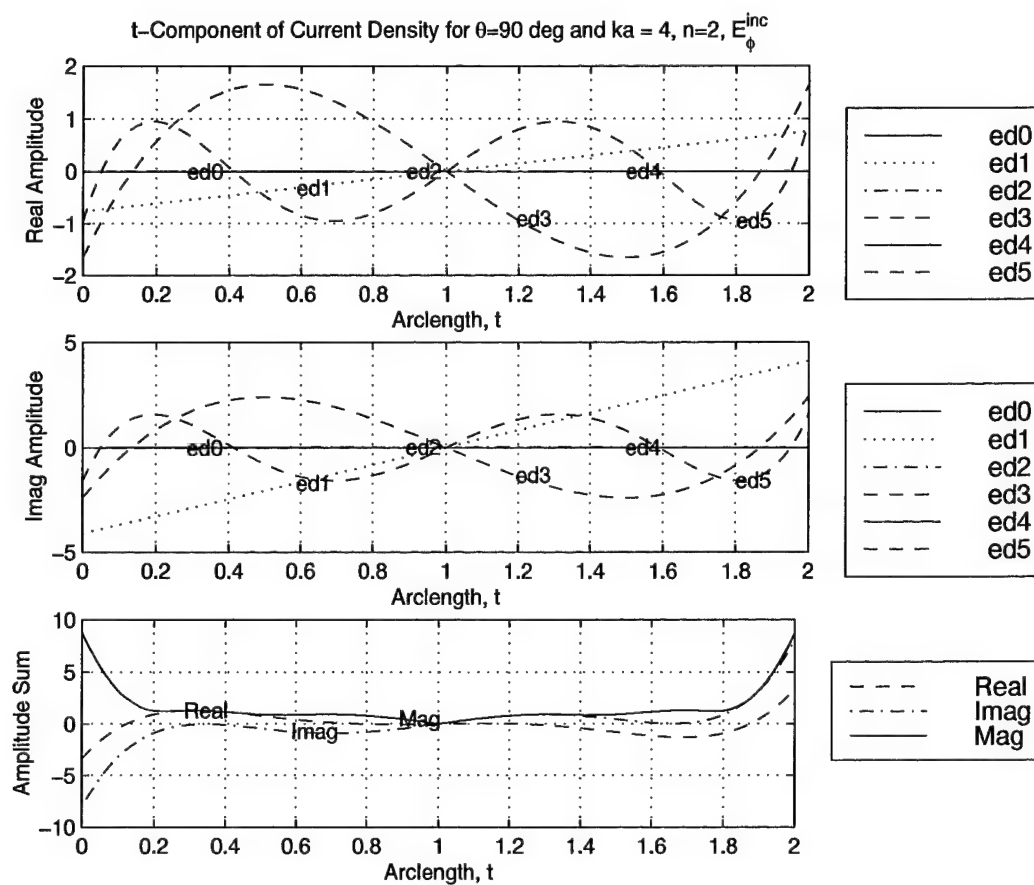


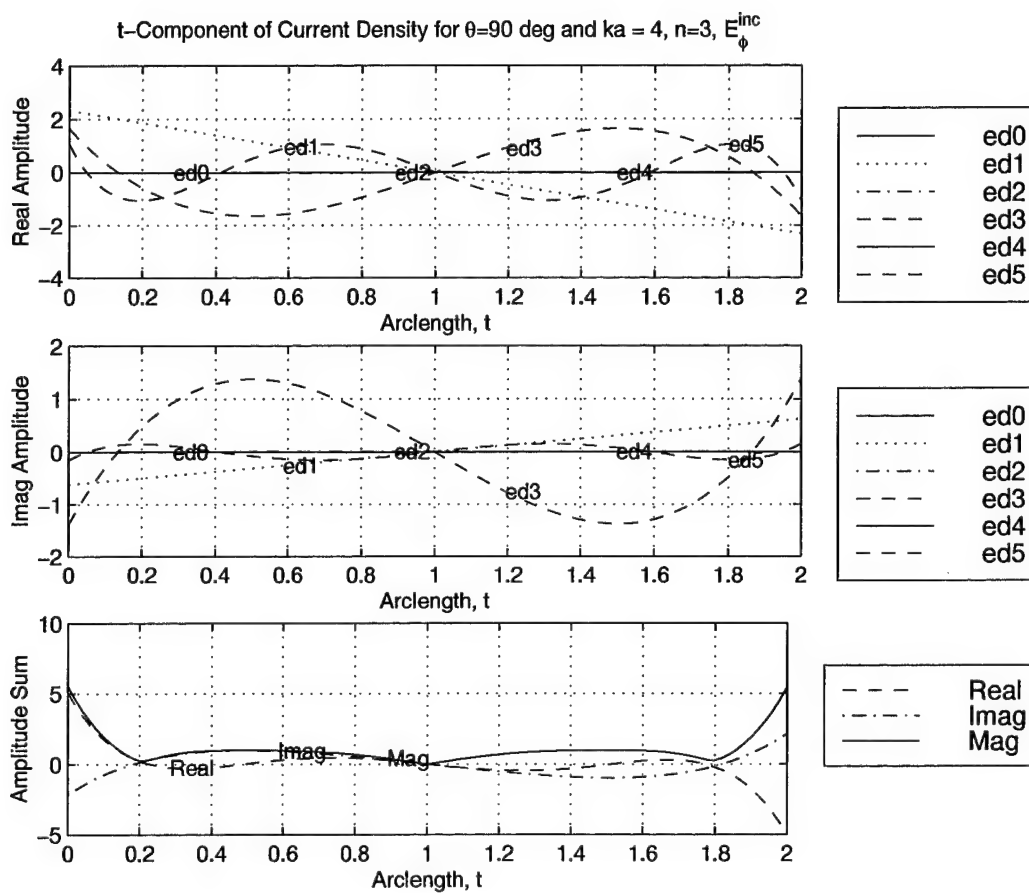


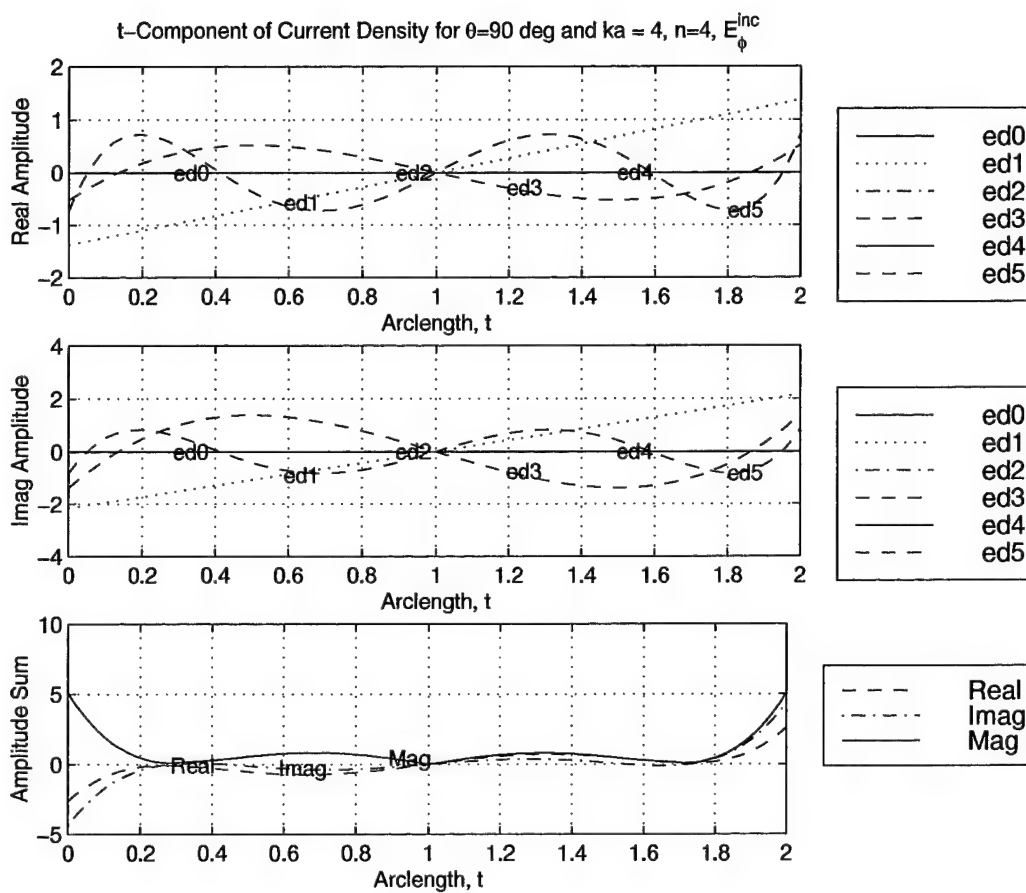


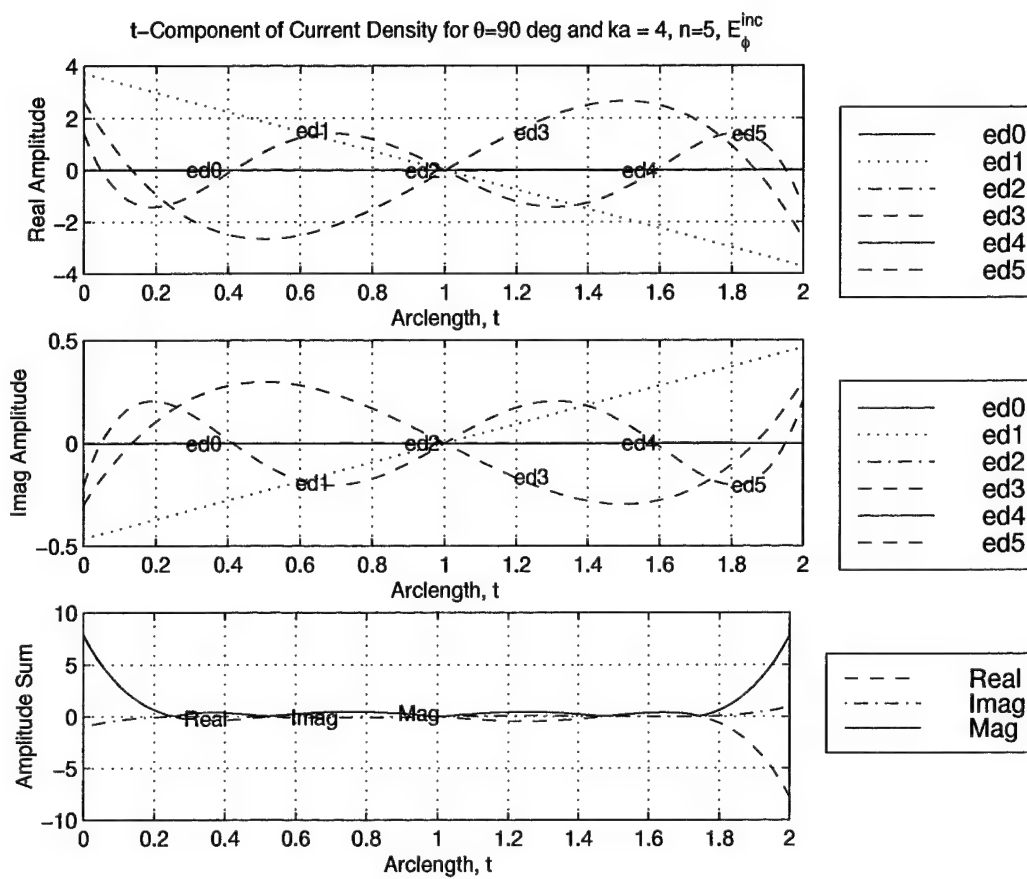


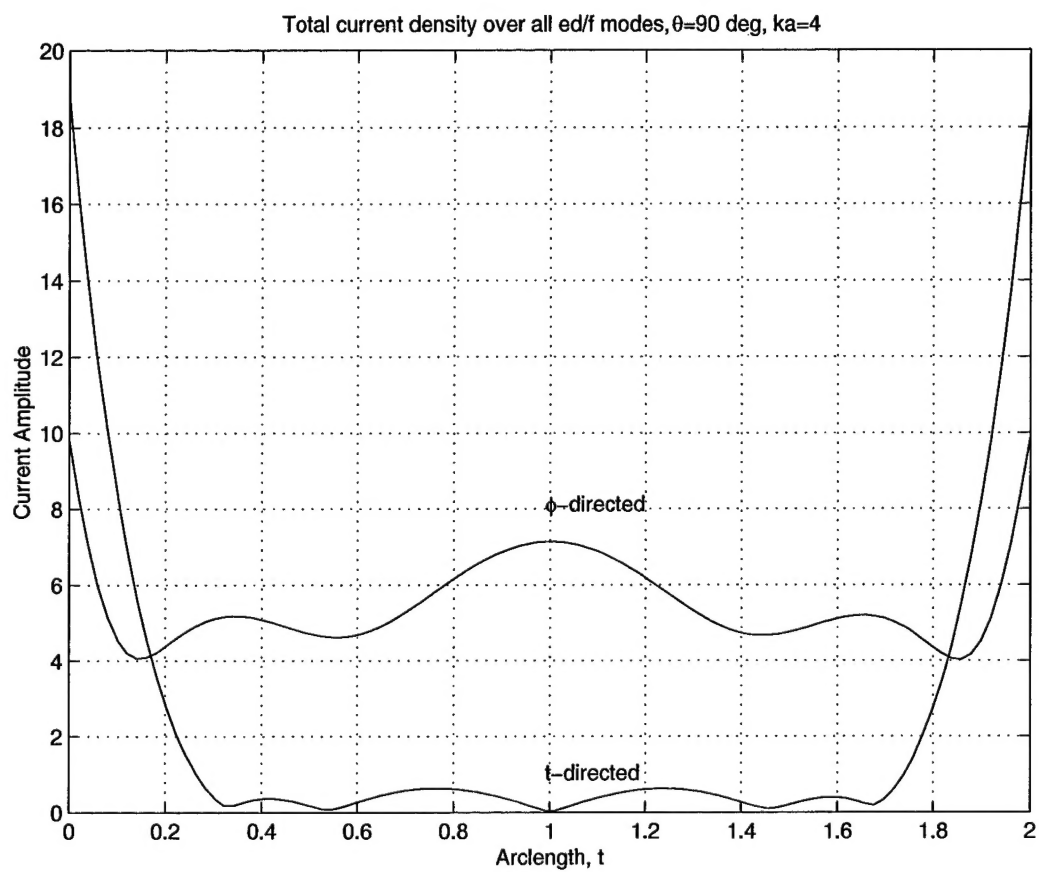












Bibliography

1. Balanis, Constantine A. *Advanced Engineering Electromagnetics*. New York: John Wiley and Sons, 1989.
2. Balanis, Constantine A. *Antenna Theory* (Second Edition). New York: John Wiley and Sons, 1997.
3. Butler, Chalmers M. and Donald R. Wilton. "General Analysis of Narrow Strips and Slots," *IEEE Transactions on Antennas and Propagation*, 28:42-48 (January 1980).
4. Glisson, A. W. and D. R. Wilton. *Simple and Efficient Techniques for Treating Bodies of Revolution*. Contract F30602-78-C-0120, Griffiss Air Force Base, New York 13441: Rome Air Development Center, March 1979 (AD-A067361).
5. Harrington, R. F. *Field Computation by Moment Methods*. New York: IEEE Press, 1997.
6. Kent, William J. *Plane Wave Scattering by Thin Linear Dielectric-coated Wires and Dielectric Strips: A Moment Method Approach with Physical Basis Functions*. PhD dissertation, The Ohio State University, Columbus OH, 1985 (ON8518971).
7. Kitazawa, Toshihide and others. "Analysis of the Dispersion Characteristic of Slot Line with Thick Metal Coating," *IEEE Transactions on Microwave Theory and Techniques*, 28:387-392 (April 1980).
8. Mautz, Joseph R. and Roger F. Harrington. *Computer Programs for H-Field, E-Field, and Combined Field Solutions for Bodies of Revolution*. Contract F19628-76-C-0300, Griffiss Air Force Base, New York 13441: Rome Air Development Center, June 1977.
9. Mautz, Joseph R. and Roger F. Harrington. *H-Field, E-Field, and Combined Field Solutions for Bodies of Revolution: Interim Technical Report*. Contract F19628-76-C-0300, Griffiss Air Force Base, New York 13441: Rome Air Development Center, March 1977.
10. National Bureau of Standards. *Handbook of Mathematical Functions*. Applied Mathematics Series 55. Washington: U.S. Government Printing Office, 1965.
11. Peterson, Andrew F. and others. *Computational Methods for Electromagnetics*. New York: IEEE Press, 1998.
12. *My Research*. Personal Web Page. <http://www.teorel.lth.se/svensk/SPmapp/soren.html>, soeren@teorel.lth.se, Lund Sweden, Oct 1988.
13. Rogers, Jim. *JRMBOR User's Guide*. Greenbelt Maryland: Atlantic Aerospace Electronics Corporation, 1997.
14. Skinner, Paul. Class handout distributed in EENG 630, Applications of Electromagnetic Theory Graduate School of Engineering, Air Force Institute of Technology (AETC), Wright-Patterson AFB OH, April 1998.

15. Thiele, Gary A. and Thomas H. Newhouse. "A Hybrid Technique for Combining Moment Methods with the Geometrical Theory of Diffraction," *IEEE Transactions on Antennas and Propagation*, 23:62-69 (January 1975).
16. Wood, Capt William D. *Electromagnetic Scattering from a Cavity in a Ground Plane: Theory and Experiment*. PhD dissertation, Graduate School of Engineering, Air Force Institute of Technology (AETC), Wright-Patterson AFB OH, March 1997 (DA9732739).

Vita

Captain Arthur P. Ford, IV was born on 16 August 1969 in Murray, Utah. He graduated from Alameda High School in Lakewood, Colorado in 1987 and entered Brigham Young University on university and Air Force Reserve Officer Training Corps scholarships. He graduated in 1994 with a B.S. in Electrical Engineering and a B.A. in Japanese and was commissioned as an officer in the United States Air Force. He was assigned as an engineer and test manager for a tri-service infrared decoy program at the Aeronautical Systems Center of the Air Force Materiel Command at Wright-Patterson Air Force Base, Ohio. In 1995 he was awarded a Dayton Area Graduate Studies Institute scholarship and entered the Air Force Institute of Technology as a part-time student. In 1997 he was admitted to the full-time program to specialize in Low-Observables technology. Following graduation in March 1999, he will be assigned to work with the B-2 aircraft based at Whiteman Air Force Base, Missouri.

Permanent address: 9134 West Iowa Place
Lakewood, Colorado 80232